

POLITECNICO DI TORINO

SCUOLA DI DOTTORATO

Dottorato in Fluidodinamica – XXVII ciclo

Tesi di Dottorato

**Component-wise models for static,
dynamic and aeroelastic analyses of
metallic and composite aerospace
structures**



Alfonso Pagani

Tutore

Prof. Erasmo Carrera

Coordinatore del corso di dottorato

Prof. Gaetano Iuso

Co-tutore

Dr. Marco Petrolo

March 2015

to my loved ones

Acknowledgements

The work presented in this thesis would not have been possible without the support of Professor Erasmo Carrera, who constantly inspired and encouraged me. His revolutionary ideas, his passion for research, and his enormous knowledge of aerospace structures and solid mechanics have instilled within me an unconditioned love for engineering, science and exploration. I also thank him for his efforts in letting me carry out part of my PhD activity with Professor J.R. Banerjee and Dr. Marco Boscolo at London City University, Professor Antonio J.M. Ferreira at Universidade do Porto, and Dr. Marco Petrolo (my co-tutor) at RMIT University. They all played a crucial role in my research.

I am very grateful also to the extraordinary guys who are (or were) part of the MUL2 group: Marco and Alberto, who thought me a lot of things, Matteo, for our extremely interesting and always formative discussions about all the topics of structure mechanics and aeroelasticity, but also Enrico, Mirella, Francesco, Stefano, Tommaso, Marianna, Fiorenzo, Prasantha, Moshen, Gianni, Alessandro.

Finally, I would like to thank my family and my beloved Teresa, for their patience and generous support. Their invaluable lessons and advices continue to light my path.

Torino, March 3, 2015

Alfonso Pagani

Abstract

In the framework of structural mechanics, the classical beam theories that are commonly adopted in many applications may be affected by inconsistencies, because they are not able to foresee higher-order phenomena, such as elastic bending/shear couplings, restrained torsional warping and 3D strain effects. Depending on the problem, those limitations can be overcome by using more complex and computationally expensive 2D and 3D models or, alternatively, by adopting refined beam models, to which many scientists have dedicated their research over the last century. One of the latest contributions to the development of advanced models, including variable kinematic beam theories, is the Carrera Unified Formulation (CUF), which is the main subject of the research discussed in this thesis.

According to CUF, the 3D displacement field can be expressed as an arbitrary expansion of the generalized displacements. Depending on the choice of the polynomials employed in the expansion, various classes of beam models can be implemented. In this work, for instance, Taylor-like and Lagrange polynomials are adopted. The former choice leads to the so-called TE (Taylor Expansion) beam models, whereas LE (Lagrange Expansion) beam models with only pure displacement variables are obtained by interpolating the problem unknowns by Lagrange polynomials. The strength of CUF lies in the fact that, independently of the choice of the polynomials, the governing equations are written in terms of fundamental nuclei, which are invariant with the theory class and order.

In this thesis, both strong and weak form governing equations for arbitrarily refined CUF models are derived. Subsequently, exact closed-form and approximate solutions are sought. Exact solutions of any beam model with arbitrary boundary conditions are found by formulating a frequency-dependant Dynamic Stiffness (DS) matrix and by using the Wittrick-Williams algorithm to carry out the resulting transcendental eigenvalue problem for free vibration analysis. Conversely, a linear eigenvalue problem is also derived by approximating the strong form governing equations by Radial Basis Functions (RBFs). On the other hand, weak form solutions are discussed by Finite Element Method (FEM), which still deserves important attentions due to its versatility and numerical efficiency. The various problems of the mechanics are addressed, including static, free vibration and dynamic response problems.

Based on CUF and the proposed numerical methods, advanced methodologies for the analysis of complex structures, such as aircraft structures and civil engineering constructions, are developed. Those advanced techniques make use of the Component-Wise (CW) and the Multi-Line approaches. The CW method exploits the natural capability of the LE CUF beam models to be assembled at the cross-section level. This characteristic allows the analyst to use only CUF beam elements to model each component (e.g., stringers, panels and ribs) of the structure and purely physical surfaces are employed to construct the mathematical models. In the ML framework, on the other hand, each component of the structure is modelled via TE beam elements of arbitrary order. Compatibility of displacements between two or more components is then enforced through the Lagrange

multipliers method.

The second part of this thesis deals with aeroelasticity. In particular, the Vortex (VLM) and the Doublet Lattice Methods (DLM) are employed and extended to CUF to develop aeroelastic models. VLM is used to model the steady contribution in the aerodynamic model, whereas DLM provides the unsteady contribution in the frequency domain. The infinite plate spline approach is adopted for the mesh-to-mesh transformation. Finally, the g-method is described as an effective means for the formulation of the flutter stability problem. Particular attention is given to the extension of this methodology to exact DS solutions of CUF beams.

Simplified, discrete, dynamic gust response analysis by refined beam models is also discussed. In this work, vertical gusts and one-minus-cosine idealization is addressed. Accordingly, gust loads in terms of time-dependent load factors are formulated. Subsequently, the mode superposition method is briefly introduced in order to solve the linear dynamic response problem in the time domain by using both weak and strong form solutions of CUF models.

In the final part of the work, extensions of 1D CUF models for Fluid-Dynamics problems are carried out. CUF approximation of laminar, incompressible, Stokes flows with constant viscosity was introduced in a recent thesis work and it is here extended to the hierarchical p-version of FEM, which makes use of Legendre-like polynomials to interpolate the generalized unknowns along the 1D computational domain.

Finally, the structural, aeroelastic and fluid-dynamics formulations are validated by discussing some selected results. In particular, regarding structures, the efficiency of the various numerical approaches when applied to CUF is investigated and simple to complex problems are considered, including metallic and composite wings. The aeroelastic analyses show that classical beam models are not adequate for the flutter detection, and at least a third-order beam model is required. Contrarily, classical beam models can be quite accurate in dynamic gust response analysis if no coupling phenomena occur, i.e. when the response is dominated by only pure bending modes. Regarding fluid-dynamics, it is demonstrated that CUF models can reproduce the results by finite volume codes for both simple Poiseuille and complex non-axisymmetric fluids in cylinders. In general, the capability of the proposed CUF models to provide accurate results with very low computational efforts is firmly highlighted. Similar analyses are possible only by using 3D models, which usually require a number of degrees of freedom that is some two order of magnitude higher.

Keywords: *Component-wise, one-dimensional refined models, Carrera Unified Formulation, Finite Element Method, Dynamic Stiffness Method, Radial Basis Functions, Doublet Lattice Method, aircraft structures, aeroelasticity, structural dynamics, fluid dynamics, composite materials.*

Sommario

Nel campo della modellizzazione strutturale, le teorie classiche delle travi che sono usualmente adottate nei modelli matematici sono affette da inconsistenze fisiche, quali ad esempio l'impossibilità di descrivere correttamente fenomeni di accoppiamento flessione/taglio, warping e deformazioni tridimensionali. Queste limitazioni, a seconda del problema, possono essere surclassate tramite l'utilizzo di modelli 2D o 3D, a spese di un maggior costo computazionale, oppure adottando modelli trave rifiniti, a cui molti scienziati hanno dedicato le proprie ricerche nel corso dell'ultimo secolo. Uno degli ultimi contributi allo sviluppo di teorie avanzate, comprese le teorie trave a cinematica variabile, è la Carrera Unified Formulation (CUF), la quale rappresenta il tema principale di questo lavoro di tesi.

Secondo la CUF, il campo di spostamenti tridimensionale può essere espresso come una espansione generica degli spostamenti generalizzati. A seconda della scelta dei polinomi adottati nell'espansione, si possono implementare diverse classi di modelli trave. Nel presente lavoro, ad esempio, sono stati impiegati polinomi di tipo Taylor e Lagrange. Nel primo caso, si hanno i cosiddetti modelli TE (Taylor Expansion), mentre, se si utilizzano i polinomi di Lagrange, si ottengono i modelli LE (Lagrange Expansion), che sono caratterizzati da sole incognite di spostamento. La potenza del metodo CUF risiede nel fatto che, indipendente dalla scelta di questi polinomi, le equazioni di governo sono scritte in termini di nuclei fondamentali, i quali sono indipendenti dalla classe e dall'ordine del modello.

In questa tesi, vengono derivate le equazioni di governo sia in forma forte che in forma debole per modelli trave CUF di ordine arbitrario. Si ricavano, quindi, soluzioni esatte in forma chiusa e approssimate. Soluzioni esatte per qualsiasi modello trave soggetto a generiche condizioni al contorno sono ricavate formulando una matrice dipendente dalla frequenza, la cosiddetta matrice *Dynamic Stiffness* (DS), e applicando l'algoritmo di Wittrick-Williams per la risoluzione del problema non-lineare agli autovalori. Al contrario, una soluzione approssimata dello stesso problema viene ricavata per mezzo di interpolazione delle equazioni differenziali tramite funzioni Radial Basis (RBFs). Le soluzioni delle equazioni in forma debole vengono, invece, ricavate per mezzo del Metodo agli Elementi Finiti (FEM), che tutt'oggi merita importanti attenzioni per via del suo successo, la sua versatilità e efficienza numerica. Vengono discussi i vari problemi della meccanica, inclusi problemi di risposta statica, vibrazioni libere e risposta dinamica.

Sulla base dei modelli CUF formulati e i vari metodi numerici adottati, si sviluppano quindi metodologie avanzate per l'analisi di strutture complesse, quali strutture aeronautiche e civili. Queste metodologie fanno uso delle tecniche Component-Wise (CW) e Multi-Line (ML). Il metodo CW sfrutta la naturale caratteristica dei modelli CUF LE di essere assemblati sulla sezione della trave. Tale proprietà permette all'analista di utilizzare meramente elementi CUF 1D per modellizzare ogni componente strutturale (ad es., correnti, longheroni, pannelli e centine) e di utilizzare semplicemente le superfici fisiche

per delimitare il modello matematico. Nel caso della tecnica ML, invece, ogni componente della struttura viene modellizzato tramite elementi TE di ordine qualsiasi. Quindi, la compatibilità degli spostamenti all'interfaccia tra gli elementi viene imposta per mezzo di moltiplicatori di Lagrange.

La seconda parte della tesi riguarda applicazioni di tipo aeroelastico. In particolare, si estendono i metodi Vortex (VLM) e Douber Lattice (DLM) ai modelli CUF per sviluppare modelli aeroelastici avanzati per lo studio dei fenomeni di flutter. Il VLM viene utilizzato per modellizzare il contributo stazionario nel modello aerodinamico, mentre il DLM viene sfruttato per formulare il contributo non-stazionario nel dominio delle frequenze. L'appiaccio *infinite plate spline* è adottato per il passaggio delle informazioni dalla mesh strutturale e quella aerodinamica. Infine, il *g-method* viene descritto e utilizzato per la formulazione del problema di stabilità aeroelastica dinamica. Particolare attenzione è stata posta nell'estensione di questa metodologia alle soluzioni DS esatte dei modelli CUF.

Vengono anche discusse analisi semplificate di risposta alla raffica discreta per mezzo di teorie trave rifinite. Raffiche verticali modellizzate per mezzo dell'approssimazione uno-meno-coseno vengono in particolare prese in considerazione. I carichi di raffica sono, quindi, formulati in termini di fattori di carico dipendenti dal tempo. In seguito, il metodo di sovrapposizione modale è brevemente descritto e utilizzato per risolvere il problema lineare di risposta dinamica nel dominio del tempo, utilizzando sia modelli CUF in forma debole e forte.

Estensioni dei modelli CUF 1D a problemi fluidodinamici sono, infine, presentate nell'ultima parte dell'elaborato. L'approssimazione tramite CUF di flussi di Stokes, laminari, incomprimibili e a viscosità costante sono stati recentemente proposti in un lavoro di tesi. Tale formulazione viene qui estesa alla *p-version* del metodo FEM, il quale fa uso di polinomi gerarchici di tipo Legendre per interpolare le incognite generalizzate lungo il dominio mono-dimensionale.

Le formulazioni strutturale, aeroelastica e fluidodinamica sono validate per mezzo di alcuni esempi selezionati. In particolare, riguardo le strutture, viene discussa l'efficacia dei vari metodi numerici applicati ai modelli CUF, prendendo in considerazione problemi semplici e complessi, comprese ali in materiale metallico e composito. Le analisi aeroelastiche dimostrano che i modelli classici sono assolutamente inadeguati per l'analisi dei fenomeni di flutter essendo necessario almeno un modello trave del terzo ordine. Al contrario, i modelli trave classici possono essere abbastanza accurati per le analisi di risposta alla raffica, purchè la risposta sia dominata da puri modi flessionali. Per quanto concerne la formulazione fluidodinamica, viene dimostrato che i modelli CUF 1D possono riprodurre i stessi risultati di codici ai volumi finiti sia nel caso di semplici flussi di Poiseuille, sia nel caso di flussi non-assialsimmetrici all'interno di cilindri. In generale, si evidenzia fermamente la capacità dei modelli CUF proposti di assicurare risultati accurati al prezzo di costi computazionali assolutamente esigui. Analisi di tale accuratezza sono altrimenti possibili solamente utilizzando modelli 3D, che solitamente richiedono un numero di gradi di libertà di alcuni ordini di grandezza maggiore.

Parole chiave: *Component-wise, modelli rifiniti mono-dimensionali, Carrera Unified Formulation, Metodo agli Elementi Finiti, Dynamic Stiffness Method, Funzioni Radial Basis, Doublet Lattice Method, strutture aeronautiche, aeroelasticità, dinamica strutturale, fluidodinamica, materiali compositi.*

Contents

Acknowledgements	I
Abstract	III
Sommario	V
Contents	VII
1 Introduction	1
1.1 Reinforced-shell structures for aerospace vehicles	1
1.2 Higher-order beam theories	3
1.2.1 CUF, state-of-the-art	3
1.2.2 The component-wise approach	4
1.2.3 Adopted numerical methods	5
1.3 Aeroelastic phenomena	6
1.4 One-dimensional models for fluid-dynamics	7
2 Carrera Unified Formulation	9
2.1 Preliminaries	9
2.2 From classical to variable kinematic beam theories	11
2.2.1 Taylor Expansion (TE)	13
2.3 Lagrange Expansion (LE)	14
3 Strong Form Solutions for Free Vibrations	17
3.1 Equations of motion of the N-order TE model	17
3.2 Dynamic Stiffness Method (DSM)	19
3.2.1 Solution of the differential equations	19
3.2.2 Dynamic stiffness matrix	22
3.2.3 Application of the Wittrick-Williams algorithm	24
3.3 Radial Basis Functions (RBFs)	24
3.3.1 From a differential problem to a eigenvalue problem via RBFs	25
4 Finite Element Method	29
4.1 Weak form governing equations	29
4.1.1 Static response analysis	30
4.1.2 Free vibrations	30
4.1.3 Dynamic response	31
4.2 Stiffness matrix	31
4.3 Mass matrix	32
4.3.1 Localized inertia	33

4.4	Loading vector	34
4.4.1	Inertial loads	34
5	Component-wise	35
5.1	Multi-component structures	35
5.2	Component-Wise (CW) approach	36
5.3	Multi-Line (ML)	37
5.3.1	Lagrange multipliers	38
5.3.2	ML models for the analysis of composites	39
6	Aeroelastic Model	41
6.1	Hypotheses	41
6.2	Oscillating lifting surfaces	41
6.2.1	Vortex Lattice Method (VLM)	42
6.2.2	Quartic Doublet Lattice Method (DLM)	43
6.3	Unsteady aeroelastic analysis	44
6.3.1	Modal shapes and boundary conditions	44
6.3.2	The g-method	45
6.4	Generalized mass and stiffness matrices	46
7	Discrete Gust Response	47
7.1	Vertical gust	47
7.2	One-minus-cosine discrete gust idealization	48
7.2.1	Effect of aeroelastic deformation on $C_{L\alpha}$	49
7.3	Solution of equations of motion in dynamic analysis	49
7.4	Mode superposition	49
7.4.1	Analysis with damping neglected	50
7.4.2	Analysis with damping included	51
8	Computational Fluid-Dynamics by CUF	53
8.1	Preface and notation	53
8.2	Stokes equations	54
8.2.1	Weak formulation of the Stokes equations	55
8.2.2	Galerkin approximation	56
8.3	One-dimensional CUF models for Stokes flows	57
8.3.1	Velocity and pressure field approximations	57
8.3.2	CFD fundamental nuclei	58
8.4	Boundary conditions	60
9	Numerical Results	63
9.1	Comparison of FEM, DSM and RBFs for free vibrations	63
9.1.1	Rectangular cross-section beam	63
9.1.2	Thin-walled cylinder	66
9.1.3	Four- and two-layer beams	68
9.2	Analysis of thin-walled and composite structures by ML	70
9.2.1	I-section beam	71
9.2.2	Symmetric laminated beam	73
9.3	Analysis of aircraft structures by CW	75
9.3.1	Static analysis of a trapezoidal wing box	75
9.3.2	Free vibrations of a complete NACA wing	78

- 9.3.3 Free vibrations of composite wing boxes 81
- 9.4 Application of CW models to civil engineering structures 82
- 9.5 Flutter analysis of flat-plate wings 85
 - 9.5.1 Isotropic plate wing 85
 - 9.5.2 Composite plate wing 88
- 9.6 Dynamic and gust response analyses 90
 - 9.6.1 Square cross-section beam subjected to sinusoidal loading 90
 - 9.6.2 Sweep angle effect on gust response of metallic plate wings 91
 - 9.6.3 Composite plate wing 93
 - 9.6.4 Complete NACA aircraft wing 94
- 9.7 Stokes flows 97
 - 9.7.1 Poiseuille flow 97
 - 9.7.2 Fourth-order velocity profile 98
 - 9.7.3 Fifth-order velocity profile 100
- 10 Conclusions** 105
 - 10.1 Work outline 105
 - 10.2 Concluding remarks 107
 - 10.3 Future work 108
- Bibliography** 109

Chapter 1

Introduction

1.1 Reinforced-shell structures for aerospace vehicles

Primary aircraft structures are essentially reinforced thin shells [21]. These are the so-called *semimonocoque* constructions (see Fig. 1.1), which are obtained by assembling three main components: skins (or panels), longitudinal stiffening members (including spar caps) and transversal stiffeners (ribs). The determination of stress/strain fields in these structural components and their dynamic behaviour is of prime interest for structural analysts.

Many different approaches were developed in the first half of the last century. These are discussed in major reference books [21, 134] and more recently in [24]. Among these approaches the so-called Pure Semimonocoque (PS) (or “idealized semimonocoque”) is the most popular, since it assumes constant shear into panels and shear webs, according to the simplification outlined in Fig. 1.2. The main advantage of PS is that it leads to a system of linear algebraical equations. However, the number of such equations rapidly increases for multi-bay box structures with high redundancies. The number of resulting equations (and redundancies) can be strongly reduced by coupling PS with the assumptions from Euler-Bernoulli (Euler-Bernoulli Beam Model, EBBM) [69] or Timoshenko theories (Timoshenko Beam Model, TBM) [155, 156]. Many works are known to overcome limitations related to constant shear hypotheses, see [57, 86, 64, 65, 20] as examples. The systematic use of matrix methods in aircraft structure analysis was introduced by Argyris and Kensley [4]. Here, the PS approach and force methods were used to describe an automatic technique to build compliance matrices. This automatic technique is one of the pioneering contributions to the development of Finite Element Methods (FEM).

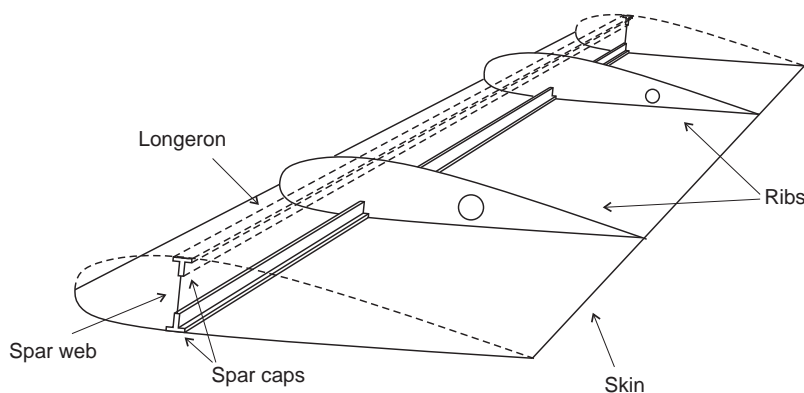


Figure 1.1: Simplified sketch of a wing structure



Figure 1.2: Reinforced-shell structure (a) and related semimonocoque simplification (b)

Due to the advent of computational methods, mostly FEM, the analysis of complex aircraft structures continued to be made using a combination of solids (3D), plates/shells (2D) and beams (1D). These were implemented first in Nastran codes (see for example [113]). Many others commercial Finite Element (FE) codes have been developed and used in aerospace industries. Nowadays FEM models with a number of unknowns (Degrees Of Freedom, DOFs) close to 10^6 are widely used in common practise. The possible manner in which stringers, spar caps, spar webs, panels, ribs are introduced into FE mathematical models is part of the knowledge of structural analysts. A short discussion of this follows.

A number of works have shown the necessity for a proper simulation of the stiffeners-panel “linkage”. Satsangi and Murkhopadhyay [138] used 8-node plate elements assuming the same displacement field for stiffeners and plates. Kolli and Chandrashekhara [105] formulated an FE model with 9-node plate and 3-node beam elements. Gangadhara [83] carried out linear static analyses of composite laminated shells using a combination of 8-node plate elements and 3-node beam elements. Recently, Thin and Khoa [154] have developed a new 9-node rectangular plate model to study the free vibrations of shell structures with arbitrary oriented stiffeners.

It is often necessary to model stiffeners out of the plate/shell element plane. In this case, beam nodes are connected to the shell element nodes via rigid fictitious links. This methodology presents some inconsistencies. The main problem is that the out-of-plane warping displacements in the stiffener section are neglected, and the beam torsional rigidity is not correctly predicted. Several solutions have been proposed in the literature to overcome this issue. Patel et al. [125] introduced a torsion correction factor. Vörös [166, 167] proposed a procedure to model the connection between the plate/shell and the stiffener where the shear deformation of the beam is neglected and the formulation of the stiffener is based on the well-known *Bernoulli-Vlasov* [164] theory. In Vörös’ method the stiffener element has two nodes with seven degrees of freedom per node. In order to maintain the displacement compatibility between the beam and the stiffened element, a special transformation was used, which included torsional-bending coupling and the eccentricity of internal forces between the stiffener and the plate elements.

3D finite element models are usually implemented as soon as the wing structural layouts are determined. Because of their complexity, solid models are generally used only within optimization procedures. In fact, despite the availabilities of even cheaper computer power, these FEM models present large computational costs and their use in multi-field iterative processes, such as aeroelastic analyses, is quite a burden. Nowadays the trend is to use equivalent, simplified, lower fidelity 1D FEM models (the so-called “stick-model”) of the wing structure to be used within iterative algorithms. There are numerous papers dealing with wing stick models in the literature, such as [1, 129, 68]. These methodologies are based on the extraction of the structural stiffness of the wing with respect to its principal axes.

Those stiffness properties are then employed to generate the wing stick model. Simplified models are created along the wing elastic axis. This applies a geometrical constraint so that the stick model principal torsional axis act as the wing elastic axis. It could be concluded that the development of computationally cheaper models compared to those by standard FE models, but with high accuracy, still plays a crucial role in aircraft structure analysis.

1.2 Higher-order beam theories

In this thesis, various 1D beam theories for the analysis of aircraft structures have been developed. The classical and best-known beam theories are EBBM and TBM. The former theory does not account for transverse shear deformations, whereas the latter assumes a uniform shear distribution along the cross-section of the beam, together with the effects of rotatory inertia. These models yield reasonably good results when slender, solid section, homogeneous structures are subjected to bending. However, the analysis of deep, thin-walled, open section beams may require more sophisticated theories to achieve sufficiently accurate results, see [115]. Over the last century, many refined beam theories have been proposed to overcome the limitations of classical beam modelling. Different approaches, including the introduction of shear correction factors, the use of warping functions based on de Saint-Venant's solution, the variational asymptotic method (VAM), the generalized beam theory (GBT), and others have been used to improve beam models. A general review of beam modelling, in which static, buckling, free-vibration and wave propagation analyses are taken into account, was proposed by Kapania and Raciti [101, 102]. Some selective references and noteworthy contributions are briefly discussed below.

Early investigations focused on the use of appropriate shear correction factors to increase the accuracy of classical 1D formulations, see, for example, Timoshenko and Goodier [157], Sokolnikoff [147], Stephen [148], Hutchinson [95], and the recent work by Nguyen et al. [114]. However, a review paper by Kaneko [97] and a recent paper by Dong et al. [62], have highlighted the difficulty of defining a universally accepted formulation for shear correction factors.

Another important class of refinement methods reported in the literature is based on the use of warping functions. The contributions by El Fatmi [66, 67], Ladevèze et al. [108], and Ladevèze and Simmonds [109] are some excellent examples.

The asymptotic type expansion, in conjunction with variational methods, was proposed in the work by Berdichevsky et al. [14], in which a noteworthy review of previous works on beam theory developments is also given. Some recent valuable contributions on VAM are those by Rajagopal and Hodges [132], Wang and Yu [168], Yu and Hodges [176, 177], and Kim and Wang [104].

The generalized beam theory was originally proposed by Schardt [140, 141]. GBT improves classical theories through the use of a piece-wise beam description of thin-walled sections. GBT has been widely employed and extended in various forms by Silvestre [144], Nunes et al. [116], Silvestre and Camotim [145], and De Miranda et al. [59].

1.2.1 CUF, state-of-the-art

This work falls within the framework of the Carrera Unified Formulation (CUF), which is a hierarchical theory allowing for the automatic and straightforward development of higher-order kinematics with no need of apriori assumptions. According to CUF, in fact, 3D problems are reduced to 2D or 1D ones in a unified manner, that is, by exploiting arbitrarily

rich expansions of the unknown variables. In the structural mechanics scenario, CUF was initially devoted to the development of refined plate and shell theories, see [22, 23]. In recent works [33], CUF has been extended to beam modeling that is the case of interest for this thesis; hence, a brief review about 1D CUF follows.

1D CUF models were first proposed to study isotropic compact and thin-walled structures in [31, 32]. In these works, 1D Taylor-like polynomials were used to describe the cross-sectional displacement field, and closed-form and FE solutions were considered. Comprehensive expansion order convergence analyses have shown how the adoption of higher-order models can lead to 3D-like accuracy with small computational costs (see also [25]). A new class of 1D CUF models was presented in [47], where Lagrange polynomials were used to model the cross-section displacement field. The adoption of Lagrange polynomials led to the development of models that have only pure displacement unknowns. Furthermore, Lagrange beams can easily be used to model geometric discontinuities and localized boundary conditions; they can also be used to refine the beam model locally.

CUF beam theory was extended to the free vibration analysis of isotropic structures by Carrera et al. [49] via FEM. Closed-form solutions were considered in [84] instead. The shell-like capabilities of the 1D CUF were highlighted in this paper. In other words, it was shown that 1D CUF models can detect those modal shapes that are characterized by severe transverse distortions.

Composite structures have been investigated through 1D CUF models by Catapano et al. [51] and Carrera and Petrolo [48]. The former considered Taylor beam models and closed-form, Navier-Type solutions. The latter exploited Lagrange beam models and complex structures, such as aeronautic longerons, were considered. The results showed the enhanced capabilities of 1D CUF models to detect 3D stress fields with 10-100 times fewer DOFs than solid FEs. Further enhancements of the 1D CUF for composites were proposed in [30] by exploiting polynomial, trigonometric, exponential and zig-zag displacement fields. Accurate displacement/strain/stress fields were obtained for both slender and short structures.

The enhanced capabilities of refined models are often only required for some portions of the structures, e.g. close to geometrical and mechanical boundary conditions. This requirement has recently led to the development of techniques that can be used to couple lower- and higher-order models. Biscani et al. [15] exploited the Arlequin method to couple different beam models along the axis of the beam. Lower computational costs were obtained without any accuracy penalties. Carrera et al. [42] obtained similar results by exploiting the Lagrange multipliers method. In [36, 37], multi-line elements were introduced by further extending this coupling technique to the cross-section level, and they are also discussed in this thesis.

Other important contributions are [161], which extended the 1D CUF models to biomechanics; [85], where thermo-mechanical analyses were proposed; and [107, 112], in which piezo-electric beam structures and related electro-mechanical analyses were discussed.

1.2.2 The component-wise approach

CUF methodology has recently been extended to the so-called Component-Wise (CW) approach [44]. In a CW model, each component of a complex structure is modeled by 1D elements. The use of Lagrange polynomials to expand the cross-sectional unknowns makes the assembling of each component straightforward because it can be conducted at the interface level by imposing displacement continuity. Furthermore, 1D, 2D, and 3D structural elements can be modeled through 1D models since the arbitrarily rich displacement fields

of the 1D CUF allow very short and thin-walled beams to be dealt with.

CW models have been widely used in the framework of aircraft structures, where each component (i.e. ribs, stiffeners, and longerons) can be modeled through the 1D CUF. Carrera et al. [39, 40] exploited the CW to carry out the static and free vibration analysis of complex aerospace structures. Those papers demonstrated the natural capability of CW approach to allow the modeling by only using physical surfaces and without the need for fictitious links connecting the various components. Furthermore, comparisons with 3D models and analytical solutions highlighted the high accuracy of the present formulation and its computational efficiency. The same approach was successfully applied to civil structures by Carrera et al. [43] and Carrera and Pagani [41], where complex structures such as industrial and civil engineering buildings have been addressed.

Regarding composite materials, CW can be considered as a multiscale approach. In fact, CW can be used to model different scale components - layers, fibers, and matrices - by accounting for their material characteristics and with no need for coupling techniques. In other words, no homogenization techniques are needed for the material properties and the different scale models can be straightforwardly assembled since only 1D FEs are employed. Refined models at the microscale level can be employed solely where required, for instance where failure can occur, whereas macroscale models can be used elsewhere (see [34, 35]).

Some of the CW results discussed in the papers above are briefly reported in this thesis, where CUF beam models of wing structures are used for structural and aeroelastic analysis, including gust response. Aeroelasticity defines important parameters in modern design of aircraft and spacecraft and it is shortly discussed in the following for the sake of completeness. However, some details about the numerical methods adopted in this thesis are given before.

1.2.3 Adopted numerical methods

In the majority of the literature about 1D CUF, FEM has been used to handle arbitrary geometries and loading conditions. Pagani et al. [118, 121, 120] extended 1D CUF to the Dynamic Stiffness Method (DSM) to obtain closed-form solutions with arbitrary boundary conditions for free vibrations of both metallic and composite structures. DSM and the related extension to CUF models are also discussed in this thesis.

DSM has been quite extensively developed for beam elements by Banerjee [7, 6, 8, 9, 10], Banerjee et al. [11], and Williams and Wittrick [171]. Plate elements based on DSM were originally formulated by Wittrick [172] and Wittrick and Williams [174]. Recently, DSM has been applied to Mindlin plate assemblies by Boscolo and Banerjee in [17, 18] and to a higher order shear deformation theory by Fazzolari et al. [74, 73]. In those papers, a more comprehensive review on the use of DSM can be found.

The DSM is appealing in dynamic analysis because, unlike the FEM, it provides the exact solution of the equations of motion of a structure once the initial assumptions on the displacements field have been made. This essentially means that, unlike the FEM and other approximate methods, the model accuracy is not unduly compromised when a small number of elements are used in the analysis. For instance, one single structural element can be used in the DSM to compute any number of natural frequencies to any desired accuracy. Of course, the accuracy of the DSM will be as good as the accuracy of the governing differential equations of the structural element in free vibration. In fact, the exact Dynamic Stiffness (DS) matrix stems from the solution of the governing differential equations.

Nevertheless, the main drawback of DSM is that it results in a nonlinear, transcendental

eigenvalue problem and iterative procedures may be needed (see [173]). Thus, a further methodology based on Radial Basis Functions (RBFs) method is proposed in this thesis as an alternative method for the solution of strong form equations of motion for CUF beams in free vibration (see [122]). The use of alternative methods to FEM and DSM for the analysis of structures, such as the meshless methods based on collocation with RBFs, is attractive due to the absence of a mesh and the ease of the collocation techniques. In recent years, RBFs method showed excellent accuracy in the interpolation of data and functions. The RBFs method was first used by Hardy [89, 90] for the interpolation of geographical scattered data and later used by Kansa [98, 99] for the solution of partial differential equations. Afterward, Ferreira successfully applied RBFs to the analysis of beams and plates [75, 76]. RBFs method is appealing because it results in a linear eigenvalue problem in the case of free vibrations. However, numerical instabilities may be encountered and they are discussed later in this thesis.

1.3 Aeroelastic phenomena

Aeroelasticity is the multidisciplinary field of study that concerns with the interaction between an elastic structure and the aerodynamic forces due to an airstream. Aeroelastic phenomena have played a major role throughout the history of flight [93]. However, torsional divergence phenomena were a major factor in the predominance of aircraft design until the early 1930s, when metallic structures were first introduced. The first recorded and documented case of aircraft flutter occurred in 1916 to the Handley Page O/400 bomber (see Fig. 1.3), which experienced violent tail oscillations due to the coupling of a fuselage torsion mode and an antisymmetric elevator mode. Since then, and after the publication of the now famous report by Theodorsen [153], flutter became a major design concern and remained so today.

A vast range of aerodynamic models has been used in aeroelastic problems in the last 80 years, from strip theories to Reynolds-averaged Navier-Stokes (RANS). Excellent reviews of these methodologies are presented in [178, 142]. The Doublet Lattice Method (DLM) emerged in the late 1960s (see [2]). More recently, an improved version of DLM has been proposed by Rodden et al. [136], and this version is used in this thesis. Three main features are responsible for DLM success [178]: (i) it offers good accuracy (unless transonic regimes are considered or separation occurs); (ii) DLM is cost competitive with respect to simpler methods such as strip theories; (iii) and fairly complex geometries can be analysed.



Figure 1.3: Historical picture of the Handley Page O/400

One of the aims of this thesis is to present aeroelastic models based on highly accurate 1D CUF structural models and low-fidelity aerodynamic tools. An important effort to apply refined beam models to aeroelastic problems was made by Librescu and his co-workers, who incorporated a number of non-classical effects in order to study the static and dynamic aeroelastic response of beam structures (see for example [111]). In recent works, Varello et al. [162] extended CUF 1D to steady aeroelasticity by using the Vortex Lattice Method (VLM), whereas DLM was used by Petrolo [128, 127] in the framework of CUF for flutter analyses. During the research activities discussed in the present thesis particular efforts have been made to extend the Petrolo's formulation to DSM, which is here used along with CUF models of isotropic and composite wings. Mode shapes are hence used with reference to DLM to carry out flutter analyses, whereas mode superposition method is exploited to conduct some representative pulse gust dynamic responses.

1.4 One-dimensional models for fluid-dynamics

The last part of the present thesis deals with minor extensions and validation of the work initiated by Varello in [160], where 1D CUF models have been extended to fluid-dynamics problems. Because of the 3D intricate nature of fluids, 1D models in fluid-dynamics are less common than the structural mechanics counterparts. However, 1D models may be of interest in some applications, such as flows in vessels and pipes. A very brief review of 1D models for fluid-dynamics follows.

The one-dimensional modelling of the human arterial system was probably introduced by Euler [70], who derived the partial differential equations expressing the conservation of mass and momentum for inviscid flows. Since then, various numerical techniques and modelling strategies have been developed and disclosed. Hereinafter, the attention is focused on some noteworthy contributions of the last years. Formaggia et al. [80] devised a 1D model of the incompressible Navier-Stokes equations by integrating the fluid equations over each section normal to the axis of the computational domain. Similarly, Smith et al. [146] developed a finite difference model of blood flow through the coronary vessels by integrating axial velocity of the 3D equations. Sherwin et al. [143] carried out 1D analyses of a vascular network by using a spectral/hp element spatial discretization with a discontinuous Galerkin formulation and a second order Adams-Bashforth time integration scheme. In [81], a family of 1D nonlinear systems for modelling the blood pulse propagation in compliant arteries were investigated.

The literature shows the clear interest in 1D models for Fluid-Dynamics, which can play an important role, for example, in fluid-structure coupled systems. The computational complexity of 1D models is, in fact, several orders of magnitude lower than that of multidimensional models based on the Navier-Stokes equations. Nevertheless, most of the works in the literature deal with 1D models providing just averaged information. In this thesis, a 1D CUF model with 3D-like capabilities is discussed. The attention is focused on the simplest problem of Stokes flows in rigid pipes. However, the results provide encouragement for future applications, including fluid-structure coupled problems.

Chapter 2

Carrera Unified Formulation

Depending on the problem, classical beam theories are usually affected by inconsistencies since they are not able to foresee higher-order phenomena, such as elastic bending/shear coupling, restrained torsional warping and 3D strain effects. A large amount of literature has been therefore produced over the years in order to improve Euler-Bernoulli and Timoshenko theories. In this chapter, a novel approach that unifies and enhances the modern theory of structures is described. Kinematics of beam is in fact obtained in a compact form, which is independent of the order of the theory. Hence, higher-order refined models can be straightforwardly implemented in a hierarchical and automatic manner.

2.1 Preliminaries

The adopted rectangular cartesian coordinate system is shown in Fig. 2.1, together with the geometry of a beam structure. The cross-section of the beam lies on the xz -plane and it is denoted by Ω , whereas the boundaries over y are $0 \leq y \leq L$. Let us introduce the transposed displacement vector,

$$\mathbf{u}(x, y, z; t) = \{ u_x \quad u_y \quad u_z \}^T \quad (2.1)$$

The time variable (t) is omitted in the remaining part of this chapter for clarity purposes. The stress, $\boldsymbol{\sigma}$, and strain, $\boldsymbol{\epsilon}$, components are expressed in transposed forms as follows:

$$\begin{aligned} \boldsymbol{\sigma} &= \{ \sigma_{yy} \quad \sigma_{xx} \quad \sigma_{zz} \quad \sigma_{xz} \quad \sigma_{yz} \quad \sigma_{xy} \}^T \\ \boldsymbol{\epsilon} &= \{ \epsilon_{yy} \quad \epsilon_{xx} \quad \epsilon_{zz} \quad \epsilon_{xz} \quad \epsilon_{yz} \quad \epsilon_{xy} \}^T \end{aligned} \quad (2.2)$$

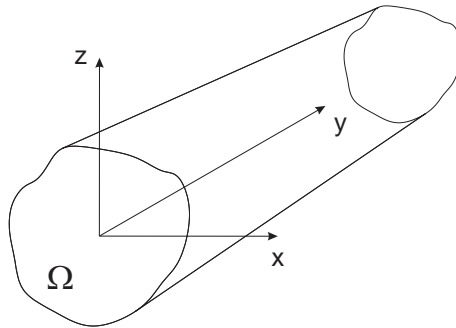


Figure 2.1: Geometry and adopted reference system

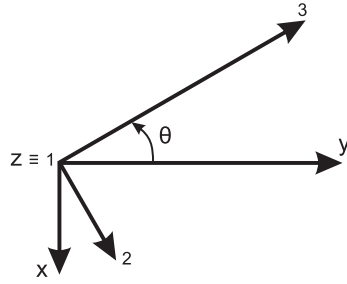


Figure 2.2: Fiber orientation angle

In the case of small displacements with respect to a characteristic dimension in the plane Ω , the strain-displacement relations are

$$\boldsymbol{\epsilon} = \mathbf{D}\mathbf{u} \quad (2.3)$$

where \mathbf{D} is the following linear differential operator matrix

$$\mathbf{D} = \begin{bmatrix} 0 & \frac{\partial}{\partial y} & 0 \\ \frac{\partial}{\partial x} & 0 & 0 \\ 0 & 0 & \frac{\partial}{\partial z} \\ \frac{\partial}{\partial z} & 0 & \frac{\partial}{\partial x} \\ 0 & \frac{\partial}{\partial z} & \frac{\partial}{\partial y} \\ \frac{\partial}{\partial y} & \frac{\partial}{\partial x} & 0 \end{bmatrix} \quad (2.4)$$

Constitutive laws are now exploited to obtain stress components to give

$$\boldsymbol{\sigma} = \tilde{\mathbf{C}}\boldsymbol{\epsilon} \quad (2.5)$$

In the case of orthotropic material the matrix $\tilde{\mathbf{C}}$ is

$$\tilde{\mathbf{C}} = \begin{bmatrix} \tilde{C}_{33} & \tilde{C}_{23} & \tilde{C}_{13} & 0 & 0 & \tilde{C}_{36} \\ \tilde{C}_{23} & \tilde{C}_{22} & \tilde{C}_{12} & 0 & 0 & \tilde{C}_{26} \\ \tilde{C}_{13} & \tilde{C}_{12} & \tilde{C}_{11} & 0 & 0 & \tilde{C}_{16} \\ 0 & 0 & 0 & \tilde{C}_{44} & \tilde{C}_{45} & 0 \\ 0 & 0 & 0 & \tilde{C}_{45} & \tilde{C}_{55} & 0 \\ \tilde{C}_{36} & \tilde{C}_{26} & \tilde{C}_{16} & 0 & 0 & \tilde{C}_{66} \end{bmatrix} \quad (2.6)$$

Coefficients \tilde{C}_{ij} depend on Young and Poisson moduli as well as on the fiber orientation angle θ that is graphically defined in Fig. 2.2, where “1”, “2”, and “3” represent the Cartesian axes of the material. For the sake of brevity, the expressions for the coefficients \tilde{C}_{ij} are not reported here, but they can be found in standard texts, see for example Tsai [159] and Reddy [133]. More generally, in the case of anisotropic materials, matrix $\tilde{\mathbf{C}}$ is fully populated, see [28]. Furthermore, it should be underlined that models with constant and linear distributions of the in-plane displacement components, u_x and u_z , require modified material coefficients to overcome Poisson locking, see [26]. The explicit expressions of the reduced material coefficients is not reported here; the reader is referred to [33], where they are given together with a more comprehensive analysis of the effect of Poisson locking and its correction.

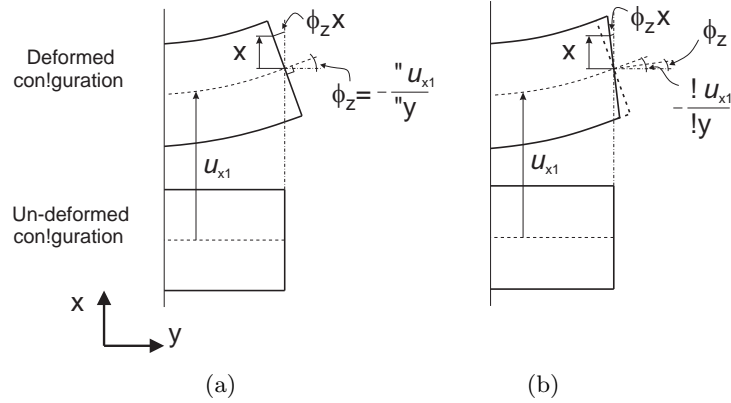


Figure 2.3: Differences between Euler-Bernoulli (a) and Timoshenko (b) beam theories

2.2 From classical to variable kinematic beam theories

A number of refined beam theories have been proposed over the years to overcome the limitations of classical beam models, as already mentioned in the introductory section. According to the rectangular Cartesian coordinate system shown in Fig. 2.1, and considering a beam under bending on the xy -plane, the kinematic field of EBBM (Euler-Bernoulli Beam Model) can be written as:

$$\begin{aligned} u_x &= u_{x1} \\ u_y &= u_{y1} - x \frac{\partial u_{x1}}{\partial y} \end{aligned} \quad (2.7)$$

where u_x and u_y are the displacement components of a point belonging to the beam domain along x and y , respectively. u_{x1} and u_{y1} are the displacements of the beam axis, whereas $-\frac{\partial u_{x1}}{\partial y}$ is the rotation of the cross-section about the z -axis (i.e. ϕ_z) as shown in Fig. 2.3a. According to EBBM, the deformed cross-section remains plane and orthogonal to the beam axis. EBBM neglects the cross-sectional shear deformation phenomena. Shear stresses play an important role in several problems (e.g. short beams, composite structures) and their neglect can lead to incorrect results. One may want to generalize Eq. (2.7) and overcome the EBBM assumption of the orthogonality of the cross-section. The improved displacement field results in the TBM (Timoshenko Beam Model),

$$\begin{aligned} u_x &= u_{x1} \\ u_y &= u_{y1} + x \phi_z \end{aligned} \quad (2.8)$$

TBM constitutes an improvement over EBBM since the cross-section does not necessarily remain perpendicular to the beam axis after deformation and one degree of freedom (i.e. the unknown rotation ϕ_z) is added to the original displacement field (see Fig. 2.3b).

As already discussed in Section 1.2 and in [115], classical beam theories are reliable only for a narrow range of problems, such as bending of slender, solid structures. When more complex phenomena are analysed, refined kinematics may be necessary. For example, one of the main problems of TBM is that the homogeneous conditions of the transverse stress components at the top/bottom surfaces of the beam are not fulfilled, as shown in Fig. 2.4. One can impose, for instance, Eq. (2.8) in order to have null transverse strain components ($\gamma_{xy} = \frac{\partial u_x}{\partial y} + \frac{\partial u_y}{\partial x}$) at $x = \pm \frac{b}{2}$. This leads to the third-order displacement field

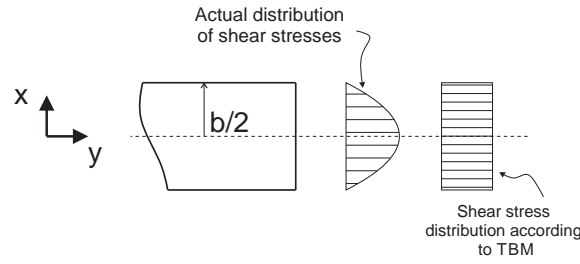


Figure 2.4: Homogeneous condition of transverse stress components at the unloaded edges of the beam

known as the Reddy-Vlasov beam theory [164, 91],

$$\begin{aligned} u_x &= u_{x1} \\ u_y &= u_{y1} + f_1(x) \phi_z + g_1(x) \frac{\partial u_{x1}}{\partial y} \end{aligned} \quad (2.9)$$

where $f_1(x)$ and $g_1(x)$ are cubic functions of the x coordinate. It should be noted that although the model of Eq. (2.9) has the same number of degrees of freedom of TBM, it overcomes classical beam theory limitations by foreseeing a quadratic distribution of transverse stresses on the cross-section of the beam.

The above theories are not able to include any kinematics resulting from the application of torsional moments. The simplest way to include torsion consists of considering a rigid rotation of the cross-section around the y -axis (i.e. ϕ_y), see Fig. 2.5. The resulting displacement model is:

$$\begin{aligned} u_x &= z \phi_y \\ u_z &= -x \phi_y \end{aligned} \quad (2.10)$$

where u_z is the displacement component along the z -axis. According to Eq. (2.10), a linear distribution of transverse displacement components is needed to detect the rigid rotation of the cross-section about the beam axis. Beam models that include all the aforementioned capabilities can be obtained by summing all the contributions discussed above. By considering the deformations also in the yz -plane, one has

$$\begin{aligned} u_x &= u_{x1} + z \phi_y \\ u_y &= u_{y1} + f_1(x) \phi_z + f_2(z) \phi_x + g_1(x) \left(\frac{\partial u_{x1}}{\partial y} + z \frac{\phi_y}{\partial y} \right) + g_2(z) \left(\frac{\partial u_{z1}}{\partial y} - x \frac{\phi_y}{\partial y} \right) \\ u_z &= u_{z1} - x \phi_y \end{aligned} \quad (2.11)$$

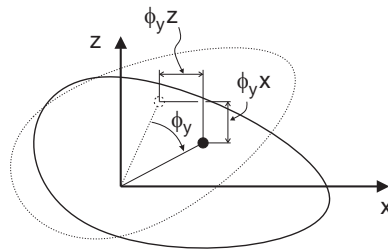


Figure 2.5: Rigid torsion of the beam cross-section

N	M	F_τ
0	1	$F_1 = 1$
1	3	$F_2 = x \ F_3 = z$
2	6	$F_4 = x^2 \ F_5 = xz \ F_6 = z^2$
3	10	$F_7 = x^3 \ F_8 = x^2z \ F_9 = xz^2 \ F_{10} = z^3$
\vdots	\vdots	\vdots
N	$\frac{(N+1)(N+2)}{2}$	$F_{(N^2+N+2)/2} = x^N \ F_{(N^2+N+4)/2} = x^{N-1} \dots \ F_{N(N+3)/2} = xz^{N-1} \ F_{(N+1)(N+2)/2} = z^N$

Table 2.1: MacLaurin's polynomials

where $f_1(x)$, $g_1(x)$, $f_2(z)$, and $g_2(z)$ are cubic functions¹.

These beam models, however, are not able to account for many *higher-order effects*, such as the second-order in-plane deformations of the cross-section. As discussed in Section 1.2, many refined beam theories have been proposed over the last century to overcome the limitations of classical beam modelling. Nonetheless, as a general guideline, one can state that the richer the kinematic field, the most accurate the 1D model becomes [169]. However, richer displacement fields lead to a higher amount of equations to be solved and, moreover, the choice of the additional expansion terms is problem dependent.

2.2.1 Taylor Expansion (TE)

According to Carrera Unified Formulation (CUF), the generic displacement field can be expressed in a compact manner as an expansion in terms of arbitrary functions, F_τ ,

$$\mathbf{u}(x, y, z) = F_\tau(x, z)\mathbf{u}_\tau(y), \quad \tau = 1, 2, \dots, M \quad (2.12)$$

where F_τ are the functions of the coordinates x and z on the cross-section; \mathbf{u}_τ is the vector of the *generalized displacements*; M stands for the number of terms used in the expansion; and the repeated subscript, τ , indicates summation. The choice of F_τ determines the class of the 1D CUF model.

Taylor Expansion (TE) 1D CUF models consists of MacLaurin series that uses the 2D polynomials $x^i z^j$ as F_τ basis. Table 2.1 shows M and F_τ as functions of the expansion order, N , which represents the maximum order of the polynomials used in the expansion.

According to CUF, Eqs. (2.7) to (2.11) consist of particular cases of TE theories. For example, it should be noted that Eqs. (2.7), (2.8), and (2.10) are degenerated cases of the linear ($N = 1$) TE model, which can be expressed as

$$\begin{aligned} u_x &= u_{x_1} + x u_{x_2} + z u_{x_3} \\ u_y &= u_{y_1} + x u_{y_2} + z u_{y_3} \\ u_z &= u_{z_1} + x u_{z_2} + z u_{z_3} \end{aligned} \quad (2.13)$$

where the parameters on the right-hand side (u_{x_1} , u_{y_1} , u_{z_1} , u_{x_2} , etc.) are the displacements of the beam axis and first derivatives of displacements. Higher-order terms can be taken into account according to Eq. (2.12). For instance, the displacement fields of Eqs. (2.9)

¹ In the case of rectangular cross-section, the cubic functions from Vlasov's theory are

$$f_1(x) = x - \frac{4}{3b^2}x^3, \quad g_1(x) = -\frac{4}{3b^2}x^3, \quad f_2(z) = z - \frac{4}{3h^2}z^3, \quad g_2(z) = -\frac{4}{3h^2}z^3$$

where b and h are the dimensions of the cross-section along the x - and z -axis, respectively.

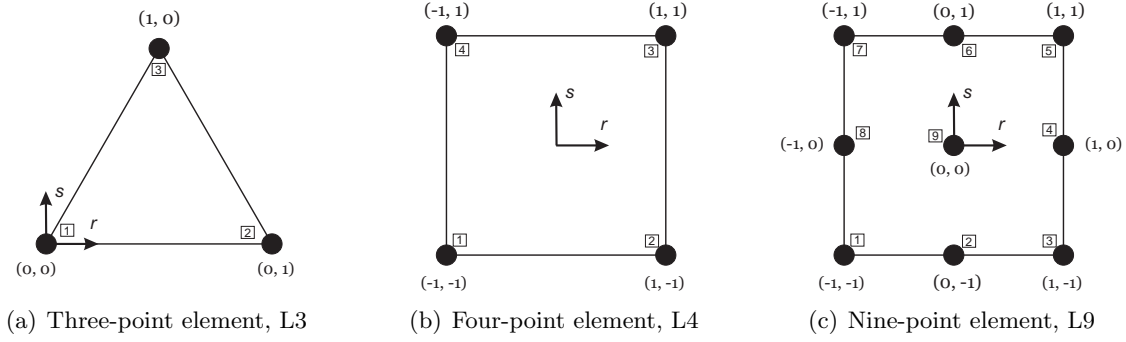


Figure 2.6: Cross-section L-elements in natural geometry

and (2.11) can be considered as particular cases of the third-order ($N = 3$) TE model,

$$\begin{aligned}
 u_x &= u_{x_1} + x u_{x_2} + z u_{x_3} + x^2 u_{x_4} + xz u_{x_5} + z^2 u_{x_6} + x^3 u_{x_7} + x^2 z u_{x_8} + xz^2 u_{x_9} + z^3 u_{x_{10}} \\
 u_y &= u_{y_1} + x u_{y_2} + z u_{y_3} + x^2 u_{y_4} + xz u_{y_5} + z^2 u_{y_6} + x^3 u_{y_7} + x^2 z u_{y_8} + xz^2 u_{y_9} + z^3 u_{y_{10}} \\
 u_z &= u_{z_1} + x u_{z_2} + z u_{z_3} + x^2 u_{z_4} + xz u_{z_5} + z^2 u_{z_6} + x^3 u_{z_7} + x^2 z u_{z_8} + xz^2 u_{z_9} + z^3 u_{z_{10}}
 \end{aligned} \tag{2.14}$$

A more comprehensive treatise about TE CUF models can be found in [33], where details about the derivation of classical models from the linear ($N = 1$) TE model and various numerical experiments are also given.

2.3 Lagrange Expansion (LE)

In this work, another CUF class of models has played an important role and it is referred to as Lagrange Expansion (LE) class. The LE models exploit Lagrange polynomials to build 1D higher-order models; i.e., as F_τ cross-sectional functions. In this thesis, three types of cross-sectional polynomial sets have been adopted as shown in Fig. 2.6: three-point elements (L3), four-point elements (L4), and nine-point elements (L9). The isoparametric formulation is exploited to deal with arbitrarily shaped geometries. The Lagrange polynomial expansions can be found in Ref. [117], although the interpolation functions in the case of an L4 element are given in the following as an example:

$$F_\tau = \frac{1}{4}(1 + r r_\tau)(1 + s s_\tau) \quad \tau = 1,2,3,4 \tag{2.15}$$

where r and s vary from -1 to $+1$, whereas r_τ and s_τ are the coordinates of the four points whose numbering and location in the natural coordinate frame are shown in Fig. 2.6b. The displacement field of a beam model described by one single L4 element is

$$\begin{aligned}
 u_x &= F_1 u_{x_1} + F_2 u_{x_2} + F_3 u_{x_3} + F_4 u_{x_4} \\
 u_y &= F_1 u_{y_1} + F_2 u_{y_2} + F_3 u_{y_3} + F_4 u_{y_4} \\
 u_z &= F_1 u_{z_1} + F_2 u_{z_2} + F_3 u_{z_3} + F_4 u_{z_4}
 \end{aligned} \tag{2.16}$$

where u_{x_1}, \dots, u_{z_4} are the displacement variables of the problem and represent the translational displacement components of each of the four points of the L4 element. For further refinements, the cross-section can be discretized by using several L-elements as in Fig. 2.7, where two assembled L9 elements are shown.

Further details about LE models can be found in the original work by Carrera and Petrolo [47] and in [44]. In this thesis, LE models are exploited to build component-wise

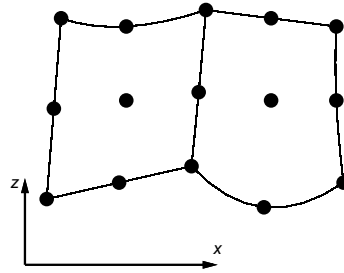


Figure 2.7: Two assembled L9 elements in actual geometry

models of complex structures as described in Chapter 5, where more details about LE and its differences with respect to TE can also be found.

Chapter 3

Strong Form Solutions for Free Vibrations

Free vibration analysis is an important aspect of engineering. In the design of aircraft structures, for example, the results of modal analysis are generally used to compute the aeroelastic properties and the dynamic response of a wing or to evaluate the acoustic performance of the fuselage. Moreover, avoiding resonance failures is a major concern in every structure project. For these reasons, accurate solutions and models that can accurately describe the dynamic behavior of complex structures, such as aerospace ones, are needed. In this chapter, the equations of motion for higher-order CUF models in free vibration are provided. Strong form solutions are then sought both exactly, by applying the dynamic stiffness method, and approximately, by collocating the unknowns and their derivatives via radial basis functions.

3.1 Equations of motion of the N-order TE model

The principle of virtual displacements is generally used in this thesis to derive the equilibrium equations. In the case of a beam in free vibration, it holds

$$\delta L_{\text{int}} = \int_V \delta \boldsymbol{\epsilon}^T \boldsymbol{\sigma} \, dV = -\delta L_{\text{ine}} \quad (3.1)$$

where L_{int} stands for the strain energy and δL_{ine} is the work done by the inertial loadings. δ stands for the virtual variation operator. The virtual variation of the strain energy can be written by using Eqs. (2.3), (2.5) and (2.12). After integrations by part, it reads

$$\delta L_{\text{int}} = \int_L \delta \mathbf{u}_\tau^T \mathbf{K}^{\tau s} \mathbf{u}_s \, dy + \left[\delta \mathbf{u}_\tau^T \boldsymbol{\Pi}^{\tau s} \mathbf{u}_s \right]_{y=0}^{y=L} \quad (3.2)$$

where $\mathbf{K}^{\tau s}$ is the differential linear stiffness matrix and $\boldsymbol{\Pi}^{\tau s}$ is the matrix of the natural boundary conditions in the form of 3×3 fundamental nuclei. The components of $\mathbf{K}^{\tau s}$ are provided in the following in the case of orthotropic material and they are referred to as $K_{(ij)}^{\tau s}$, where i is the row number ($i = 1, 2, 3$) and j denotes the column number

($j = 1, 2, 3$):

$$\begin{aligned}
 K_{(11)}^{\tau s} &= E_{\tau, x s, x}^{22} + E_{\tau, z s, z}^{44} + (E_{\tau, x s}^{26} - E_{\tau s, x}^{26}) \frac{\partial}{\partial y} - E_{\tau s}^{66} \frac{\partial^2}{\partial y^2} \\
 K_{(12)}^{\tau s} &= E_{\tau, x s, x}^{26} + E_{\tau, z s, z}^{45} + (E_{\tau, x s}^{23} - E_{\tau s, x}^{66}) \frac{\partial}{\partial y} - E_{\tau s}^{36} \frac{\partial^2}{\partial y^2} \\
 K_{(13)}^{\tau s} &= E_{\tau, x s, z}^{12} + E_{\tau, z s, x}^{44} + (E_{\tau, z s}^{45} - E_{\tau s, z}^{16}) \frac{\partial}{\partial y} \\
 K_{(21)}^{\tau s} &= E_{\tau, x s, x}^{26} + E_{\tau, z s, z}^{45} + (E_{\tau, x s}^{66} - E_{\tau s, x}^{23}) \frac{\partial}{\partial y} - E_{\tau s}^{36} \frac{\partial^2}{\partial y^2} \\
 K_{(22)}^{\tau s} &= E_{\tau, x s, x}^{66} + E_{\tau, z s, z}^{55} + (E_{\tau, x s}^{36} - E_{\tau s, x}^{36}) \frac{\partial}{\partial y} - E_{\tau s}^{33} \frac{\partial^2}{\partial y^2} \\
 K_{(23)}^{\tau s} &= E_{\tau, x s, z}^{16} + E_{\tau, z s, x}^{45} + (E_{\tau, z s}^{55} - E_{\tau s, z}^{13}) \frac{\partial}{\partial y} \\
 K_{(31)}^{\tau s} &= E_{\tau, x s, z}^{44} + E_{\tau, z s, x}^{12} + (E_{\tau, z s}^{16} - E_{\tau s, z}^{45}) \frac{\partial}{\partial y} \\
 K_{(32)}^{\tau s} &= E_{\tau, x s, z}^{45} + E_{\tau, z s, x}^{16} + (E_{\tau, z s}^{13} - E_{\tau s, z}^{55}) \frac{\partial}{\partial y} \\
 K_{(33)}^{\tau s} &= E_{\tau, x s, x}^{44} + E_{\tau, z s, z}^{11} + (E_{\tau, x s}^{45} - E_{\tau s, x}^{45}) \frac{\partial}{\partial y} - E_{\tau s}^{55} \frac{\partial^2}{\partial y^2}
 \end{aligned} \tag{3.3}$$

The generic term $E_{\tau, \theta s, \zeta}^{\alpha \beta}$ above is a cross-sectional moment parameter

$$E_{\tau, \theta s, \zeta}^{\alpha \beta} = \int_{\Omega} \tilde{C}_{\alpha \beta} F_{\tau, \theta} F_{s, \zeta} \, d\Omega \tag{3.4}$$

The suffix after the comma in Eq. (3.3) denotes the derivatives. As far as the boundary conditions are concerned, the components of $\mathbf{\Pi}^{\tau s}$ are

$$\begin{aligned}
 \Pi_{(11)}^{\tau s} &= E_{\tau s, x}^{26} + E_{\tau s}^{66} \frac{\partial}{\partial y}, & \Pi_{(12)}^{\tau s} &= E_{\tau s, x}^{66} + E_{\tau s}^{36} \frac{\partial}{\partial y}, & \Pi_{(13)}^{\tau s} &= E_{\tau s, z}^{16} \\
 \Pi_{(21)}^{\tau s} &= E_{\tau s, x}^{23} + E_{\tau s}^{36} \frac{\partial}{\partial y}, & \Pi_{(22)}^{\tau s} &= E_{\tau s, x}^{36} + E_{\tau s}^{33} \frac{\partial}{\partial y}, & \Pi_{(23)}^{\tau s} &= E_{\tau s, z}^{13} \\
 \Pi_{(31)}^{\tau s} &= E_{\tau s, z}^{45}, & \Pi_{(32)}^{\tau s} &= E_{\tau s, z}^{55}, & \Pi_{(33)}^{\tau s} &= E_{\tau s, x}^{45} + E_{\tau s}^{55} \frac{\partial}{\partial y}
 \end{aligned} \tag{3.5}$$

The main property of the fundamental nuclei is that their formal mathematical expression does not depend either on the order of the beam theory or on the geometry of the problem.

The virtual variation of the inertial work is given by

$$\delta L_{\text{ine}} = \int_L \delta \mathbf{u}_{\tau} \int_{\Omega} \rho F_{\tau} F_s \, d\Omega \, \ddot{\mathbf{u}}_s \, dy = \int_L \delta \mathbf{u}_{\tau} \mathbf{M}^{\tau s} \ddot{\mathbf{u}}_s \, dy \tag{3.6}$$

where $\mathbf{M}^{\tau s}$ is the fundamental nucleus of the mass matrix and double over dots stand as second derivative with respect to time (t). The components of matrix $\mathbf{M}^{\tau s}$ are

$$\begin{aligned}
 M_{(11)}^{\tau s} &= M_{(22)}^{\tau s} = M_{(33)}^{\tau s} = E_{\tau s}^{\rho} \\
 M_{(12)}^{\tau s} &= M_{(13)}^{\tau s} = M_{(21)}^{\tau s} = M_{(23)}^{\tau s} = M_{(31)}^{\tau s} = M_{(32)}^{\tau s} = 0
 \end{aligned} \tag{3.7}$$

where ρ is the material density and

$$E_{\tau s}^{\rho} = \int_{\Omega} \rho F_{\tau} F_s \, d\Omega \tag{3.8}$$

The governing equations of the undamped dynamic problem can be therefore written in the following compact form:

$$\delta \mathbf{u}_\tau : \mathbf{K}^{\tau s} \mathbf{u}_s = -\mathbf{M}^{\tau s} \ddot{\mathbf{u}}_s \quad (3.9)$$

where $\mathbf{u}_s = \{u_{xs} \ u_{ys} \ u_{zs}\}^T$ is the vector of the unknown generalised displacements and $\delta \mathbf{u}_\tau$ the corresponding virtual variation. Letting $\mathbf{P}_\tau(y; t) = \{P_{x\tau} \ P_{y\tau} \ P_{z\tau}\}^T$ to be the vector of the generalized forces applied at the ends of the beam, the natural boundary conditions are

$$\delta \mathbf{u}_\tau : \mathbf{P}_s = \mathbf{\Pi}^{\tau s} \mathbf{u}_s \quad (3.10)$$

For a fixed theory order N , Eqs. (3.9) and (3.10) have to be expanded using the indices τ and s from 1 to $M = (N + 1)(N + 2)/2$ in order to obtain the equations of motion and the natural boundary conditions of the desired model.

The strong form of the equations of motion of the higher-order beam in free vibration have been solved both in closed-form and numerically in the present thesis. In the former case, we use the Dynamic Stiffness Method (DSM), which brings to a non-linear eigenvalue problem. On the other hand, we describe the Radial Basis Functions (RBFs) method for approximate solutions.

3.2 Dynamic Stiffness Method (DSM)

The procedure to obtain the Dynamic Stiffness (DS) matrix for a structural problem can be summarised as follows: (i) Seek a closed form analytical solution of the governing differential equations of motion of the structural element in free vibration; (ii) Apply a number of general boundary conditions equal to twice the number of integration constants in algebraic form that are usually the nodal displacements and forces; (iii) Eliminate the integration constants by relating the harmonically varying amplitudes of the generalized nodal forces to the corresponding generalized displacements that generates the frequency dependent DS matrix.

These passages are briefly described below and the DS matrix is formulated. The Wittrick-Williams algorithm is finally introduced as an effective methodology to solve transcendental eigenvalue problems.

3.2.1 Solution of the differential equations

In the case of harmonic motion, the solution of Eqs. (3.9) is sought in the form

$$\mathbf{u}_s(y; t) = \mathbf{U}_s(y) e^{i\omega t} \quad (3.11)$$

where $\mathbf{U}_s(y)$ is the amplitude function of the motion, ω is an arbitrary circular or angular frequency, and i is the imaginary unit. Equation (3.11) allows the formulation of the equilibrium equations and the natural boundary conditions in the frequency domain. Substituting Eq. (3.11) into Eq. (3.9), a set of three coupled ordinary differential equations (ODEs) is obtained which can be written in a matrix form as follows:

$$\delta \mathbf{U}_\tau : \mathbf{L}^{\tau s} \tilde{\mathbf{U}}_s = 0 \quad (3.12)$$

where

$$\tilde{\mathbf{U}}_s = \{ U_{xs} \ U_{xs,y} \ U_{xs,yy} \ U_{ys} \ U_{ys,y} \ U_{ys,yy} \ U_{zs} \ U_{zs,y} \ U_{zs,yy} \}^T \quad (3.13)$$

and $\mathbf{L}^{\tau s}$ is the 3×9 fundamental nucleus of the matrix containing the coefficients of the ordinary differential equations. The components of matrix $\mathbf{L}^{\tau s}$ are provided below in the case of orthotropic materials and they are referred to as $L_{(ij)}^{\tau s}$, where i is the row number ($i = 1, 2, 3$) and j is the column number ($j = 1, 2, \dots, 9$)

$$\begin{aligned}
 L_{(11)}^{\tau s} &= -\omega^2 E_{\tau s}^{\rho} + E_{\tau, x s, x}^{22} + E_{\tau, z s, z}^{44}, & L_{(12)}^{\tau s} &= E_{\tau, x s}^{26} - E_{\tau s, x}^{26}, & L_{(13)}^{\tau s} &= -E_{\tau s}^{66} \\
 L_{(14)}^{\tau s} &= E_{\tau, x s, x}^{26} + E_{\tau, z s, z}^{45}, & L_{(15)}^{\tau s} &= E_{\tau s, x}^{23} - E_{\tau s, x}^{66}, & L_{(16)}^{\tau s} &= -E_{\tau s}^{36} \\
 L_{(17)}^{\tau s} &= E_{\tau, x s, z}^{12} + E_{\tau, z s, x}^{44}, & L_{(18)}^{\tau s} &= E_{\tau, z s}^{45} - E_{\tau s, z}^{16}, & L_{(19)}^{\tau s} &= 0 \\
 L_{(21)}^{\tau s} &= E_{\tau, x s, x}^{26} + E_{\tau, z s, z}^{45}, & L_{(22)}^{\tau s} &= E_{\tau, x s}^{66} - E_{\tau s, x}^{23}, & L_{(23)}^{\tau s} &= -E_{\tau s}^{36} \\
 L_{(24)}^{\tau s} &= -\omega^2 E_{\tau s}^{\rho} + E_{\tau, x s, x}^{66} + E_{\tau, z s, z}^{55}, & L_{(25)}^{\tau s} &= E_{\tau, x s}^{36} - E_{\tau s, x}^{36}, & L_{(26)}^{\tau s} &= -E_{\tau s}^{33} \\
 L_{(27)}^{\tau s} &= E_{\tau, x s, z}^{16} + E_{\tau, z s, x}^{45}, & L_{(28)}^{\tau s} &= E_{\tau, z s}^{55} - E_{\tau s, z}^{13}, & L_{(29)}^{\tau s} &= 0 \\
 L_{(31)}^{\tau s} &= E_{\tau, x s, z}^{44} + E_{\tau, z s, x}^{12}, & L_{(32)}^{\tau s} &= E_{\tau, z s, x}^{16} - E_{\tau s, z}^{45}, & L_{(33)}^{\tau s} &= 0 \\
 L_{(34)}^{\tau s} &= E_{\tau, x s, z}^{45} + E_{\tau, z s, x}^{16}, & L_{(35)}^{\tau s} &= E_{\tau, z s}^{13} - E_{\tau s, z}^{55}, & L_{(36)}^{\tau s} &= 0 \\
 L_{(37)}^{\tau s} &= -\omega^2 E_{\tau s}^{\rho} + E_{\tau, x s, x}^{44} + E_{\tau, z s, z}^{11}, & L_{(38)}^{\tau s} &= E_{\tau, x s}^{45} - E_{\tau s, x}^{45}, & L_{(39)}^{\tau s} &= -E_{\tau s}^{55}
 \end{aligned} \tag{3.14}$$

For a given expansion order, N , the equations of motion in the frequency domain can be obtained in the form of Eq. (3.15), as given below, by expanding $\mathbf{L}^{\tau s}$ for indexes τ and s . It reads:

$$\mathbf{L} \hat{\mathbf{U}} = 0 \tag{3.15}$$

Note that the matrix \mathbf{L} is hierarchical. This means that the \mathbf{L} matrix related to the N -order model actually contains the \mathbf{L} matrix related to the $(N - 1)$ -order beam model.

Similarly as above, the boundary conditions of Eqs. (3.10) can be written in a matrix form as

$$\delta \mathbf{U}_{\tau} : \mathbf{P}_s = \mathbf{B}^{\tau s} \hat{\mathbf{U}}_s \tag{3.16}$$

where

$$\hat{\mathbf{U}}_s = \{ U_{xs} \quad U_{xs,y} \quad U_{ys} \quad U_{ys,y} \quad U_{zs} \quad U_{zs,y} \}^T \tag{3.17}$$

and $\mathbf{B}^{\tau s}$ is the 3×6 fundamental nucleus which contains the coefficients of the natural boundary conditions

$$\mathbf{B}^{\tau s} = \begin{bmatrix} E_{\tau s, x}^{26} & E_{\tau s}^{66} & E_{\tau s, x}^{66} & E_{\tau s}^{36} & E_{\tau s, z}^{16} & 0 \\ E_{\tau s, x}^{23} & E_{\tau s}^{36} & E_{\tau s, x}^{36} & E_{\tau s}^{33} & E_{\tau s, z}^{13} & 0 \\ E_{\tau s, z}^{45} & 0 & E_{\tau s, z}^{55} & 0 & E_{\tau s, x}^{45} & E_{\tau s}^{55} \end{bmatrix} \tag{3.18}$$

For a given expansion order, N , the natural boundary conditions can be obtained in the form of Eq. (3.19) by expanding $\mathbf{B}^{\tau s}$ in the same way as $\mathbf{L}^{\tau s}$ to finally give

$$\mathbf{P} = \mathbf{B} \hat{\mathbf{U}} \tag{3.19}$$

Equation (3.15) is a system of ODEs of second order in y with constant coefficients. A change of variables is used to reduce the second order system of ODEs to a first order system,

$$\mathbf{Z} = \{ Z_1 \quad Z_2 \quad \dots \quad Z_n \}^T = \hat{\mathbf{U}} = \{ U_{x1} \quad U_{x1,y} \quad U_{y1} \quad U_{y1,y} \quad U_{z1} \quad U_{z1,y} \quad \dots \quad U_{xM} \quad U_{xM,y} \quad U_{yM} \quad U_{yM,y} \quad U_{zM} \quad U_{zM,y} \}^T \quad (3.20)$$

where $\hat{\mathbf{U}}$ is the expansion of $\hat{\mathbf{U}}_s$ for a given theory order, M is the number of expansion terms for the given N -order beam theory, and $n = 6 \times M$ is the dimension of the unknown vector as well as the number of differential equations. In [119], an automatic algorithm to transform the \mathbf{L} matrix of Eq. (3.15) into the matrix \mathbf{S} of the following linear differential system was described:

$$\mathbf{Z}_{,y}(y) = \mathbf{S}\mathbf{Z}(y) \quad (3.21)$$

Once the differential problem is described in terms of Eq. (3.21), the solution can be written as follows:

$$\begin{bmatrix} Z_1 \\ Z_2 \\ \vdots \\ Z_n \end{bmatrix} = \begin{bmatrix} \delta_{11} & \delta_{21} & \dots & \delta_{n1} \\ \delta_{12} & \delta_{22} & \dots & \delta_{n2} \\ \vdots & \vdots & \ddots & \vdots \\ \delta_{1n} & \delta_{2n} & \dots & \delta_{nn} \end{bmatrix} \begin{bmatrix} C_1 e^{\lambda_1 y} \\ C_2 e^{\lambda_2 y} \\ \vdots \\ C_n e^{\lambda_n y} \end{bmatrix} \quad (3.22)$$

where λ_i is the i -th eigenvalue of the \mathbf{S} matrix, δ_{ij} is the j -th element of the i -th eigenvector of the \mathbf{S} matrix and C_i are the integration constants which need to be determined by using the boundary conditions. The above equation can be written in a matrix form as follows:

$$\mathbf{Z} = \boldsymbol{\delta}\mathbf{C}e^{\boldsymbol{\lambda}y} \quad (3.23)$$

Vector \mathbf{Z} does not only contain the displacements but also their first derivatives. If only the displacements are needed, according to Eq. (3.20), only the lines 1,3,5, ..., $n-1$ should be taken into account, giving a solution in the following form:

$$\begin{aligned} U_{x1}(y) &= C_1 \delta_{11} e^{\lambda_1 y} + C_2 \delta_{21} e^{\lambda_2 y} + \dots + C_n \delta_{n1} e^{\lambda_n y} \\ U_{y1}(y) &= C_1 \delta_{13} e^{\lambda_1 y} + C_2 \delta_{23} e^{\lambda_2 y} + \dots + C_n \delta_{n3} e^{\lambda_n y} \\ U_{z1}(y) &= C_1 \delta_{15} e^{\lambda_1 y} + C_2 \delta_{25} e^{\lambda_2 y} + \dots + C_n \delta_{n5} e^{\lambda_n y} \\ &\vdots \\ U_{zM}(y) &= C_1 \delta_{1(n-1)} e^{\lambda_1 y} + C_2 \delta_{2(n-1)} e^{\lambda_2 y} + \dots + C_n \delta_{n(n-1)} e^{\lambda_n y} \end{aligned} \quad (3.24)$$

Once the displacements are known, the boundary conditions are obtained by substituting the solution of Eq. (3.23) into the boundary conditions (Eq. (3.19)). In fact, it should be noted that $\hat{\mathbf{U}}$ is equal to \mathbf{Z} (Eq. (3.20)). It reads

$$\mathbf{P} = \mathbf{B}\boldsymbol{\delta}\mathbf{C}e^{\boldsymbol{\lambda}y} = \boldsymbol{\Lambda}\mathbf{C}e^{\boldsymbol{\lambda}y} \quad (3.25)$$

where $\boldsymbol{\Lambda} = \mathbf{B}\boldsymbol{\delta}$. The boundary conditions can be written in explicit form as follows:

$$\begin{aligned} P_{x1}(y) &= C_1 \Lambda_{11} e^{\lambda_1 y} + C_2 \Lambda_{12} e^{\lambda_2 y} + \dots + C_n \Lambda_{1n} e^{\lambda_n y} \\ P_{y1}(y) &= C_1 \Lambda_{21} e^{\lambda_1 y} + C_2 \Lambda_{22} e^{\lambda_2 y} + \dots + C_n \Lambda_{2n} e^{\lambda_n y} \\ P_{z1}(y) &= C_1 \Lambda_{31} e^{\lambda_1 y} + C_2 \Lambda_{32} e^{\lambda_2 y} + \dots + C_n \Lambda_{3n} e^{\lambda_n y} \\ &\vdots \\ P_{zM}(y) &= C_1 \Lambda_{n1} e^{\lambda_1 y} + C_2 \Lambda_{n2} e^{\lambda_2 y} + \dots + C_n \Lambda_{nn} e^{\lambda_n y} \end{aligned} \quad (3.26)$$

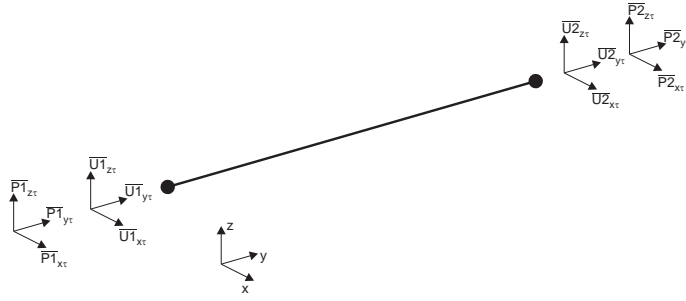


Figure 3.1: Boundary conditions of the beam element and sign conventions

3.2.2 Dynamic stiffness matrix

Once the closed form analytical solution of the differential equations of motion of the structural element in free vibration has been sought, a number of general boundary conditions - which are usually the nodal displacements and forces - equal to twice the number of integration constants in algebraic form needs to be applied (see Fig. 3.1).

Starting from the displacements, the boundary conditions can be written as

$$\begin{aligned}
 \text{At } y = 0 : \\
 U_{x1}(0) &= -\bar{U}1_{x1} \\
 U_{y1}(0) &= -\bar{U}1_{y1} \\
 U_{z1}(0) &= -\bar{U}1_{z1} \\
 &\vdots \\
 U_{zM}(0) &= -\bar{U}1_{zM}
 \end{aligned} \tag{3.27}$$

$$\begin{aligned}
 \text{At } y = L : \\
 U_{x1}(L) &= \bar{U}2_{x1} \\
 U_{y1}(L) &= \bar{U}2_{y1} \\
 U_{z1}(L) &= \bar{U}2_{z1} \\
 &\vdots \\
 U_{zM}(L) &= \bar{U}2_{zM}
 \end{aligned} \tag{3.28}$$

By evaluating Eqs. (3.24) in $y = 0$ and $y = L$ and applying the boundary conditions of Eqs. (3.27) and (3.28), the following matrix relation for the nodal generalized displacements is obtained:

$$\begin{Bmatrix} \bar{U}1_{x1} \\ \bar{U}1_{y1} \\ \bar{U}1_{z1} \\ \vdots \\ \bar{U}1_{zM} \\ \bar{U}2_{x1} \\ \bar{U}2_{y1} \\ \bar{U}2_{z1} \\ \vdots \\ \bar{U}2_{zM} \end{Bmatrix} = \begin{bmatrix} -\delta_{11} & -\delta_{21} & \dots & -\delta_{n1} \\ -\delta_{13} & -\delta_{23} & \dots & -\delta_{n3} \\ -\delta_{15} & -\delta_{25} & \dots & -\delta_{n5} \\ \vdots & \vdots & \ddots & \vdots \\ -\delta_{1(n-1)} & -\delta_{2(n-1)} & \dots & -\delta_{n(n-1)} \\ \delta_{11}e^{\lambda_1 L} & \delta_{21}e^{\lambda_2 L} & \dots & \delta_{n1}e^{\lambda_n L} \\ \delta_{13}e^{\lambda_1 L} & \delta_{23}e^{\lambda_2 L} & \dots & \delta_{n3}e^{\lambda_n L} \\ \delta_{15}e^{\lambda_1 L} & \delta_{25}e^{\lambda_2 L} & \dots & \delta_{n5}e^{\lambda_n L} \\ \vdots & \vdots & \ddots & \vdots \\ \delta_{1(n-1)}e^{\lambda_1 L} & \delta_{2(n-1)}e^{\lambda_2 L} & \dots & \delta_{n(n-1)}e^{\lambda_n L} \end{bmatrix} \begin{Bmatrix} C_1 \\ C_2 \\ C_3 \\ \vdots \\ C_{\frac{n}{2}} \\ C_{\frac{n}{2}+1} \\ C_{\frac{n}{2}+2} \\ C_{\frac{n}{2}+3} \\ \vdots \\ C_n \end{Bmatrix} \tag{3.29}$$

The above equation can be written in a more compact form as

$$\bar{\mathbf{U}} = \mathbf{A}\mathbf{C} \tag{3.30}$$

Similarly, boundary conditions for generalized nodal forces are as follows:

$$\begin{aligned}
 \text{At } y = 0 : \\
 P_{x1}(0) &= -\bar{P}1_{x1} \\
 P_{y1}(0) &= -\bar{P}1_{y1} \\
 P_{z1}(0) &= -\bar{P}1_{z1} \\
 &\vdots \\
 P_{zM}(0) &= -\bar{P}1_{zM}
 \end{aligned} \tag{3.31}$$

$$\begin{aligned}
 \text{At } y = L : \\
 P_{x1}(L) &= \bar{P}2_{x1} \\
 P_{y1}(L) &= \bar{P}2_{y1} \\
 P_{z1}(L) &= \bar{P}2_{z1} \\
 &\vdots \\
 P_{zM}(L) &= \bar{P}2_{zM}
 \end{aligned} \tag{3.32}$$

By evaluating Eqs. (3.26) in $y = 0$ and $y = L$ and applying the boundary conditions of Eqs. (3.31) and (3.32), the following matrix relation for the nodal forces is obtained:

$$\begin{pmatrix} \bar{P}1_{x1} \\ \bar{P}1_{y1} \\ \bar{P}1_{z1} \\ \vdots \\ \bar{P}1_{M1} \\ \bar{P}2_{x1} \\ \bar{P}2_{y1} \\ \bar{P}2_{z1} \\ \vdots \\ \bar{P}2_{M1} \end{pmatrix} = \begin{bmatrix} -\Lambda_{11} & -\Lambda_{12} & \dots & -\Lambda_{1n} \\ -\Lambda_{21} & -\Lambda_{22} & \dots & -\Lambda_{2n} \\ -\Lambda_{31} & -\Lambda_{32} & \dots & -\Lambda_{3n} \\ \vdots & \vdots & \ddots & \vdots \\ -\Lambda_{n1} & -\Lambda_{n2} & \dots & -\Lambda_{nn} \\ \Lambda_{11}e^{\lambda_1 L} & \Lambda_{12}e^{\lambda_2 L} & \dots & \Lambda_{1n}e^{\lambda_n L} \\ \Lambda_{21}e^{\lambda_1 L} & \Lambda_{22}e^{\lambda_2 L} & \dots & \Lambda_{2n}e^{\lambda_n L} \\ \Lambda_{31}e^{\lambda_1 L} & \Lambda_{32}e^{\lambda_2 L} & \dots & \Lambda_{3n}e^{\lambda_n L} \\ \vdots & \vdots & \ddots & \vdots \\ \Lambda_{n1}e^{\lambda_1 L} & \Lambda_{n2}e^{\lambda_2 L} & \dots & \Lambda_{nn}e^{\lambda_n L} \end{bmatrix} \begin{pmatrix} C_1 \\ C_2 \\ C_3 \\ \vdots \\ C_{\frac{n}{2}} \\ C_{\frac{n}{2}+1} \\ C_{\frac{n}{2}+2} \\ C_{\frac{n}{2}+3} \\ \vdots \\ C_n \end{pmatrix} \tag{3.33}$$

The above equation can be written in a more compact form as

$$\bar{\mathbf{P}} = \mathbf{R}\mathbf{C} \tag{3.34}$$

The integration constants in vector \mathbf{C} from Eqs. (3.30) and (3.34) can now be eliminated by relating the harmonically varying amplitudes of the generalized nodal forces to the corresponding generalized displacements to give the DS matrix of one beam element as follows:

$$\bar{\mathbf{P}} = \mathbf{K}\bar{\mathbf{U}} \tag{3.35}$$

where

$$\mathbf{K} = \mathbf{R}\mathbf{A}^{-1} \tag{3.36}$$

is the required DS matrix.

The DS matrix given by Eq. (3.36) is the basic building block to compute the exact natural frequencies of a higher-order beam. The global DS matrix can be obtained by assembling elemental matrices as in the classical way of Finite Element Method (FEM) (see Chapter 4). As far as the boundary conditions are concerned, they can be applied by using the well-known penalty method (often used in FEM) or by simply removing rows and columns of the stiffness matrix corresponding to the degrees of freedom which are zeroes. In this paper, the penalty method is used and more details can be found in [119].

3.2.3 Application of the Wittrick-Williams algorithm

For free vibration analysis of structures, FEM and collocation methods, such as RBF method, lead to a linear eigenvalue problem. By contrast, the DSM leads to a transcendental (non-linear) eigenvalue problem for which the Wittrick-Williams algorithm [173] can be used. The basic working principle of the algorithm can be briefly summarised in the following steps:

- (i) A trial frequency ω^* is chosen to compute the DS matrix \mathcal{K}^* of the final structure;
- (ii) \mathcal{K}^* is reduced to its upper triangular form by the usual form of Gauss elimination to obtain $\mathcal{K}^{*\Delta}$ and the number of negative terms on the leading diagonal of $\mathcal{K}^{*\Delta}$ is counted; this is known as the sign count $s(\mathcal{K}^*)$ of the algorithm;
- (iii) The number, j , of natural frequencies (ω) of the structure which lie below the trial frequency (ω^*) is given by:

$$j = j_0 + s(\mathcal{K}^*) \quad (3.37)$$

where j_0 is the number of natural frequencies of all individual elements with clamped-clamped boundary conditions on their opposite sides which still lie below the trial frequency ω^* .

Note that j_0 is required because the DSM allows for an infinite number of natural frequencies to be accounted for when all the nodes of the structure are fully clamped so that one or more individual elements of the structure can still vibrate on their own between the nodes. j_0 corresponds to $\bar{\mathbf{U}} = 0$ modes of Eq. (3.35) when $\bar{\mathbf{P}} = 0$. Assuming that j_0 is known, and $s(\mathcal{K}^*)$ can be obtained by counting the number of negative terms in $\mathcal{K}^{*\Delta}$, a suitable procedure can be devised, for example the bi-section method, to bracket any natural frequency between an upper and lower bound of the trial frequency ω^* to any desired accuracy.

Once the natural frequency has been computed and the related global DS matrix evaluated, the corresponding nodal generalized displacements can be obtained by solving the associated homogeneous system of Eq. (3.35). By utilizing the nodal generalized displacements $\bar{\mathbf{U}}$, the integration constants \mathbf{C} of the element can be computed with the help of Eq. (3.30). In this way, using Eq. (3.24), the unknown generalized displacements can be computed as a function of y . Finally, by using Eqs. (3.11) and (2.12), the complete displacement field can be generated as a function of x, y, z and the time t (if an animated plot is needed). Clearly, the plot of the required mode and required element can be visualised on a fictitious 3D mesh. By following this procedure, it is possible to compute the exact mode shapes using just one single element, which is impossible in weak-form solutions and other numerical methods.

3.3 Radial Basis Functions (RBFs)

DSM, although interesting, exact and elegant from a mathematical point of view, requires an iterative procedure and faster approaches can be sometimes desirable at the expense of accuracy. In this thesis, RBFs functions method has been used for this reason.

RBFs approximations are collocation schemes that can exploit accurate representations of the boundary, are easy to implement and can be spectrally accurate. In solid mechanics, they are essentially used to approximate the unknowns derivatives and this is the case of the

methodology described hereinafter. For this purpose, Eqs. (3.12) and (3.16) are rewritten in the following equivalent forms:

$$\delta \mathbf{U}_\tau : (\mathbf{K}^{\tau s} - \omega^2 \mathbf{M}^{\tau s}) \mathbf{U}_s = 0 \quad (3.38)$$

$$\delta \mathbf{U}_\tau : \bar{\mathbf{P}}_s = \mathbf{\Pi}^{\tau s} \mathbf{U}_s \quad (3.39)$$

where matrices $\mathbf{K}^{\tau s}$, $\mathbf{\Pi}^{\tau s}$ and $\mathbf{M}^{\tau s}$ are those from Eqs. (3.3), (3.5) and (3.7), respectively. In Eq. (3.39) the load $\mathbf{P}_\tau(y; t)$ has been assumed harmonic with amplitude equal to $\bar{\mathbf{P}}_\tau(y)$.

In the framework of the RBFs method, the amplitude of the harmonically varying generalized displacement $\mathbf{U}_s(y)$ is approximated with a linear combination of the radial basis functions ϕ_i .

$$\mathbf{U}_s(y) = \alpha_{s i} \phi_i (\|y - y_i\|_2), \quad i = 1, \dots, n \quad (3.40)$$

where y_i is a finite set of n distinct points (centers) and $\|y - y_i\|_2$ is the Euclidian distance r_i , which in the case of 1D problems corresponds to $|y - y_i|$. In Eq. (3.40), index i indicates summation. Derivatives of $\mathbf{U}_s(y)$ over y can be treated similarly.

$$\begin{aligned} \mathbf{U}_{s,y}(y) &= \alpha_{s i} \phi_{i,y} (|y - y_i|), & i = 1, \dots, n \\ \mathbf{U}_{s,yy}(y) &= \alpha_{s i} \phi_{i,yy} (|y - y_i|), & i = 1, \dots, n \end{aligned} \quad (3.41)$$

In the present thesis, uniform and Chebyshev grid distributions of points y_i are used. The latter distribution, in particular, is known to be the best choice in terms of stability (see for example [79, 175, 78]). A Chebyshev grid is defined by

$$y_i = \frac{L}{2} \left[1 - \cos \left(\frac{i-1}{n-1} \pi \right) \right], \quad i = 1, \dots, n \quad (3.42)$$

Several RBFs have been formulated over the years and they are covered in a large literature. In the present work, locally supported Wendland's C^6 functions [170] are chosen as ϕ_i

$$\phi_i(r_i, c) = \max((1 - cr_i)^8, 0) + (32c^3r_i^3 + 25c^2r_i^2 + 8cr_i + 1) \quad (3.43)$$

where c is a positive shape parameter. The shape parameter c is known to play a very important role in collocation with RBFs for approximating functions and solving partial differential equations, see for example [137, 130]. The accuracy of the solution can vary significantly depending on the choice of the shape parameter indeed. In the literature, several solutions for the evaluation of an optimal value of c have been proposed depending upon the number of nodes, the distance between the nodes and the type of the RBFs. For instance, in [72] a shape parameter inversely proportional to the square root of the number of grid points was proposed in the case of multiquadrics RBFs. However, finding a good value of the parameter c is not always an easy task. As specified in [77], smaller values of c generally lead to higher accuracy. On the other hand, unstable numerical solutions may occur as the value of c is decreased (see [139]). In the present thesis, a constant value of c is used and no optimization procedures are employed. An optimization technique, such as the one recently introduced by Fantuzzi et al. [71], will be the subject of future work.

3.3.1 From a differential problem to a eigenvalue problem via RBFs

Let the domain of the problem be denoted by Γ and let $\partial\Gamma$ be its boundary. We consider n_I nodes in Γ and n_B nodes on $\partial\Gamma$, with $n = n_I + n_B$. In the particular case of 1D beam theories as in this work, $n_B = 2$ (i.e. the two ends of the beam). By substituting

Eqs. (3.40) and (3.41) into Eq. (3.38), the differential equations of motion are reduced to a classical eigenvalue problem. For a node $y_j \in \Gamma$, it reads:

$$(\mathbf{K}^{\tau sij} - \omega^2 \mathbf{M}^{\tau sij}) \alpha_{si} = 0 \quad (3.44)$$

where $\mathbf{K}^{\tau sij}$ and $\mathbf{M}^{\tau sij}$ are the 3×3 fundamental nuclei which contains the coefficients of the algebraic equations of motion. In the case of orthotropic material, the components of matrix $\mathbf{K}^{\tau sij}$ are

$$\begin{aligned} \mathbf{K}_{(11)}^{\tau sij} &= (E_{\tau, xs, x}^{22} + E_{\tau, zs, z}^{44}) \phi_{ij} + (E_{\tau, xs}^{26} - E_{\tau s, x}^{26}) \phi_{ij, y} - E_{\tau s}^{66} \phi_{ij, yy} \\ \mathbf{K}_{(12)}^{\tau sij} &= (E_{\tau, xs, x}^{26} + E_{\tau, zs, z}^{45}) \phi_{ij} + (E_{\tau, xs}^{23} - E_{\tau s, x}^{66}) \phi_{ij, y} - E_{\tau s}^{36} \phi_{ij, yy} \\ \mathbf{K}_{(13)}^{\tau sij} &= (E_{\tau, xs, z}^{12} + E_{\tau, zs, x}^{44}) \phi_{ij} + (E_{\tau, zs}^{45} - E_{\tau s, z}^{16}) \phi_{ij, y} \\ \mathbf{K}_{(21)}^{\tau sij} &= (E_{\tau, xs, x}^{26} + E_{\tau, zs, z}^{45}) \phi_{ij} + (E_{\tau, xs}^{66} - E_{\tau s, x}^{23}) \phi_{ij, y} - E_{\tau s}^{36} \phi_{ij, yy} \\ \mathbf{K}_{(22)}^{\tau sij} &= (E_{\tau, xs, x}^{66} + E_{\tau, zs, z}^{55}) \phi_{ij} + (E_{\tau, xs}^{36} - E_{\tau s, x}^{36}) \phi_{ij, y} - E_{\tau s}^{33} \phi_{ij, yy} \\ \mathbf{K}_{(23)}^{\tau sij} &= (E_{\tau, xs, z}^{16} + E_{\tau, zs, x}^{45}) \phi_{ij} + (E_{\tau, zs}^{55} - E_{\tau s, z}^{13}) \phi_{ij, y} \\ \mathbf{K}_{(31)}^{\tau sij} &= (E_{\tau, xs, z}^{44} + E_{\tau, zs, x}^{12}) \phi_{ij} + (E_{\tau, zs}^{16} - E_{\tau s, z}^{45}) \phi_{ij, y} \\ \mathbf{K}_{(32)}^{\tau sij} &= (E_{\tau, xs, z}^{45} + E_{\tau, zs, x}^{16}) \phi_{ij} + (E_{\tau, zs}^{13} - E_{\tau s, z}^{55}) \phi_{ij, y} \\ \mathbf{K}_{(33)}^{\tau sij} &= (E_{\tau, xs, x}^{44} + E_{\tau, zs, z}^{11}) \phi_{ij} + (E_{\tau, xs}^{45} - E_{\tau s, x}^{45}) \phi_{ij, y} - E_{\tau s}^{55} \phi_{ij, yy} \end{aligned} \quad (3.45)$$

The components of matrix $\mathbf{M}^{\tau sij}$ are

$$\begin{aligned} \mathbf{M}_{(11)}^{\tau sij} &= \mathbf{M}_{(22)}^{\tau sij} = \mathbf{M}_{(33)}^{\tau sij} = E_{\tau s}^{\rho} \phi_{ij} \\ \mathbf{M}_{(12)}^{\tau sij} &= \mathbf{M}_{(13)}^{\tau sij} = \mathbf{M}_{(21)}^{\tau sij} = \mathbf{M}_{(23)}^{\tau sij} = \mathbf{M}_{(31)}^{\tau sij} = \mathbf{M}_{(32)}^{\tau sij} = 0 \end{aligned} \quad (3.46)$$

In Eqs. (3.45) and (3.46), ϕ_{ij} stands for $\phi_i(|y_j - y_i|)$. For a given theory order N , the eigenvalue problem describing the motion of the beam in free vibration is obtained by expanding $\mathbf{K}^{\tau sij}$ and $\mathbf{M}^{\tau sij}$ for $\tau = 1, 2, \dots, M$, $s = 1, 2, \dots, M$, $i = 1, \dots, n$, and $j = 1, \dots, n_I$. The final problem essentially holds

$$(\mathbf{K}^I - \omega^2 \mathbf{M}^I) \alpha = 0 \quad (3.47)$$

where the superscript I denotes the fact that Eq. (3.47) applies in Γ . In a similar way, the natural boundary conditions can be written in algebraic form by substituting Eqs. (3.40) and (3.41) into Eq. (3.39). For a node $y_j \in \partial\Gamma$, it reads:

$$\bar{\mathbf{P}}_{sj} = \mathbf{B}^{\tau sij} \alpha_{si} \quad (3.48)$$

where the components of the algebraic fundamental nucleus $\mathbf{B}^{\tau sij}$ are as follows:

$$\begin{aligned}
 \mathbf{B}_{(11)}^{\tau sij} &= E_{\tau s, x}^{26} \phi_{ij} + E_{\tau s}^{66} \phi_{ij, y}, & \mathbf{B}_{(12)}^{\tau sij} &= E_{\tau s, x}^{66} \phi_{ij} + E_{\tau s, x}^{66} \phi_{ij, y}, & \mathbf{B}_{(13)}^{\tau sij} &= E_{\tau s, z}^{16} \phi_{ij} \\
 \mathbf{B}_{(21)}^{\tau sij} &= E_{\tau s, x}^{23} \phi_{ij} + E_{\tau s}^{36} \phi_{ij, y}, & \mathbf{B}_{(22)}^{\tau sij} &= E_{\tau s, x}^{36} \phi_{ij} + E_{\tau s}^{33} \phi_{ij, y}, & \mathbf{B}_{(23)}^{\tau sij} &= E_{\tau s, z}^{13} \phi_{ij} \\
 \mathbf{B}_{(31)}^{\tau sij} &= E_{\tau s, z}^{45} \phi_{ij}, & \mathbf{B}_{(32)}^{\tau sij} &= E_{\tau s, z}^{55} \phi_{ij}, & \mathbf{B}_{(33)}^{\tau sij} &= E_{\tau s, x}^{45} \phi_{ij} + E_{\tau s}^{55} \phi_{ij, y}
 \end{aligned} \tag{3.49}$$

For a given expansion order N , the natural boundary conditions can be obtained in the form of Eq. (3.50) by expanding $\mathbf{B}^{\tau sij}$ for $\tau = 1, 2, \dots, M$, $s = 1, 2, \dots, M$, $i = 1, \dots, n$, and $j = n_I + 1, \dots, n$. In the case of homogeneous natural boundary condition one has

$$\mathbf{B}^B \boldsymbol{\alpha} = 0 \tag{3.50}$$

where superscript B denotes the fact that Eq. (3.50) applies on $\partial\Gamma$. Matrix \mathbf{B}^B is not derived in this thesis in the case of essential boundary conditions for the sake of brevity. Essential boundary conditions can be applied by imposing a certain value to the amplitude of the harmonically varying generalized displacement $\mathbf{U}_s(\mathbf{y}) = \bar{\mathbf{U}}_s(\mathbf{y})$.

Once matrices \mathbf{K}^I , \mathbf{M}^I , and \mathbf{B}^B are obtained, the final eigenvalue problem can be solved

$$\left(\begin{bmatrix} \mathbf{K}^I \\ \mathbf{B}^B \end{bmatrix} - \omega_k^2 \begin{bmatrix} \mathbf{M}^I \\ \mathbf{0} \end{bmatrix} \right) \boldsymbol{\alpha}_k = 0 \tag{3.51}$$

where $\boldsymbol{\alpha}_k$ is the k -th eigenvector. It is well known that some RBFs produces ill-conditioned matrices and this problem increases as the number of grid points rises. Some authors reduce the conditioning number by using preconditioners, see [100]. Moreover, the results discussed later in this thesis shows that, increasing the expansion order N , the problem can be severely ill-conditioned. However, scaling the matrices \mathbf{K}^I and \mathbf{M}^I as well as the matrix of natural (not essential) boundary conditions \mathbf{B}^B by the maximum coefficient of the stiffness matrix itself, was sufficient to obtain a well-conditioned problem for each case considered. Nevertheless, in order to further improve the accuracy of the solution, the generalized displacements on the boundary centers could be condensed with respect to those on the internal nodes, as presented in [158].

Chapter 4

Finite Element Method

The finite element method has acquired a predominant role in the analysis of structures. The historical reason is due to the limitations of analytical solutions, which are often available only for a few particular cases that represent coarse simplifications of reality. Although the exact solution of the free vibration problem of CUF models has been addressed in the present research by dynamic stiffness method for arbitrary boundary conditions and geometries, the finite element method still deserves particular attention for the ease it allows to face the various problems of mechanics as well as for its numerical stability and efficiency. In this chapter, the weak form of the 1D CUF governing equations for static and dynamic problems are thus formulated in terms of finite element approximation. The fundamental nuclei of the elemental stiffness, mass, and loading arrays are provided as well.

4.1 Weak form governing equations

In the previous chapter, the strong form ODEs related to CUF models have been solved both exactly - by using the DSM - and by reducing them into algebraic equations via RBFs. The weak form of the same mathematical problem is discussed hereinafter and presented as a weighted integral equation relaxing the strong form into a domain-averaging statement, thus holding solution only with respect to certain *test functions*. Weak form governing equations of CUF models are here obtained by means of the principle of virtual displacement and solved via Finite Element Method (FEM).

In the framework of FEM, the CUF generalized displacements $\mathbf{u}_\tau(y)$ (see Eq. (2.12)) are expressed as a weighted linear combination of arbitrary test functions (or *shape functions*); i.e.

$$\mathbf{u}_\tau(y) = N_i(y)\mathbf{q}_{\tau i}, \quad i = 1, 2, \dots, p + 1 \quad (4.1)$$

where N_i stands for 1D shape functions and $\mathbf{q}_{\tau i}$ is the nodal displacement vector,

$$\mathbf{q}_{\tau i} = \left\{ q_{u_{x\tau i}} \quad q_{u_{y\tau i}} \quad q_{u_{z\tau i}} \right\}^T \quad (4.2)$$

Similarly to τ index (see Section 2.2.1), i represents a summation over the $p + 1$ nodes of the 1D FEM element of order p . Thus, summarizing, the kinematic approximation by 1D CUF in the framework of FEM holds

$$\mathbf{u}(x, y, z) = F_\tau(x, z)N_i(y)\mathbf{q}_{\tau i}, \quad \tau = 1, 2, \dots, M \quad i = 1, 2, \dots, p + 1 \quad (4.3)$$

In this thesis, mostly Lagrange shape functions are used for the mechanical problem. Two-node linear ($p = 1$), three-node quadratic ($p = 2$), and four-node cubic ($p = 3$)

shape functions are considered. Lagrange 1D shape functions can be found in many reference books, for instance in [12]. However, they are also reported herein for the sake of completeness. In the case of B2 element, the shape functions are:

$$N_1 = \frac{1}{2}(1-r), \quad N_2 = \frac{1}{2}(1+r), \quad \begin{cases} r_1 = -1 \\ r_2 = +1 \end{cases} \quad (4.4)$$

where the natural coordinate, r , varies from -1 to $+1$ and r_i indicates the position of the node within the natural beam boundaries. In the case of B3 elements one has

$$N_1 = \frac{1}{2}r(r-1), \quad N_2 = \frac{1}{2}r(r+1), \quad N_3 = -(1+r)(1-r), \quad \begin{cases} r_1 = -1 \\ r_2 = +1 \\ r_3 = 0 \end{cases} \quad (4.5)$$

Finally, B4 shape functions hold

$$\begin{aligned} N_1 &= -\frac{9}{16}(r + \frac{1}{3})(r - \frac{1}{3})(r - 1), & N_2 &= \frac{9}{16}(r + \frac{1}{3})(r - \frac{1}{3})(r + 1), \\ N_3 &= +\frac{27}{16}(r + 1)(r - \frac{1}{3})(r - 1), & N_4 &= -\frac{27}{16}(r + 1)(r + \frac{1}{3})(r - 1), \end{aligned} \quad \begin{cases} r_1 = -1 \\ r_2 = +1 \\ r_3 = -\frac{1}{3} \\ r_4 = +\frac{1}{3} \end{cases} \quad (4.6)$$

4.1.1 Static response analysis

One of the main advantages of FEM is that it allows the handling of various problems of mechanics in a relatively straightforward and easy manner. In this thesis, FEM has been used for static, free vibration and dynamic response analyses of structures.

In the case of static analysis, the principle of virtual displacements holds

$$\delta L_{\text{int}} = \delta L_{\text{ext}} \quad (4.7)$$

where L_{int} stands for the strain energy as discussed in Chapter 3 and L_{ext} in the work done by the external loadings. In the case of FEM, the virtual variation of the internal work reads

$$\delta L_{\text{int}} = \delta \mathbf{q}^T \mathbf{K} \mathbf{q} \quad (4.8)$$

where \mathbf{q} is the global vector containing the generalized nodal unknowns and \mathbf{K} is the assembled global stiffness matrix whose derivation in the framework of CUF is briefly described in Section 4.2. On the other hand, the virtual variation of the external energy is

$$\delta L_{\text{ext}} = \delta \mathbf{q}^T \mathbf{P} \quad (4.9)$$

where \mathbf{P} is the vector of the generalized nodal forces (see Section 4.4). By substituting Eqs. (4.9) and (4.8) into Eq. (4.7), the final algebraic system of equations is obtained

$$\mathbf{K} \mathbf{q} = \mathbf{P} \quad (4.10)$$

4.1.2 Free vibrations

Free vibration analysis investigates the equilibrium between elastic and inertial forces. As already discussed in Chapter 3, the principle of virtual displacements in this case is formulated as

$$\delta L_{\text{int}} = -\delta L_{\text{ine}} \quad (4.11)$$

Introducing the FEM approximation, the virtual variation of inertial forces is written in the following form:

$$\delta L_{\text{ine}} = \delta \mathbf{q}^T \mathbf{M} \ddot{\mathbf{q}} \quad (4.12)$$

where \mathbf{M} is the global mass matrix as presented in Section 4.3 and $\ddot{\mathbf{q}}$ is the vector containing the nodal generalized accelerations. By substituting Eqs. (4.9) and (4.12) into Eq. (4.11), the equations of motion become

$$\mathbf{K} \mathbf{q} + \mathbf{M} \ddot{\mathbf{q}} = 0 \quad (4.13)$$

Considering the solution \mathbf{q} to be harmonic with amplitude \mathbf{Q} and angular frequency ω , Eq. (4.13) can be reduced into a classical eigenvalue problem as in the case of RBFs method (see Section 3.3)

$$(\mathbf{K} - \omega^2 \mathbf{M}) \mathbf{Q} e^{i\omega t} = 0 \quad (4.14)$$

4.1.3 Dynamic response

In the more general case, both internal, external and inertial energy contributions are accounted for. In this case, the principle of virtual displacements reads

$$\delta L_{\text{int}} = \delta L_{\text{ext}} - \delta L_{\text{ine}} \quad (4.15)$$

which in the FEM form becomes

$$\mathbf{K} \mathbf{q} + \mathbf{M} \ddot{\mathbf{q}} = \mathbf{P} \quad (4.16)$$

The solution of this equation in the time domain requires the use of a numerical technique. More details about dynamic response problems are given in Chapter 7, where the mode superposition method as a means to solve Eq. (4.16) is discussed in details and the effect of structural damping is also addressed.

4.2 Stiffness matrix

The virtual variation of the strain energy is recalled here for the sake of clarity

$$\delta L_{\text{int}} = \int_V \delta \boldsymbol{\epsilon}^T \boldsymbol{\sigma} dV \quad (4.17)$$

The fundamental nucleus of the elemental structural stiffness matrix of the 1D CUF FE model is derived by substituting the constitutive laws (Eq. (2.5)), the geometrical relations (Eq. (2.3)), and the kinematic assumptions of Eq. (4.3) into Eq. (4.17). One has

$$\delta L_{\text{int}} = \delta \mathbf{q}_{\tau i}^T \mathbf{K}^{\tau s i j} \mathbf{q}_{s j} \quad (4.18)$$

The derivation of the FE stiffness matrix and the other arrays is not reported here, but they can be found in [33, 27], where more details about CUF and FEM are also given. However, the components of the 3×3 fundamental nucleus of the stiffness matrix are given below and they are referred to as $K_{(rc)}^{\tau s i j}$, where r is the row number ($r = 1, 2, 3$) and c is

the column number ($c = 1, 2, 3$).

$$\begin{aligned}
 K_{(11)}^{\tau sij} &= (E_{\tau, xs, x}^{22} + E_{\tau, zs, z}^{44}) J_{ij} + E_{\tau, xs}^{26} J_{ij, y} + E_{\tau s, x}^{26} J_{i, yj} + E_{\tau s}^{66} J_{i, yj, y} \\
 K_{(12)}^{\tau sij} &= (E_{\tau, xs, x}^{26} + E_{\tau, zs, z}^{45}) J_{ij} + E_{\tau, xs}^{23} J_{ij, y} + E_{\tau s, x}^{66} J_{i, yj} + E_{\tau s}^{36} J_{i, yj, y} \\
 K_{(13)}^{\tau sij} &= (E_{\tau, xs, z}^{12} + E_{\tau, zs, x}^{44}) J_{ij} + E_{\tau, zs}^{45} J_{ij, y} + E_{\tau s, z}^{16} J_{i, yj} \\
 K_{(21)}^{\tau sij} &= (E_{\tau, xs, x}^{26} + E_{\tau, zs, z}^{45}) J_{ij} + E_{\tau, xs}^{66} J_{ij, y} + E_{\tau s, x}^{23} J_{i, yj} + E_{\tau s}^{36} J_{i, yj, y} \\
 K_{(22)}^{\tau sij} &= (E_{\tau, xs, x}^{66} + E_{\tau, zs, z}^{55}) J_{ij} + E_{\tau, xs}^{36} J_{ij, y} + E_{\tau s, x}^{36} J_{i, yj} + E_{\tau s}^{33} J_{i, yj, y} \\
 K_{(23)}^{\tau sij} &= (E_{\tau, xs, z}^{16} + E_{\tau, zs, x}^{45}) J_{ij} + E_{\tau, zs}^{55} J_{ij, y} + E_{\tau s, z}^{13} J_{i, yj} \\
 K_{(31)}^{\tau sij} &= (E_{\tau, xs, z}^{44} + E_{\tau, zs, x}^{12}) J_{ij} + E_{\tau, zs}^{16} J_{ij, y} + E_{\tau s, z}^{45} J_{i, yj} \\
 K_{(32)}^{\tau sij} &= (E_{\tau, xs, z}^{45} + E_{\tau, zs, x}^{16}) J_{ij} + E_{\tau, zs}^{13} J_{ij, y} + E_{\tau s, z}^{55} J_{i, yj} \\
 K_{(33)}^{\tau sij} &= (E_{\tau, xs, x}^{44} + E_{\tau, zs, z}^{11}) J_{ij} + E_{\tau, xs}^{45} J_{ij, y} + E_{\tau s, x}^{45} J_{i, ij} + E_{\tau s}^{55} J_{i, yj, y}
 \end{aligned} \tag{4.19}$$

where the generic term $E_{\tau, \theta s, \zeta}^{\alpha\beta}$ is a cross-sectional parameter as defined in Eq. (3.4), whereas

$$\begin{aligned}
 J_{ij} &= \int_L N_i(y) N_j(y) dy, & J_{i, yj} &= \int_L N_{i, y}(y) N_j(y) dy \\
 J_{ij, y} &= \int_L N_i(y) N_{j, y}(y) dy, & J_{i, yj, y} &= \int_L N_{i, y}(y) N_{j, y}(y) dy
 \end{aligned} \tag{4.20}$$

are the integrals of the product of shapes functions and related derivatives along the beam axis. The shape functions integrals are calculated by means Gauss integration [152]. In particular, selective reduced integration scheme is adopted in order to attenuate the shear locking phenomena (see [12, 160]).

The fundamental nuclei in FEM have the same properties of the strong form counterparts; hence, they neither depend on the expansion order or the choice of the F_τ expansion polynomials. Thus, with only nine coding statements, it is possible to implement any-order of multiple class theories. In fact, the assembly procedure of the global stiffness matrix is straightforwardly accomplished by using the four indexes τ , s , i , and j , which are opportunely translated into loop cycles in the coding statements. The automatic derivation of the elemental stiffness matrix is depicted in Fig. 4.1, whereas Fig. 4.2 shows the classical FEM assembly of the global arrays from the element matrices. Once the global matrix is obtained, boundary conditions are applied by the penalty method in the present work.

4.3 Mass matrix

As discussed in Section 3.1, the virtual variation of the inertial work is given by

$$\delta L_{\text{ine}} = \int_V \delta \mathbf{u}^T \rho \ddot{\mathbf{u}}_s dV \tag{4.21}$$

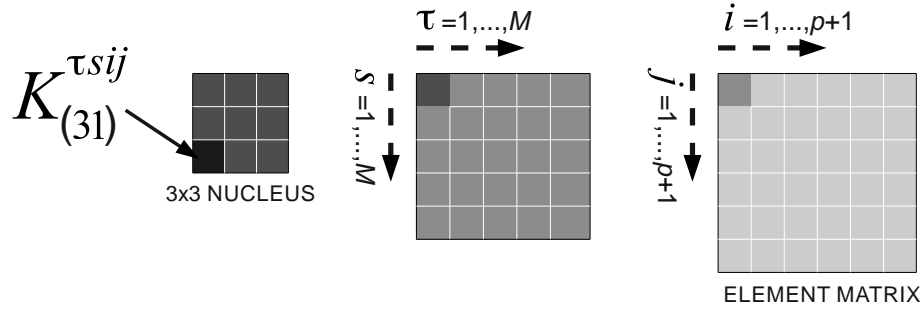


Figure 4.1: Derivation of the element stiffness matrix from the fundamental nucleus

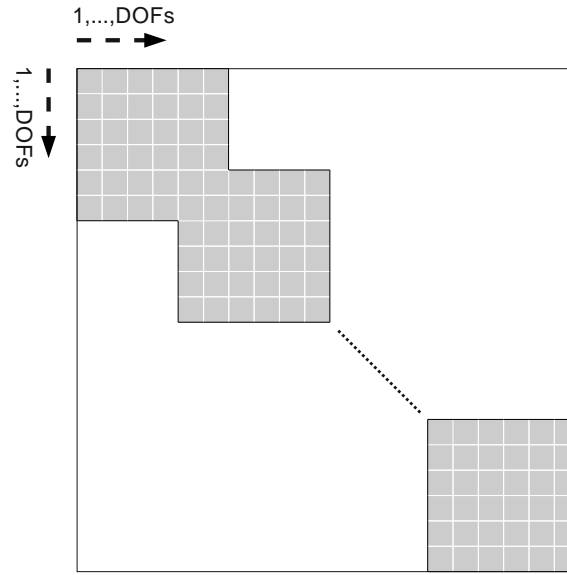


Figure 4.2: Classical FEM assembly procedure of element matrices

Retrieving the 1D CUF FE approximation of the displacement field (Eq. (4.3)), it is easy to demonstrate that

$$\delta L_{\text{ine}} = \delta \mathbf{q}_{\tau i}^T \left(\int_L N_i N_j dy \int_{\Omega} \rho F_{\tau} F_s d\Omega \right) \ddot{\mathbf{q}}_{s j} = \delta \mathbf{q}_{\tau i}^T (E_{\tau s}^{\rho} J_{ij} \mathbf{I}) \ddot{\mathbf{q}}_{s j} \quad (4.22)$$

where \mathbf{I} is a 3×3 identity matrix and $E_{\tau s}^{\rho}$ has been defined in Eq. (3.8). The terms into brackets in Eq. (4.22) represent the fundamental nucleus of the FE mass matrix $\mathbf{M}^{\tau s i j}$, which is clearly diagonal.

$$\mathbf{M}^{\tau s i j} = E_{\tau s}^{\rho} J_{ij} \mathbf{I} \quad (4.23)$$

The derivation of the global mass matrix is completely analogous to the stiffness assembly discussed in the previous section.

4.3.1 Localized inertia

In the present thesis, the effect due to non-structural masses is also investigated (see [124]). Localized inertia can in principle be arbitrarily placed into the 3D domain of the beam structure. In the framework of CUF, this is easily realized by adding the following term to the fundamental nucleus of the mass matrix:

$$\mathbf{m}^{\tau s i j} = \mathbf{I} (F_{\tau}(x_m, z_m) F_s(x_m, z_m) N_i(y_m) N_j(y_m)) \tilde{m} \quad (4.24)$$

where \tilde{m} is the value of the non-structural mass, which is applied at point (x_m, y_m, z_m) .

4.4 Loading vector

The loadings vector that is variationally coherent to the hierarchical model can be derived with relative ease in the case of a generic concentrated load \mathbf{F} acting on the application point (x_p, y_p, z_p) ,

$$\mathbf{F} = \{ F_x \quad F_y \quad F_z \}^T \quad (4.25)$$

Any other loading conditions, such as line and surface loads, can be similarly treated. The virtual work due to \mathbf{F} is

$$\delta L_{\text{ext}} = \delta \mathbf{u}^T \mathbf{F} \quad (4.26)$$

After using Eq. (4.3), Eq. (4.26) becomes

$$\delta L_{\text{ext}} = \delta \mathbf{q}_{\tau i}^T F_{\tau} N_i \mathbf{F} = \delta \mathbf{q}_{\tau i}^T \mathbf{P}^{\tau i} \quad (4.27)$$

where F_{τ} and N_i are evaluated in (x_p, z_p) and y_p , respectively. The last equation allows the identification of the components of the nucleus that have to be loaded; i.e., it allows the proper assembling of the loading vector by detecting the displacement variables that have to be loaded.

4.4.1 Inertial loads

In this thesis, the special case of inertial loads (see [124, 45, 46]) has been considered; e.g., for gust response analysis in Chapter 7. When using classical beam theories, translational as well as rotational acceleration are usually applied with respect to the reference axis - or with respect to the shear axis if transverse stresses are also included. The derivation of the FEM loading vector due to generic accelerations in the framework of CUF models, which are opportunely able to take into account the effects due to 3D distributions of inertial loads, is described hereinafter. Let the following acceleration field be applied to the structure:

$$\ddot{\mathbf{u}}_0(x, y, z) = \{ \ddot{u}_{x_0} \quad \ddot{u}_{y_0} \quad \ddot{u}_{z_0} \}^T \quad (4.28)$$

The virtual variation of the external work, δL_{ext} , due to the acceleration field $\ddot{\mathbf{u}}_0$ is given by:

$$\delta L_{\text{ext}} = \int_V \delta \mathbf{u}^T \rho \ddot{\mathbf{u}}_0 \, dV \quad (4.29)$$

Equation (4.3) is substituted into Eq. (4.29). It reads:

$$\delta L_{\text{ext}} = \delta \mathbf{q}_{\tau i}^T \left(\int_L N_i N_j \, dy \int_{\Omega} \rho F_{\tau} F_s \, d\Omega \right) \ddot{\mathbf{q}}_{s j_0} \quad (4.30)$$

where the term between square brackets is the fundamental nucleus of the mass matrix $\mathbf{M}^{\tau s i j}$. The virtual variation of the external work is therefore written as

$$\delta L_{\text{ext}} = \delta \mathbf{q}_{\tau i}^T \mathbf{M}^{\tau s i j} \ddot{\mathbf{q}}_{s j_0} = \delta \mathbf{q}_{\tau i}^T \mathbf{P}_{\text{ine}}^{\tau i} \quad (4.31)$$

where $\mathbf{P}_{\text{ine}}^{\tau i}$ is the nucleus of the loading vector due to the given acceleration field.

Chapter 5

Component-wise

The analysis of multi-component structures, such as aircraft frames, generally requires the adoption and the coupling of various mathematical models, even in the framework of finite element method. As a consequence, artificial techniques are usually involved to connect, for example, 1D and 2D finite elements. This may result in numerical and physical uncertainties, especially if higher-order models are employed. In this chapter, two innovative approaches are presented. The component-wise approach, which is based on LE, exploits the natural capability of Lagrange polynomials to be assembled on the beam cross-section. Multi-line approach, on the other hand, is based on 1D TE finite elements, which are placed on different beam axes and connected together at boundaries via Lagrange multipliers method.

5.1 Multi-component structures

Most of the engineering structures are composed of different components, which are commonly characterized by different scales and geometries in order to accomplish the technical requisites. In the structural analysis and design of wings, for example, each component (i.e. ribs, stringers, panels, etc.) is commonly modelled through different elements (beams, shells, or solids). For instance, by considering a simplified wing-box (see Fig. 5.1), stringers are usually considered as beams, whereas panels and ribs are modelled with 2D plate elements in modern analysis techniques. If necessary, 3D elasticity elements could be also

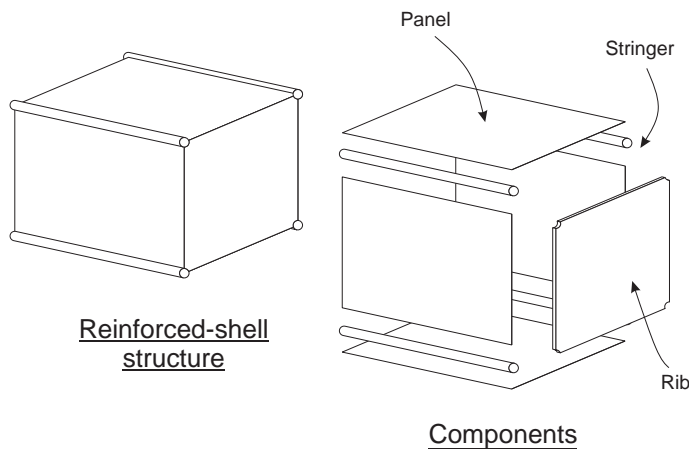


Figure 5.1: Multi-component structure

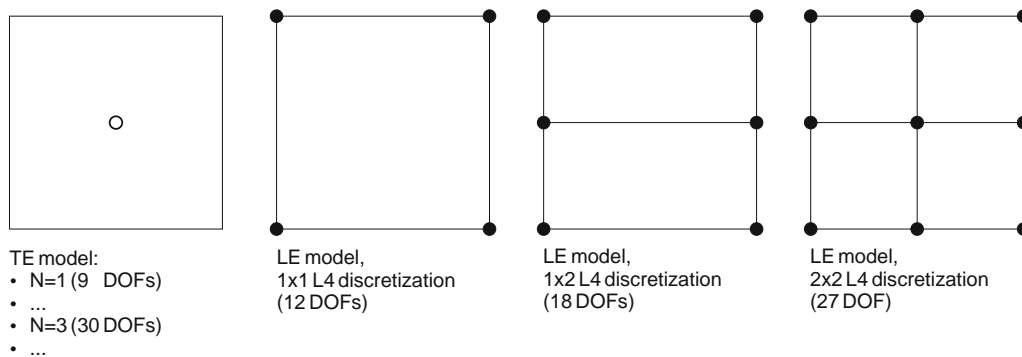


Figure 5.2: Differences between the TE and LE models

used for stringers or both stringers and panels. The choice of the models to involve in the mathematical formulation of the whole structure is part of the knowledge and expertise of the structural analysts.

Other examples of multi-component structures are composites, which are composed of laminae, fibres, core, and matrix; civil engineering structures, which are made of columns, floors, walls, etc.; and naval engineering structures, which are very similar to aerospace ones.

5.2 Component-Wise (CW) approach

The refined TE models described in Chapter 2 are characterised by degrees of freedom (displacements and N-order derivatives of displacements) with a correspondence to the axis of the beam (see Fig. 5.2). As already mentioned, the CUF expansion can also be made by using only pure displacement values, e.g. by using Lagrange polynomials. The resulting LE can be used for the whole cross-section or can be introduced by dividing the cross-section into various sub-domains (see Fig. 5.2). The resulting approach is referred to as Component-Wise (CW) because Lagrange elements are used to model the displacement variables in each structural component at the cross-sectional level. This characteristic allows us to separately model, for instance, stringers and panels in aerospace structures design. In the present work, CW has been developed in the framework of FEM (see Chapter 4) and it is briefly discussed below.

The CW approach when applied to the two-stringer spar of Fig. 5.3a is discussed as an example. Figure 5.3b shows a possible CW model of the spar where each component is modelled via one 1D LE element. Each LE element is then assembled above the cross-section to obtain the global stiffness matrix based on the 1D formulation. Since panels could not be reasonably modelled via a 1D formulation, 1D CW models can be refined by using several L-elements for one component. This aspect is shown in Fig. 5.3c, where the panel is modelled via two 1D LE elements. In the case of the wing structures, as considered in this thesis, LE expansions are adopted for each wing section component (spars, stringer, panels), including ribs. This methodology allows us to tune the capabilities of the model by (1) choosing which component requires a more detailed model; (2) setting the order of the structural model to be used.

One of the primary advantages of the CW approach is that the FE mathematical models can be built by using only real boundaries; artificial lines (beam axes) and surfaces (plate/shell reference surfaces) are no longer used. Up to now, this result could only be obtained using solid finite elements. Moreover, thanks to the CW approach, each

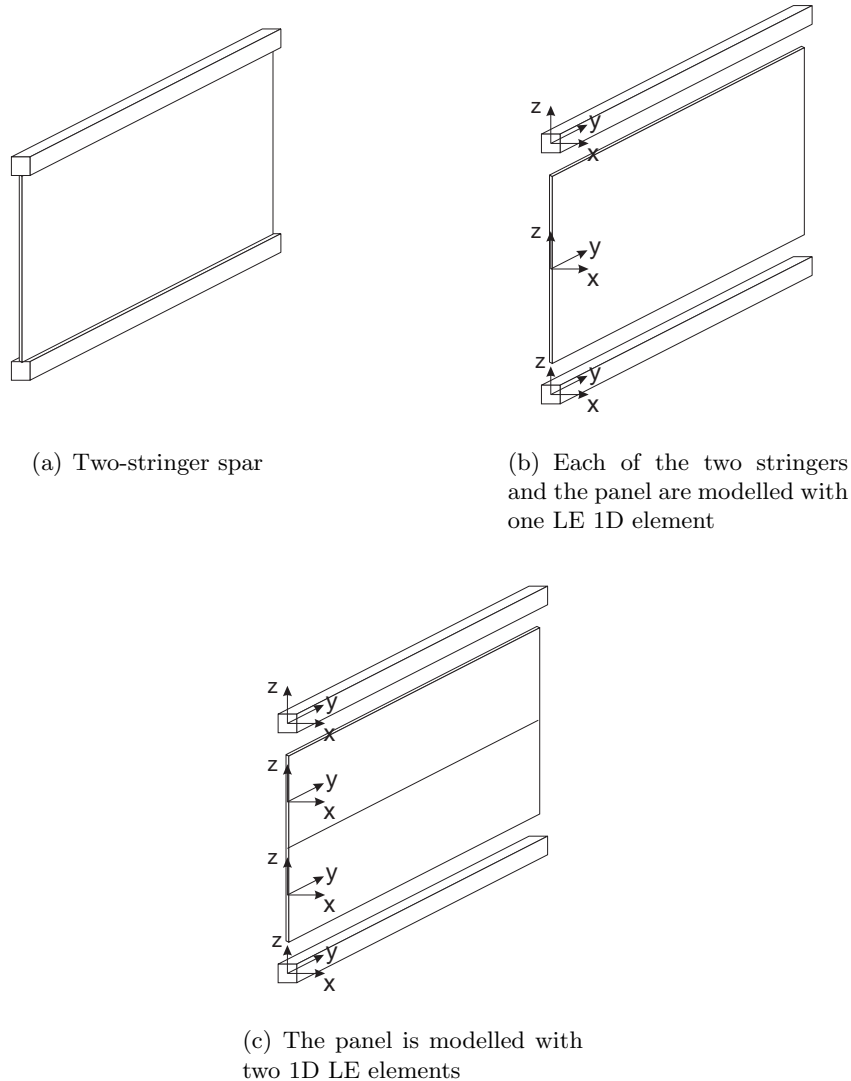


Figure 5.3: Component-wise approach through LE elements

component of the structure is described by means of the same 1D model (i.e. the same FE arrays) and artifices to coupled model with different closures (e.g. beams and shell elements) are avoided.

5.3 Multi-Line (ML)

Considerable efforts have been made during the research activities in order to allow TE models to efficiently address multi-component structures. In fact, since the generalised unknowns are placed on the beam axis in the case of TE CUF models, the solution by high expansion orders N may become increasingly inaccurate as the distance from the reference axis of the beam increases when complex cross-sections are considered. Moreover, it may be desirable to tune the model order for each structural component.

To address these challenges, Multi-Line (ML) beam models have been introduced. In the ML beam modelling approach, a slender body is discretized by means of multiple

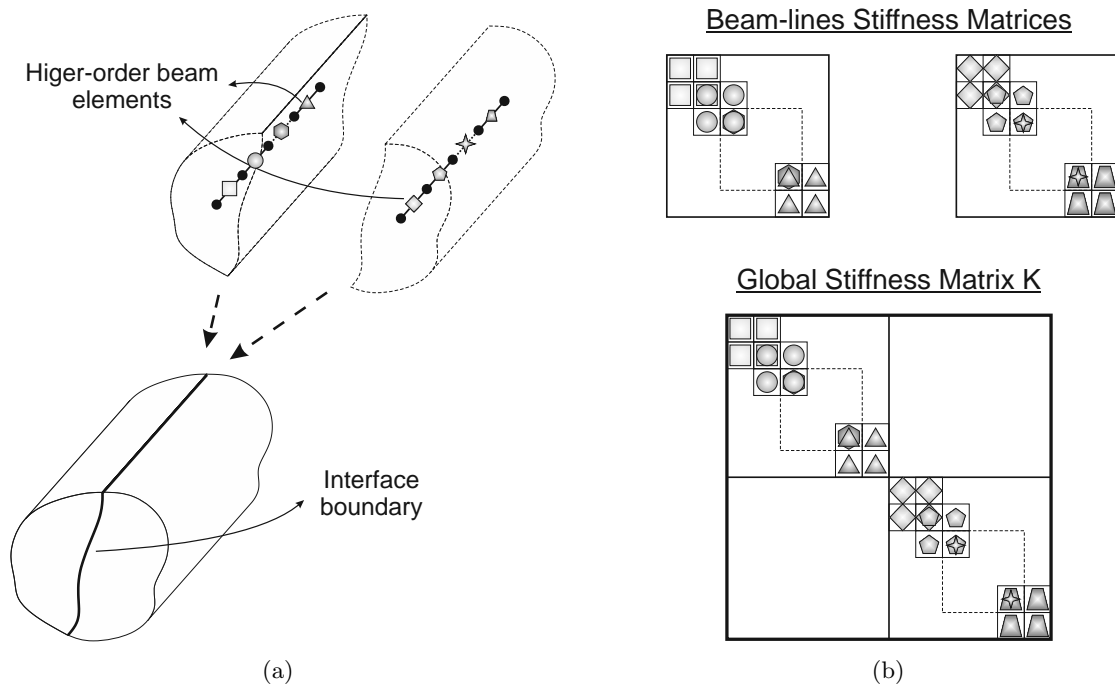


Figure 5.4: Multi-line approach for the analysis of slender bodies (a) and assembly of the global stiffness matrix (b)

beam axes that are placed in different regions over the problem domain. Different-order refined beam elements can be adopted for each beam-line in ML models. Then, once each beam axis has been discretized with 1D elements, Lagrange multipliers are used to impose constraints on displacement variables at a number of *connecting points* at the interface boundaries between each beam-line. The number of beam-lines and the order of the beam elements used to discretize each beam-line, as well as the number and the location of *connecting points* at the boundary interfaces, are all parameters of the ML model.

5.3.1 Lagrange multipliers

The method of Lagrange multipliers provides the stationary conditions of a constrained functional. The application of Lagrange multipliers to CUF has recently been introduced in [42], where Lagrange multipliers are used to implement higher-order 1D models with variable kinematic field along the beam axis. A more generic discussion of the Lagrange multipliers method can be found in [58, 149], whereas Zienkiewicz and Taylor [179] show the use of multipliers in FEM for contact and tied interfaces, for multibody coupling and to avoid the necessity of C^1 continuity for the problem of thin plates.

In the present thesis, Lagrange multipliers are used to implement ML models. In Fig. 5.4a a slender structure discretized by two different beam axes is shown. Higher-order elements of arbitrary order are placed on each beam-line, which separately describes a given sub-region of the whole structure. Lagrange multipliers are then used to impose compatibility on displacement variables at a number of *connecting points* at the interface boundary between beam-lines.

If we consider two points, 1 and 2, sharing the same position on the interface boundary, the *Lagrangian* that has to be added to the original problem in order to impose the equality

of displacements is

$$\Pi = \boldsymbol{\lambda}^T (\mathbf{u}^1 - \mathbf{u}^2) \quad (5.1)$$

where \mathbf{u}^1 and \mathbf{u}^2 are the displacements of points 1 and 2, respectively. Points 1 and 2 belong to different beam-lines. $\boldsymbol{\lambda}$ is the vector containing the Lagrange multipliers. Equation (5.1) is rewritten in terms of CUF with the help of Eq. (4.3).

$$\Pi = \boldsymbol{\lambda}^T \mathbf{B} \mathbf{q} \quad (5.2)$$

where the fundamental nucleus of the matrix \mathbf{B} is

$$\mathbf{B}^{\tau i} = \left(F_{\tau}^1 N_i^1 - F_{\tau}^2 N_i^2 \right) \mathbf{I} \quad (5.3)$$

\mathbf{I} is the identity matrix with dimensions 3×3 . $F_{\tau}^1 N_i^1$ and $F_{\tau}^2 N_i^2$ are the products of the cross-sectional functions of Eq. (2.12) and the shape functions along the beam axis computed at points 1 and 2, respectively. The superscripts "1" and "2" also denote the fact that, generally, different beam axes can be modeled with different beam theories and discretized with different FE meshes. More details about the use of multipliers in refined beam theories can be found in [42].

The solution of the problem is given by finding \mathbf{q} and $\boldsymbol{\lambda}$ from the following linear system:

$$\begin{cases} \mathbf{K} \mathbf{q} + \frac{\partial \Pi}{\partial \mathbf{q}} = \mathbf{P} \\ \frac{\partial \Pi}{\partial \boldsymbol{\lambda}} = \bar{\mathbf{u}} \end{cases} \quad (5.4)$$

where \mathbf{P} is the loadings vector and $\bar{\mathbf{u}}$ is equal to 0 for homogeneous conditions. \mathbf{K} is the global stiffness matrix. \mathbf{K} is built by assembling the stiffness matrices of each beam-line - which are computed according to the previous chapter - as shown in Fig. 5.4b. Equation (5.4) is rewritten using Eq. (5.2). In a matrix form it reads

$$\begin{bmatrix} \mathbf{K} & \mathbf{B}^T \\ \mathbf{B} & 0 \end{bmatrix} \begin{bmatrix} \mathbf{q} \\ \boldsymbol{\lambda} \end{bmatrix} = \begin{bmatrix} \mathbf{F} \\ 0 \end{bmatrix} \quad (5.5)$$

The use of the multipliers method offers many advantages. However, the main disadvantage of its use in structural problems is that the matrix of Eq. (5.5) is not, in general, positive definite.

5.3.2 ML models for the analysis of composites

ML models have demonstrated enhanced capabilities also in the analysis of composite structures [37]. In a ML framework, in fact, each layer of the composite laminate is modelled by one or more TE beam lines, each having its own properties and kinematic. The resulting methodology mimics layer-wise models, both in terms of idea and accuracy.

Chapter 6

Aeroelastic Model

Aeroelasticity plays a critical role in the design of modern aerospace vehicles. Among others, flutter is a catastrophic aeroelastic phenomenon that must be avoided at all costs. In this chapter, an unsteady aerodynamic model based on the vortex and doublet lattice methods is briefly described. The aeroelastic stability problem is therefore formulated and solved with particular reference to the g -method. The attention is focused on the capability of the presented methodology to be applied to both FE and strong formulations of 1D refined CUF models.

6.1 Hypotheses

A continuation of the work initiated in [126] - where CUF FE models were coupled with an unsteady aerodynamic formulation based on panel methods for flutter analyses - has been carried out during the research activities described in this thesis. In particular, the DSM CUF formulation (see Chapter 3) has been coupled with the aeroelastic model in the present work. Therefore, a brief description of the adopted aerodynamic and aeroelastic theories are described hereinafter for the sake of completeness.

According to [126, 128, 127, 123], the formulation described here is limited to planar lifting surfaces and subsonic incompressible flows. Moreover, the following hypotheses hold:

1. Lifting surfaces are modeled as infinitely thin sheets of discrete singularities (vortices and doublets).
2. Viscosity is neglected.
3. Boundary conditions (namely the non-penetration condition) are imposed on a number of control points placed on a mean surface.
4. A system of linear algebraic equations is solved to determine singularity strengths.
5. Thickness effect is ignored.

6.2 Oscillating lifting surfaces

The fundamental equation that, for a given oscillating surface, relates normalwash velocities to pressure jumps in different points of the surface is provided in the following. This equation is derived from the linear aerodynamic potential equation, whose comprehensive description can be found in [16].

A notation that uses non-dimensional quantities is adopted. If ω is the frequency, W is the normalwash perpendicular to an oscillating surface, and ΔP the pressure jump, the following relations can be written:

$$w = \frac{W}{V_\infty}; \quad \Delta p = \frac{\Delta P}{\frac{1}{2}\rho_\infty V_\infty^2} \quad (6.1)$$

Where V_∞ is the free-stream velocity and ρ_∞ is the air density. In the case of harmonic motion,

$$w = \bar{w} e^{i\omega t}; \quad \Delta p = \overline{\Delta p} e^{i\omega t} \quad (6.2)$$

Following [110] or [2], the normalwash in a point with coordinates x, y due to the pulsating pressure jump $\overline{\Delta p}$ in the point ξ, η has the following expression:

$$\bar{w} = \frac{1}{8\pi} \int_A \overline{\Delta p} K(x_0, y_0, \omega, M) dA \quad (6.3)$$

where M is the Mach number and

$$x_0 = x - \xi; \quad y_0 = y - \eta \quad (6.4)$$

The formal expression of the kernel function, $K(x_0, y_0, \omega, M)$, is not reported here for the sake of brevity; it can be found in [110]. Equation (6.3) can be numerically solved by means of the Doublet Lattice Method (DLM). However, as it will be clear later in this chapter, the steady part of the normalwash is calculated via the Vortex Lattice Method (VLM) (see [136]), which is briefly introduced in the next section.

6.2.1 Vortex Lattice Method (VLM)

In the framework of panel methods, such as VLM and DLM, a lifting surface is discretized into a number of panels. The key equation of the VLM is the following: named \mathbf{V}_j^i the velocity on the panel i (at the control point P_C^i) induced by the vortices of the sending panel j , the *influence coefficients* are defined as

$$a_{ij}^\Gamma = \mathbf{V}_j^i \cdot \mathbf{n}_i \quad (6.5)$$

where \mathbf{n}_i is the unit vector orthogonal to panel i .

The wall tangency condition has to be imposed for all panels of all surfaces. Considering the assumption that the freestream velocity, V_∞ , is direct along $+x$, for the panel i the wall tangency condition is

$$a_{i1}^\Gamma \Gamma_1 + a_{i2}^\Gamma \Gamma_2 + a_{i3}^\Gamma \Gamma_3 + \dots + a_{iN}^\Gamma \Gamma_N + V_\infty (\mathbf{i}^T \cdot \mathbf{n}_i) = 0 \quad (6.6)$$

where $\Gamma_1, \Gamma_2, \dots, \Gamma_N$ are the circulations of the sending panels, and \mathbf{i} is the unit vector parallel to the x axis. Assuming small perturbations, the following simplification holds:

$$\mathbf{i}^T \cdot \mathbf{n}_i = -\frac{dZ_{i \text{ loc}}}{dx} \quad (6.7)$$

where $Z_{i \text{ loc}}$ is the vertical displacement of the receiving panel i at the correspondent control point, which is located at the center of the panel's three-quarter chord line. It is easy to realize that $\frac{dZ_{i \text{ loc}}}{dx}$ is equal to the normalized normalwash at panel i , w_i . Hence, Eq. (6.6) can be formulated as

$$a_{i1}^\Gamma \Gamma_1 + a_{i2}^\Gamma \Gamma_2 + a_{i3}^\Gamma \Gamma_3 + \dots + a_{iN}^\Gamma \Gamma_N = V_\infty w_i \quad (6.8)$$

The un-dimensional pressure jump, Δp_j , at the j -th sending panel is retrieved into the formulation by recalling the following relation:

$$\Gamma_j = \frac{1}{2} V_\infty \Delta x_j \Delta p_j \quad (6.9)$$

where Δx_j is the length of the panel j in the streamwise direction. Therefore, the final form of the wall tangency condition at panel i reads

$$\frac{1}{2} \Delta x_1 a_{i1}^\Gamma \Delta p_1 + \frac{1}{2} \Delta x_2 a_{i2}^\Gamma \Delta p_2 + \frac{1}{2} \Delta x_3 a_{i3}^\Gamma \Delta p_3 + \dots + \frac{1}{2} \Delta x_N a_{iN}^\Gamma \Delta p_N = w_i \quad (6.10)$$

Equation (6.10) allows one to evaluate the steady contribution to the normalwash at panel i . For further details about VLM, the reader is referred to [103].

6.2.2 Quartic Doublet Lattice Method (DLM)

According to Rodden et al. [136], Eq. (6.3) is reduced into the following linear system of equations:

$$\bar{w}_i = \sum_{j=1}^{N_{AP}} D_{ij} \bar{\Delta p}_j \quad (6.11)$$

where D_{ij} are the *normalwash factors* and N_{AP} is the number of aerodynamic panels. D_{ij} is given by

$$D_{ij} = D_{0ij} + D_{1ij} \quad (6.12)$$

where D_{0ij} is the stationary part calculated by means of VLM. According to Eq. (6.10), D_{0ij} is expressed as

$$D_{0ij} = \frac{1}{2} \Delta x_j a_{ij}^\Gamma \quad (6.13)$$

On the other hand, by following Rodden et al. [136], D_{1ij} is

$$D_{1ij} = \frac{\Delta x_j}{8\pi} \int_{-e_j}^{+e_j} \frac{Q_1(\hat{\eta}_j)}{r^2} d\hat{\eta}_j \quad (6.14)$$

where $\hat{\eta}_j$ is the local spanwise coordinate in the plane of the sender panel j ; e_j is the semi-length of the j -th panel along the $\hat{\eta}_j$ direction; r is the cylindrical radius from the sending doublet; and $Q_1(\hat{\eta}_j)$ is the quartic approximation to kernel operator, i.e.

$$Q_1(\hat{\eta}_j) = A_1 \hat{\eta}_j^2 + B_1 \hat{\eta}_j + C_1 + D_1 \hat{\eta}_j^3 + E_1 \hat{\eta}_j^4 \approx \left(e^{-\frac{i\omega x_0}{V_\infty}} K_1 - K_{10} \right) T_1 \quad (6.15)$$

In order to calculate the coefficients A_1, B_1, \dots , the polynomial function is imposed to be equal to the approximated function on the right-hand side, where K_1 is a factor in the numerator of the kernel and K_{10} the correspondent steady contribution. It is therefore clear that this condition shall be imposed in five points for each sending panel j . The points are placed in the following positions: inboard, inboard intermediate, center, out-board intermediate and outboard. However, the five coefficients A_1, B_1, \dots , are not given here for the sake of brevity, but they can be found in [136, 126]. Nevertheless, the expression of

D_{1ij} is provided as follows:

$$\begin{aligned}
 D_{1ij} = & \frac{\Delta x_j}{8\pi} \left\{ [\hat{y}_i^2 A_1 + \hat{y}_i B_1 + C_1 + \hat{y}_i^3 D_1 + \hat{y}_i^4 E_1] F \right. \\
 & + \left[\hat{y}_i A_1 + \frac{1}{2} B_1 + \frac{3}{2} \hat{y}_i^2 D_1 + 2 \hat{y}_i^3 E_1 \right] \ln \frac{(\hat{y}_i - e_j)^2}{(\hat{y}_i + e_j)^2} \\
 & \left. + 2 e_j \left[A_1 + 2 \hat{y}_i D_1 + \left(3 \hat{y}_i^2 + \frac{1}{3} e_j^2 \right) E_1 \right] \right\}
 \end{aligned} \tag{6.16}$$

where \hat{y}_i is the coordinate of the receiving point relative to the midpoint of the sending panel, and F is the Hadamard's finite part (see [135]).

6.3 Unsteady aeroelastic analysis

Under the assumptions of linear potential aerodynamics, it is justified to consider only the displacement components perpendicular to the lifting surfaces. In this work, the reference surfaces are considered with null initial angle of attack and null dihedral angle. Moreover, according to [60], these surfaces are discretized by means of the following guidelines: (i) the local x axis of an aerodynamic lifting surface is always the global x -axis direction of the flow; (ii) each aerodynamic reference surface is divided into strips of panels; (iii) low-order modeling is used, in which each panel has a load point (it is the point at the center of the panel's quarter chord line) and a control point. The locations of these points are the same for both the vortex and the doublet lattice methods.

6.3.1 Modal shapes and boundary conditions

The unsteady aeroelastic analysis is carried out by considering a set of modal shapes as generalized motions for the unsteady aerodynamic generalized force generation. Each set of modal shapes, ϕ_m , can be considered as a displacement vector defined on a set of points above the structure. Slopes and displacements at control and load points of the aerodynamic panels are then given by

$$\frac{\partial \mathcal{Z}}{\partial x} = \mathbf{A} \cdot \phi_m \tag{6.17}$$

$$\tilde{\mathcal{Z}} = \tilde{\mathbf{A}}^* \cdot \phi_m \tag{6.18}$$

$$\mathcal{Z} = \mathbf{A}^* \cdot \phi_m \tag{6.19}$$

where $\tilde{\mathcal{Z}}$ and \mathcal{Z} are the displacements at load and control points, respectively. \mathbf{A} , $\tilde{\mathbf{A}}^*$, and \mathbf{A}^* are computed through the Infinite Plate Spline (IPS), see [88]. For the sake of brevity, the explicit expressions of these matrices are not reported here, they can be found in [60]. IPS was chosen in order to better exploit the shell-like capabilities of the present 1D structural formulation, as shown by Varello et al. [163].

Under the assumption of simple harmonic motion, it is possible to demonstrate that the vector that contains the dimensionless normalwash of all panels included in wing surface has the following expression (the boundary condition is enforced on all control points of wing surface):

$$\mathbf{w}_m = i \frac{\omega}{V_\infty} \mathcal{Z} + \frac{\partial \mathcal{Z}}{\partial x} \tag{6.20}$$

where all the vector quantities have to be understood as vectors of amplitudes of the harmonic motion and i is the imaginary unit.

6.3.2 The g-method

The generalized aerodynamic matrix for a given reduced frequency (k) is given by

$$Q_{ij}(ik) = \sum_{N=1}^{N_{AP}} \Delta p_j^N(ik) \tilde{Z}_i^N A^N \quad (6.21)$$

where

- $k = \omega b/L$, b is the reference length (equal to the half of the reference chord) and L is the length of the structure.
- $\Delta p_j^N(ik)$ is the pressure jump due to the j -th set of motions, acting on the N -th aerodynamic panel and evaluated for a given reduced frequency. The computation of the pressure jump is performed by means of the DLM.
- \tilde{Z}_i^N is the i -th motion set evaluated at the N -th aerodynamic panel. Starting from the i -th modal shape given by a structural formulation, the i -th motion set is then mapped on the aerodynamic panels by means of the splining process.
- A^N is the area of the N -th panel.

$\mathbf{Q}(ik)$ is a square matrix with $N_{\text{modes}} \times N_{\text{modes}}$ elements, where N_{modes} indicates the total number of natural modes adopted. Typically, N_{modes} ranges from 10 to 20.

The g-method was introduced by Chen [55] and it is based on a damping perturbation technique and a first-order model of the damping term. Its derivation exploits the aerodynamics in the Laplace domain and can be found in [55]. The basic assumption of the g-method is based on the following approximation of the generalized aerodynamic matrix:

$$\tilde{\mathbf{Q}}(p) \approx \tilde{\mathbf{Q}}^*(ik) + g\tilde{\mathbf{Q}}^{*'}(ik), \quad \text{for } g \ll 1 \quad (6.22)$$

where p is the nondimensional Laplace parameter ($p = g + ik$), $g = \gamma^k$ and γ is the transient decay rate coefficient. Equation (6.22) leads to the g-method equation of the aeroelastic problem

$$\left[\left(\frac{V_\infty}{b} \right)^2 \tilde{\mathbf{M}} p^2 + \tilde{\mathbf{K}} - \frac{1}{2} \rho V_\infty^2 \tilde{\mathbf{Q}}^{*'}(ik) g - \frac{1}{2} \rho V_\infty^2 \tilde{\mathbf{Q}}^*(ik) \right] \mathbf{q}(p) = \mathbf{0} \quad (6.23)$$

where the contribution of the structural damping has been neglected and $\tilde{\mathbf{M}}$ and $\tilde{\mathbf{K}}$ are the generalized mass and stiffness matrices, respectively (see Section 6.4).

The generalized aerodynamic matrix, $\tilde{\mathbf{Q}}^*(ik)$, is provided by the unsteady aerodynamic model (DLM) in the frequency domain. $\tilde{\mathbf{Q}}^{*'}(ik)$ is then obtained for a given number of k values and the computation of $\tilde{\mathbf{Q}}^{*'}(ik)$ has to be performed numerically. A central difference scheme can be used, for example. Three new matrices are introduced,

$$\begin{aligned} \mathbf{A} &= \left(\frac{V_\infty}{b} \right)^2 \tilde{\mathbf{M}} \\ \mathbf{B} &= 2ik \left(\frac{V_\infty}{b} \right)^2 \tilde{\mathbf{M}} - \frac{1}{2} \rho V_\infty^2 \tilde{\mathbf{Q}}^{*'}(ik) \\ \mathbf{C} &= -k^2 \left(\frac{V_\infty}{b} \right)^2 \tilde{\mathbf{M}} + \tilde{\mathbf{K}} - \frac{1}{2} \rho V_\infty^2 \tilde{\mathbf{Q}}^*(ik) \end{aligned} \quad (6.24)$$

Equation (6.23) therefore becomes

$$[g^2 \mathbf{A} + g \mathbf{B} + \mathbf{C}] \mathbf{q} = 0 \quad (6.25)$$

This is a second-order linear system in g ; the g-method targets to find those solutions having $\Im(g) = 0$. Equation (6.25) is rewritten in the state-space form,

$$[\mathbf{D} - g \mathbf{I}] \mathbf{X} = 0 \quad (6.26)$$

where

$$\mathbf{D} = \begin{bmatrix} \mathbf{0} & \mathbf{I} \\ -\mathbf{A}^{-1} \mathbf{C} & -\mathbf{A}^{-1} \mathbf{B} \end{bmatrix} \quad (6.27)$$

A so-called *reduced-frequency-sweep technique* is adopted to find the solution having $\Im(g) = 0$; i.e.

- a range of k values is chosen, along with a step Δk ;
- at each step i , the eigenvalues of \mathbf{D} are computed for $k_i = k_{i-1} + \Delta k$;
- a sign change of the imaginary part of each eigenvalue is searched for;
- if the sign change occurs AND $\Re(g) > 0$, the reduced flutter frequency will be computed by means of a linear interpolation.

Once k is found, the flutter frequency ω_f and damping are given by:

$$\omega_f = k (V_\infty / b) \quad (6.28)$$

$$\gamma = 2 \zeta = \frac{2 \Re(g)}{k} \quad (6.29)$$

6.4 Generalized mass and stiffness matrices

The generalized mass matrix is given by:

$$\tilde{\mathbf{M}} = \phi^T \mathbf{M} \phi \quad (6.30)$$

Where

- ϕ is a matrix containing a given number of modal shapes, dimension: $N_{DOF} \times N_{\text{modes}}$. N_{DOF} is the total number of DOFs of the structural model.
- \mathbf{M} is the mass matrix of the structure, dimension: $N_{DOF} \times N_{DOF}$.

$\tilde{\mathbf{M}}$ is a square diagonal matrix with $N_{\text{modes}} \times N_{\text{modes}}$ elements.

In the case of FEM, the evaluation of \mathbf{M} is straightforward (see Section 4.3). On the other hand, in the case of DSM (Section 3.2), matrix \mathbf{M} can be computed as follows:

$$\mathbf{M} = \frac{\mathbf{K} - \mathcal{K}(\omega_i)}{\omega_i^2} \quad (6.31)$$

where \mathbf{K} is the (“static”) structural matrix and it is evaluated as the DS matrix of Eq. (3.36), \mathcal{K} , at null frequency. ω_i is the oscillatory frequency associated to the i -th modal shape.

Similarly, the generalized stiffness matrix is a square diagonal ($N_{\text{modes}} \times N_{\text{modes}}$) matrix. Both in the case of FEM and DSM it is given by

$$\tilde{K}_{ii} = \omega_i^2 \tilde{M}_{ii} \quad (6.32)$$

Chapter 7

Discrete Gust Response

Gust loadings can affect different aspects of the aircraft's operation, such as its dynamic load, flight stability and safety, and control. In this chapter, simplified discrete gust response is discussed. First, basic ideas and formulas about vertical gust are given. The one-minus-cosine discrete gust idealization is then introduced and the corresponding time dependent incremental load factor is obtained. Next, in the second part of this chapter, the mode superposition method is described and used as an effective means for the solution of the linear, time-domain dynamic problem.

7.1 Vertical gust

Gusts loads, whether due to discrete gusts or continuous turbulence, are generally considered to be the result of a change in angle of attack due to a component of the gust velocity (U). In the case of vertical gust, such as the one depicted in Fig. 7.1, the change in angle of attack ($\Delta\alpha$), in radians, is approximately equal to the gust velocity divided by the forward speed (V_∞) of the aircraft; i.e.

$$\Delta\alpha \approx \frac{U}{V_\infty} \quad (7.1)$$

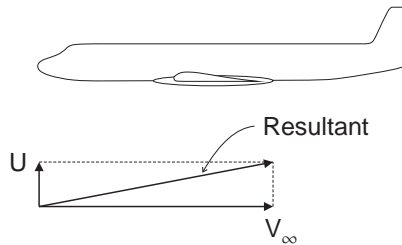


Figure 7.1: Vertical gust

The change in lift due to the gust is

$$\Delta L = \frac{\rho_\infty}{2} V_\infty^2 S C_{L_\alpha} \Delta\alpha \quad (7.2)$$

where $\frac{\rho_\infty}{2} V_\infty^2$ is the dynamic pressure, ρ_∞ being the air density; S is the reference wing area; and C_{L_α} is the lift curve slope. Equation (7.1) is substituted into Eq. (7.2). It reads

$$\Delta L = \frac{\rho_\infty}{2} V_\infty^2 S C_{L_\alpha} \frac{U}{V_\infty} = \frac{\rho_\infty}{2} U V_\infty S C_{L_\alpha} \quad (7.3)$$

Dividing by the airplane weight W , one has the incremental load factor Δn

$$\Delta n = \frac{\Delta L}{W} = \frac{\frac{\rho_\infty U V_\infty}{2}}{\left(\frac{W}{C_{L_\alpha} S}\right)} \quad (7.4)$$

7.2 One-minus-cosine discrete gust idealization

Gusts are random in nature and their profile tends to be continuous and irregular. Generally, when the profile is continuous, the gust structure is spoken of as turbulence. When the gust structure consists of more or less isolated pulses, the single pulse is referred to as a gust.

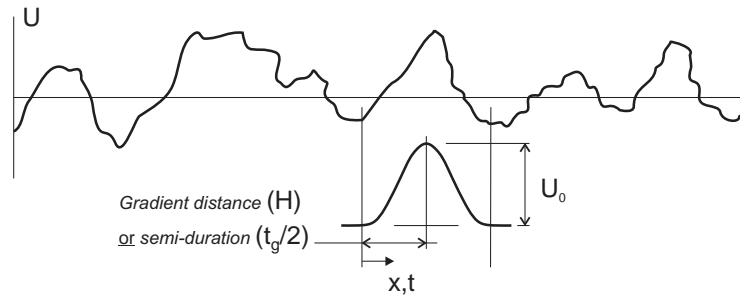


Figure 7.2: One-minus-cosine discrete gust idealization

The usual individual gust, or discrete gust, idealization of the gust structure consists of a one-minus-cosine pulse as shown in Fig. 7.2. The one-minus-cosine pulse can be either spatially distributed or temporarily distributed. In the former case, according to the notation adopted in Fig. 7.2, one has

$$U(x) = \frac{1}{2}U_0 \left(1 - \cos \frac{2\pi x}{2H}\right) \quad (7.5)$$

where H is the gust gradient distance and U_0 is the design gust velocity. Analogously, temporarily distributed gusts [150] can be expressed as follows:

$$U(t) = \frac{1}{2}U_0 \left(1 - \cos \frac{2\pi t}{t_g}\right) \quad (7.6)$$

where t_g is the duration of the gust. In this latter case, by substituting Eq. (7.6) into Eq. (7.4), the time-dependant incremental load factor is obtained

$$\Delta n = \frac{\frac{\rho_\infty U_0 V_\infty}{2}}{\left(\frac{W}{C_{L_\alpha} S}\right)} \left(1 - \cos \frac{2\pi t}{t_g}\right) \quad (7.7)$$

In this thesis, temporarily distributed gusts are addressed; hence, Eq. (7.7) is used to formulate the time-dependant loadings to be used in dynamic response analyses.

Discrete gust dynamic analyses are generally superseded by the continuous turbulence models [92]. However, it is well-known that aircraft companies perform dynamic discrete gust analyses for their own information, in addition to the continuous turbulence analysis on which primary reliance is based. The advantages of the discrete gust approach is the easier visualization of how the airplane is responding and its ease of use.

7.2.1 Effect of aeroelastic deformation on $C_{L\alpha}$

As the aircraft encounters a gust, the structure deforms in response to the forces developed. As a consequence, the aerodynamic forces vary. In using the gust loads in Eq. (7.7), it is reasonable to account for aeroelastic effects and use the appropriately modified value of $C_{L\alpha}$. Generally, as the result of the bending deformation of classical swept-back wings, the aeroelastic effects translate into a reduction in $C_{L\alpha}$. In fact, as the wing bends up, a streamwise section will experience a greater deflection at the trailing edge than at the leading edge, because the trailing edge corresponds to a more outboard location along the wing structural axis. However, this aeroelastic phenomenon decreases as the sweep angle of the wing becomes small and it is almost negligible for straight wings [92].

In a first approximation analysis, it can be reasonable to neglect the reduction of the $C_{L\alpha}$ due to aeroelasticity. This is the case of the simplified analyses conducted in the present thesis.

7.3 Solution of equations of motion in dynamic analysis

The equilibrium governing equations of the linear dynamic response of a multi-DOFs system can be expressed as follows [165]:

$$\mathbf{M}\ddot{\mathbf{q}}(t) + \mathbf{C}\dot{\mathbf{q}}(t) + \mathbf{K}\mathbf{q}(t) = \mathbf{P}(t) \quad (7.8)$$

where \mathbf{M} , \mathbf{C} , and \mathbf{K} are the mass, damping, and stiffness matrices; \mathbf{q} is the generalized displacements vector; and \mathbf{P} is the time-dependant loading vector that is calculated from Eq. (7.7) in the case of gust response analysis (see Section 4.4.1 for the formulation of inertial loads in the framework of CUF). The dot stands for derivative with respect to time (t).

Equation (7.8) represents a system of linear differential equations of second order with constant coefficient. In principle, the solution could be obtained by standard procedures (see for example Section 3.2.1). Nevertheless, in practical dynamic response analysis, we are interested in a few effective numerical methods, which can be subdivided into two main categories: direct integration and mode superposition.

In direct integration methods (e.g., central difference, Houbolt, and Newmark methods), Eq. (7.8) is integrated using a numerical step-by-step procedure [12, 50]. The term “*direct*” means that no transformation of the equations is performed prior to the numerical integration. Direct integrations methods are very effective and largely used for both linear and non-linear dynamic problems. However, large computational times may be required and they could be affected by possible instability due to error growth. In this thesis, we focus the attention on mode superposition method.

7.4 Mode superposition

We propose the following transformation on the n nodal¹ generalized displacements in \mathbf{q} :

$$\mathbf{q}(t) = \mathbf{T}\mathbf{x}(t) \quad (7.9)$$

¹Note that this procedure can be applied to all the numerical techniques described in this thesis (FEM, DSM, RBFs, etc.).

where \mathbf{T} is a $n \times n$ matrix and $\mathbf{x}(t)$ is a time-dependent vector of order n . The transformation matrix \mathbf{T} must be non-singular (i.e. $\text{rank}(\mathbf{T}) = n$) in order to have a unique relation between any vectors \mathbf{q} and \mathbf{x} . In practice, an effective transformation matrix is established using the solution of the un-damped free-vibration equations of motion, which is reduced into a linear (e.g. in the case of FEM or RBFs, see Sections 4.1.2 and 3.3 respectively) or non-linear (in the case of DSM, see Section 3.2) eigenvalue problem by assuming a harmonic solution. Briefly, the eigenproblem of the n -DOFs system under consideration yields the n eigensolutions (ω_1^2, Φ_1) , (ω_2^2, Φ_2) , ..., (ω_n^2, Φ_n) , where Φ_i are the \mathbf{M} -orthonormalized eigenvectors (see Section 6.4) and ω_i are the corresponding natural frequencies (rad/s).

We define a matrix Φ whose columns are the eigenvectors Φ_i , and a diagonal matrix Ω^2 that stores the eigenvalues ω_i^2

$$\Phi = \{\Phi_1, \Phi_2, \dots, \Phi_n\}, \quad \Omega^2 = \begin{bmatrix} \omega_1^2 & & & \\ & \omega_2^2 & & \\ & & \ddots & \\ & & & \omega_n^2 \end{bmatrix} \quad (7.10)$$

Since the eigenvectors are \mathbf{M} -orthogonal, we can demonstrate that

$$\Phi^T \mathbf{K} \Phi = \Omega^2, \quad \Phi^T \mathbf{M} \Phi = \mathbf{I} \quad (7.11)$$

where \mathbf{I} is the $n \times n$ identity matrix.

It is clear that matrix Φ would be a suitable transformation matrix \mathbf{T} in Eq. (7.9)

$$\mathbf{q}(t) = \Phi \mathbf{x}(t) \quad (7.12)$$

Hence, substituting Eq. (7.12) into the governing equations (Eq. (7.8)), pre-multiplying each term by Φ^T , and in light of the relations in Eq. (7.11) we obtain the equations of motion that correspond to the modal generalized displacements

$$\ddot{\mathbf{x}}(t) + \Phi^T \mathbf{C} \Phi \dot{\mathbf{x}}(t) + \Omega^2 \mathbf{x}(t) = \Phi^T \mathbf{P}(t) \quad (7.13)$$

The initial conditions on $\mathbf{x}(t)$ are obtained by using Eqs. (7.12) and (7.11)

$$\mathbf{x}(0) = \Phi^T \mathbf{M} \mathbf{q}(0), \quad \dot{\mathbf{x}}(0) = \Phi^T \mathbf{M} \dot{\mathbf{q}}(0) \quad (7.14)$$

7.4.1 Analysis with damping neglected

Equation (7.13) shows that if the damping is not included into the analysis, the equations of motion are decoupled. It reads

$$\ddot{\mathbf{x}}(t) + \Omega^2 \mathbf{x}(t) = \Phi^T \mathbf{P}(t) \quad (7.15)$$

Equation (7.15) represents a system of n individual equations of the form

$$\left. \begin{array}{l} \ddot{x}_i(t) + \omega_i^2 x_i(t) = r_i(t) \\ r_i(t) = \Phi_i \mathbf{P}(t) \end{array} \right\} \quad i = 1, 2, \dots, n \quad (7.16)$$

with initial conditions as defined in Eq. (7.14)

The solution of each equation in (7.16) can be derived, for example, by using the Duhamel integral

$$x_i(t) = \frac{1}{\omega_i} \int_0^t r_i(\tau) \sin \omega_i(t - \tau) d\tau + \alpha_i \sin \omega_i t + \beta_i \cos \omega_i t \quad (7.17)$$

where α_i and β_i are derived from the initial conditions (Eq. (7.14)).

For a complete response, the solution to all n equations in (7.16) must be computed; hence, $\mathbf{q}(t)$ is obtained by superposition of the response in each mode

$$\mathbf{q}(t) = \sum_{i=1}^n \Phi_i x_i(t) \quad (7.18)$$

However, the essence of the mode superposition method is that, generally, only a small fraction of the total number of decoupled equations needs to be considered in order to obtain a good approximate solution. Most frequently, only the first m equations of motion in (7.16) need to be used, with $m \ll n$. This means that we need to solve only for the lowest m eigenvalues and corresponding eigenvectors of the free-vibration problem, and we only sum in Eq. (7.18) the response in the first m modes. It reads:

$$\mathbf{q}^m(t) = \sum_{i=1}^m \Phi_i x_i(t) \quad (7.19)$$

where $\mathbf{q}^m(t)$ approximates the exact solution $\mathbf{q}(t)$ of Eq. (7.18).

7.4.2 Analysis with damping included

In general, when damping is included into the analysis, Eq. (7.13) cannot be decomposed into a system of decoupled equations. However, since generally the derivation of the damping properties cannot be carried out explicitly but only approximately, it is reasonable to use a damping matrix that allows an effective solution of the equations of motion and still includes all required effects.

The mode superposition method is particularly effective when assuming a proportional damping matrix of the form

$$\Phi_i^T \mathbf{C} \Phi_j = 2\omega_i \xi_i \delta_{ij} \quad (7.20)$$

where ξ_i is a modal damping parameter and δ_{ij} is the Kronecker delta ($\delta_{ij} = 1$ for $i = j$, $\delta_{ij} = 0$ otherwise). Equation (7.20) guarantees that the eigenvectors are also \mathbf{C} -orthonormal and Eq. (7.13) reduces into n decoupled equations as follows:

$$\ddot{x}_i(t) + 2\omega_i \xi_i \dot{x}_i + \omega_i^2 x_i(t) = r_i(t) \quad (7.21)$$

where $r_i(t)$ and the initial conditions have already been defined in Eq. (7.16). Therefore, the response can be calculated by evaluating the following Duhamel integral

$$x_i(t) = \frac{1}{\bar{\omega}_i} \int_0^t r_i(\tau) e^{-\xi_i \omega_i (t-\tau)} \sin \bar{\omega}_i (t-\tau) d\tau + e^{-\xi_i \omega_i t} (\alpha_i \sin \bar{\omega}_i t + \beta_i \cos \bar{\omega}_i t) \quad (7.22)$$

where $\bar{\omega}_i = \omega_i \sqrt{1 - \xi_i^2}$ and α_i and β_i are calculated from the initial conditions (Eq. (7.14)).

A special case of proportional damping that satisfies Eq. (7.20) is the Rayleigh damping

$$\mathbf{C} = \alpha \mathbf{M} + \beta \mathbf{K} \quad (7.23)$$

where α and β are constants. In this thesis, Rayleigh damping is used for some numerical applications. For more details about dynamic response analysis and related solution methodologies the reader is referred to [165, 12].

Chapter 8

Computational Fluid-Dynamics by CUF

Flow fields are described by the well-known Navier-Stokes equations, whose resolution is extremely challenging in almost every real situation. The main difficulties are due to turbulence and the mixing of different lengths it entails; accurate methods are therefore needed. In this chapter, a new higher-order 1D model for the computational fluid-dynamics is introduced. This model is formulated in the framework of CUF, which allows the physical quantities involved in the problem to be approximated by arbitrary accuracies through the use of generic polynomial expansions. The hierarchical p -version FEM is then discussed and used as an effective means to solve the related Galerkin formulation. Although the present methodology is here applied to the simplified problem of Stokes flows, its enhanced capabilities and efficiency is clear and provide confidence for future research in this direction.

8.1 Preface and notation

We consider the basic fluid mechanics of laminar, incompressible flows with constant (high) viscosity. This part of the thesis is due to the outstanding work initiated in [160], where CUF models were extended to Computational Fluid-Dynamics (CFD). In the research activities carried out in the present thesis, the previous work has been extended to include the p -version of FEM as approximation numerical technique. This extension is discussed hereinafter, together with a brief description of the Stokes equations and related 1D CUF approximation.

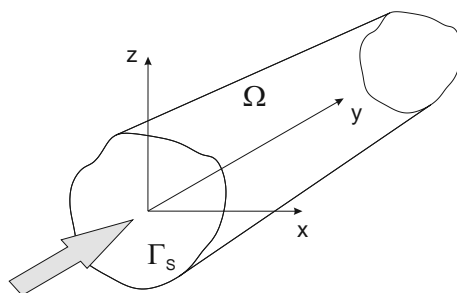


Figure 8.1: Computational domain Ω

We mainly consider 1D flows, namely pipe flows. The computational domain, considered fixed, is therefore assumed in a Cartesian coordinate system and having a geometry such as the one depicted in Fig. 8.1. In this chapter, we denote with Ω the three-dimensional volume domain in order to adopt the same notation as used in reference texts. Ω is usually called *computational domain* or *control volume*. It is bounded, and its bounding surface is denoted by $\partial\Omega$, whereas Γ is the symbol used to refer to a generic surface (two-dimensional) in the domain. The outwardly oriented unit vector normal to the boundary $\partial\Omega$ is indicated with \mathbf{n} .

8.2 Stokes equations

The Navier-Stokes equations leads to a non-linear set of ordinary differential equations because of the presence of the convective term (see [131]). This makes both the analysis and the numerical solution more difficult. However, when the fluid is highly viscous, the contribution of the non-linear convective term may be neglected.

Let the Reynolds number Re to be defined as follows:

$$Re = \frac{|\mathbf{U}| \mathcal{D}}{\nu} \quad (8.1)$$

where \mathcal{D} is a representative dimension of the domain Ω (e.g., the length of a tube wherein the fluid flow is studied); \mathbf{U} is a representative fluid velocity (e.g., the free stream velocity); $\nu = \mu/\rho$ is the kinematic viscosity [m^2/s]; and μ is the dynamic viscosity [$kg/(ms)$]. The Reynolds number measures the extent at which convection dominates over diffusion. When $Re \ll 1$ the convective term can be omitted, and the Navier-Stokes equations for incompressible flows with constant viscosity reduce to the so-called *Stokes equations* that, in the case of mixed Dirichlet–Neumann homogeneous boundary conditions, holds

$$\left\{ \begin{array}{ll} -\nu \Delta \mathbf{u} + \nabla p = \mathbf{f} & \text{in } \Omega \\ \nabla \cdot \mathbf{u} = 0 & \text{in } \Omega \\ \mathbf{u} = \mathbf{0} & \text{on } \Gamma_D \\ \nu \frac{\partial \mathbf{u}}{\partial \mathbf{n}} - p \mathbf{n} = \mathbf{0} & \text{on } \Gamma_N \end{array} \right. \quad (8.2)$$

where the first equation represents the momentum conservation equation, and the second one represents the continuity equation. In Eq. (8.2), $\Gamma_D \subset \partial\Omega$ is the domain boundary where the Dirichlet (or prescribed) boundary conditions are imposed; $\Gamma_N \subset \partial\Omega$ is the domain boundary where the Neumann (or applied stress) boundary conditions are imposed¹; \mathbf{u} [m/s] is the velocity vector; p [m^2/s^2] is the pressure scaled with respect to density; and \mathbf{f} [$N/kg = m/s^2$] is the vector of body forces (per mass unit) applied to the fluid. From Eq. (8.2), it is clear that the derivative with respect to time has also been neglected from Navier-Stokes equations. In fact, a Stokes flow is steady and has no dependence on time other than through time-dependent boundary conditions. For more details about the Navier-Stokes equations and the Stokes problem, the reader is referred to [131].

¹It is intended that $\Gamma_D \cup \Gamma_N = \partial\Omega$.

8.2.1 Weak formulation of the Stokes equations

The weak form of Stokes equations is formally obtained by taking the scalar product of the momentum equations with a vector function \mathbf{v} (called *test function*) belonging to a suitable functional space V (called *test function space*), integrating over the computational domain Ω and applying the Green integration formula. Similarly, the continuity equation is multiplied by a *scalar test function* q belonging to a suitable *test functional space* Q and integrated over the computational domain Ω .

The momentum conservation equation for the Stokes problem multiplied by a test function \mathbf{v} and integrated over Ω is:

$$\int_{\Omega} \left[-\nu \Delta \mathbf{u} \cdot \mathbf{v} + \nabla p \cdot \mathbf{v} \right] d\Omega = \int_{\Omega} \mathbf{f} \cdot \mathbf{v} d\Omega \quad (8.3)$$

By using the Green formula for the Laplacian operator and after some mathematical passages (see [160]), Eq. (8.3) becomes

$$\int_{\Omega} \nu \nabla \mathbf{u} : \nabla \mathbf{v} d\Omega - \int_{\Omega} p \nabla \cdot \mathbf{v} d\Omega = \int_{\partial\Omega} \left(\nu \frac{\partial \mathbf{u}}{\partial \mathbf{n}} - p \mathbf{n} \right) \cdot \mathbf{v} d\Gamma + \int_{\Omega} \mathbf{f} \cdot \mathbf{v} d\Omega \quad (8.4)$$

$\forall \mathbf{v} \in V$. The term $\nabla \mathbf{u} : \nabla \mathbf{v}$ in Eq. (8.4) is

$$\nabla \mathbf{u} : \nabla \mathbf{v} = \text{tr} (\nabla \mathbf{u}^T \nabla \mathbf{v}) \quad (8.5)$$

where the symbol tr stands for the trace of a square matrix.

The mass conservation of the Stokes equation (second expression in Eq. 8.2) multiplied by a test function q , belonging to a suitable functional space Q , and integrated over Ω is:

$$- \int_{\Omega} q \nabla \cdot \mathbf{u} d\Omega = 0 \quad (8.6)$$

$\forall q \in Q$. It should be noted that the negative sign in Eq. (8.6) has been included only for the sake of convenience.

Nonhomogeneous boundary conditions

In the more general case of mixed Dirichlet–Neumann nonhomogeneous boundary conditions; i.e.,

$$\begin{cases} \mathbf{u} = \mathbf{g}^D & \text{on } \Gamma_D \\ \nu \frac{\partial \mathbf{u}}{\partial \mathbf{n}} - p \mathbf{n} = \mathbf{t}^N & \text{on } \Gamma_N \end{cases} \quad (8.7)$$

the weak form of the Stokes equations is

$$\begin{cases} \int_{\Omega} \nu \nabla \mathbf{u} : \nabla \mathbf{v} d\Omega - \int_{\Omega} p \nabla \cdot \mathbf{v} d\Omega = \int_{\partial\Omega} \left(\nu \frac{\partial \mathbf{u}}{\partial \mathbf{n}} - p \mathbf{n} \right) \cdot \mathbf{v} d\Gamma + \\ \int_{\Omega} \mathbf{f} \cdot \mathbf{v} d\Omega & \forall \mathbf{v} \in V \\ - \int_{\Omega} q \nabla \cdot \mathbf{u} d\Omega = 0 & \forall q \in Q \end{cases} \quad (8.8)$$

Homogeneous boundary conditions

When mixed Dirichlet–Neumann homogeneous boundary conditions are considered, the corresponding weak form can be seen as a particular case of Eq. (8.8). In fact, the integral term on the boundary $\partial\Omega$ in Eq. (8.8) can be expressed as a summation of two integrals over Γ_D and Γ_N . On the other hand, the test function space V is chosen in such a way that the test functions \mathbf{v} vanish over Γ_D . It is therefore straightforward to demonstrate that, in the case of homogeneous boundary conditions,

$$\int_{\partial\Omega} \left(\nu \frac{\partial \mathbf{u}}{\partial \mathbf{n}} - p \mathbf{n} \right) \cdot \mathbf{v} \, d\Gamma = 0 \quad (8.9)$$

Hence, the weak form of the Stokes problem with mixed Dirichlet–Neumann homogeneous boundary conditions in Eq. (8.2) is

$$\begin{cases} \int_{\Omega} \nu \nabla \mathbf{u} : \nabla \mathbf{v} \, d\Omega - \int_{\Omega} p \nabla \cdot \mathbf{v} \, d\Omega = \int_{\Omega} \mathbf{f} \cdot \mathbf{v} \, d\Omega & \forall \mathbf{v} \in V \\ - \int_{\Omega} q \nabla \cdot \mathbf{u} \, d\Omega = 0 & \forall q \in Q \end{cases} \quad (8.10)$$

8.2.2 Galerkin approximation

The Galerkin approximation of the Stokes problem in Eq. (8.10) has the following form:

Find $\mathbf{u}_h \in V_h$, $p_h \in Q_h$ such that

$$\begin{cases} \int_{\Omega} \nu \nabla \mathbf{u}_h : \nabla \mathbf{v}_h \, d\Omega - \int_{\Omega} p_h \nabla \cdot \mathbf{v}_h \, d\Omega = \int_{\Omega} \mathbf{f} \cdot \mathbf{v}_h \, d\Omega & \forall \mathbf{v}_h \in V_h \\ - \int_{\Omega} q_h \nabla \cdot \mathbf{u}_h \, d\Omega = 0 & \forall q_h \in Q_h \end{cases} \quad (8.11)$$

Let the bilinear forms $a : V \times V \rightarrow \mathbb{R}$ and $b : V \times Q \rightarrow \mathbb{R}$ to be now defined as follows:

$$a(\mathbf{u}, \mathbf{v}) = \int_{\Omega} \nu \nabla \mathbf{u} : \nabla \mathbf{v} \, d\Omega \quad (8.12)$$

$$b(\mathbf{u}, q) = - \int_{\Omega} q \nabla \cdot \mathbf{u} \, d\Omega \quad (8.13)$$

With this notation, the Galerkin approximation of the Stokes equation reads

Find $\mathbf{u}_h \in V_h$, $p_h \in Q_h$ such that

$$\begin{cases} a(\mathbf{u}_h, \mathbf{v}_h) + b(\mathbf{v}_h, p_h) = (\mathbf{f}, \mathbf{v}_h) & \forall \mathbf{v}_h \in V_h \\ b(\mathbf{u}_h, q_h) = 0 & \forall q_h \in Q_h \end{cases} \quad (8.14)$$

where $V_h \subset V$ and $Q_h \subset Q$ represent two families of finite dimensional subspaces depending on a real positive discretization parameter h .

8.3 One-dimensional CUF models for Stokes flows

Several types of flows in nature can be considered as mono-dimensional, e.g. flows in arteries and pipes. It is, therefore, reasonable to approximate the fluid mechanics equations via 1D models. Nevertheless, simplified models cannot account for higher-order phenomena and refined models may be necessary.

1D CUF models introduced in Chapter 2 are here used along with FEM to approximate the Galerkin formulation of the Stokes equations. The attention is focused on TE models and on the hierarchical capabilities of CUF, which enables one to automatically formulate higher-order 1D models able to provide very accurate results with low computational efforts.

8.3.1 Velocity and pressure field approximations

According to CUF, the velocity field \mathbf{u}_h is assumed to be an expansion of generic functions F_τ^U on the cross-section (Γ_S in Fig. 8.1) of the 1D domain; i.e.

$$\mathbf{u}_h(x, y, z) = F_\tau^U(x, z) \mathbf{u}_\tau(y), \quad \tau = 1, \dots, M^U \quad (8.15)$$

where the repeated subscript τ indicates summation; M^U is the number of terms in the expansion, $M^U = (N^U + 1)(N^U + 2)/2$; and N^U is the theory expansion order, which is a free parameter of the formulation. According to TE, in fact, the cross-sectional F_τ^U functions consists here of MacLaurin polynomials of order N^U as detailed in Section 2.2.1. The choice of cross-sectional functions in the framework of CUF is arbitrary although.

Similarly, the discrete pressure field p_h is assumed to be an expansion on the cross-section Γ_S by generic functions F_m^P

$$p_h(x, y, z) = F_m^P(x, z) p_m(y) \quad m = 1, \dots, M^P \quad (8.16)$$

where m indicates summation; M^P is the number of terms used in the expansion, $M^P = (N^P + 1)(N^P + 2)/2$; and F_m^P are MacLaurin polynomials of order N^P . It is noteworthy that, in general, N^U must not be necessarily equal to N^P .

FEM discretization

The generalized velocity and pressure quantities, $\mathbf{u}_\tau(y)$ and p_m , are discretized by FEM along the longitudinal axis. By following Chapter 4, one has

$$\mathbf{u}_\tau(y) = N_i^U(y) \mathbf{q}_{\tau i}, \quad i = 1, \dots, p^U + 1 \quad (8.17)$$

$$p_m(y) = N_t^P(y) p_{mt}, \quad i = 1, \dots, p^P + 1 \quad (8.18)$$

where i and t represent summation; $\mathbf{q}_{\tau i}$ and p_{mt} are the nodal velocity and pressure unknowns, respectively; p^U is the order of the 1D FEM element used to discretize the velocity field; and p^P is the order of the 1D FEM element used to discretize the pressure scalar field.

The shape functions N_i^U and N_t^P can be arbitrary and in general different. In this thesis both Lagrange (see Eqs. (4.4) to (4.6)) and Legendre-like hierarchical shape functions have been used for the approximation of the fluid-dynamics problem. The latter shape functions result in the well-known *p-version* FEM (see [152]), which essentially exploit the following

one-dimensional shape functions:

$$\begin{aligned} N_1 &= \frac{1}{2}(1-r) \\ N_2 &= \frac{1}{2}(1+r) \\ N_i &= \phi_{i-1}(r), \quad i = 3, 4, \dots, p+1 \end{aligned} \quad (8.19)$$

with

$$\begin{aligned} \phi_j(r) &= \sqrt{\frac{2j-1}{2}} \int_{-1}^r L_{j-1}(y) dy \\ &= \frac{1}{\sqrt{4j-2}} (L_j(r) - L_{j-2}(r)), \quad j = 2, 3, \dots \end{aligned} \quad (8.20)$$

where N_1, N_2, \dots, N_{p+1} are either N_i^U or N_t^P shape functions; p is either p^U or p^P ; and $L_j(r)$ are the Legendre polynomials [152]. These shape functions are attractive in computational mechanics because of the orthogonality property of the Legendre polynomials.

Combining the FE approximation in Eqs. (8.17) and (8.18) with CUF (Eqs. (8.15) and (8.16)), the final expressions of the approximated velocity and pressure fields by the present 1D higher-order model hold

$$\mathbf{u}_h(x, y, z) = F_\tau^U(x, z) N_i^U(y) \mathbf{q}_{\tau i}, \quad \tau = 1, \dots, M^U \quad i = 1, \dots, p^U + 1 \quad (8.21)$$

$$p_h(x, y, z) = F_m^P(x, z) N_t^P(y) p_{mt}, \quad m = 1, \dots, M^P \quad t = 1, \dots, p^P + 1 \quad (8.22)$$

8.3.2 CFD fundamental nuclei

According to 1D CUF, the generic discrete test functions $\mathbf{v}_h \in V_h$ and $q_h \in Q_h$ are approximated in a manner equivalent to Eqs. (8.21) and (8.22), respectively. It is sufficient, therefore, that the Galerkin approximation in Eq. (8.11) is verified for each function of the basis of V_h and Q_h , because all the functions in the space V_h and Q_h are a linear combination of the basis functions (see [19, 131]). Hence, the solution of the Galerkin approximation in the framework of CUF comes from the following system of equations:

Find $\mathbf{u}_h \in V_h$, $p_h \in Q_h$ such that

$$\begin{cases} a(\mathbf{u}_h, \boldsymbol{\varphi}_{\tau i e}) + b(\boldsymbol{\varphi}_{\tau i e}, p_h) = (\mathbf{f}, \boldsymbol{\varphi}_{\tau i e}) & \forall \tau, \forall i, \forall e \\ b(\mathbf{u}_h, \phi_{mt}) = 0 & \forall m, \forall t \end{cases} \quad (8.23)$$

with $\tau = 1, \dots, M^U$, $i = 1, \dots, p^U + 1$, $e = 1, \dots, 3$, $m = 1, \dots, M^P$, $t = 1, \dots, p^P + 1$. The index e refers to the three components of the velocity field, and

$$\boldsymbol{\varphi}_{\tau i e}(x, y, z) = \begin{cases} \delta_{1e} F_\tau^U(x, z) N_i^U(y) \\ \delta_{2e} F_\tau^U(x, z) N_i^U(y) \\ \delta_{3e} F_\tau^U(x, z) N_i^U(y) \end{cases} \quad (8.24)$$

where $\delta_{ie} = 1$ if $e = i$, 0 otherwise. Similarly

$$\phi_{mt}(x, y, z) = F_m^P(x, z) N_t^P(y) \quad (8.25)$$

For the sake of convenience, indexes s (instead of τ) and j (instead of i) are introduced into Eq. (8.23) for the CUF approximation of the discrete solution \mathbf{u}_h (see Eq. (8.21)).

After extensive mathematical manipulations (see [160]), Eq. (8.23) becomes the following system of algebraic equations:

$$\begin{cases} \mathbf{A}^{\tau s i j} \mathbf{q}_{s j} + \mathbf{B}^{\tau m i t T} p_{m t} = \mathbf{F}^{\tau i} \\ \mathbf{B}^{m s t j} \mathbf{q}_{s j} = \mathbf{0} \end{cases} \quad (8.26)$$

where $\mathbf{A}^{\tau s i j}$ is the fundamental nucleus related to the bilinear form $a(\mathbf{u}_h, \varphi_{\tau i e})$ of the 1D CUF model;

$$\begin{aligned} \mathbf{A}^{\tau s i j} = & \left[\nu \int_L N_i^U N_j^U dy \int_{\Gamma_S} F_{\tau, x}^U F_{s, x}^U d\Gamma + \nu \int_L N_{i, y}^U N_{j, y}^U dy \int_{\Gamma_S} F_{\tau}^U F_s^U d\Gamma + \right. \\ & \left. \nu \int_L N_i^U N_j^U dy \int_{\Gamma_S} F_{\tau, z}^U F_{s, z}^U d\Gamma \right] \mathbf{I} \end{aligned} \quad (8.27)$$

$\mathbf{B}^{\tau m i t T}$ is the fundamental nucleus of the bilinear form $b(\varphi_{\tau i e}, p_h)$;

$$\mathbf{B}^{\tau m i t T} = \begin{pmatrix} - \int_L N_i^U N_t^P dy \int_{\Gamma_S} F_{\tau, x}^U F_m^P d\Gamma \\ - \int_L N_{i, y}^U N_t^P dy \int_{\Gamma_S} F_{\tau}^U F_m^P d\Gamma \\ - \int_L N_i^U N_t^P dy \int_{\Gamma_S} F_{\tau, z}^U F_m^P d\Gamma \end{pmatrix} \quad (8.28)$$

$\mathbf{B}^{m s t j}$ is the fundamental nucleus of the the bilinear form $b(\mathbf{u}_h, \phi_{m t})$;

$$\mathbf{B}^{m s t j} = \begin{pmatrix} - \int_L N_t^P N_j^U dy \int_{\Gamma_S} F_m^P F_{s, x}^U d\Gamma \\ - \int_L N_t^P N_{j, y}^U dy \int_{\Gamma_S} F_m^P F_s^U d\Gamma \\ - \int_L N_t^P N_j^U dy \int_{\Gamma_S} F_m^P F_{s, z}^U d\Gamma \end{pmatrix}^T \quad (8.29)$$

and $\mathbf{F}^{\tau i}$ is the fundamental nucleus related to the term $(\mathbf{f}, \varphi_{\tau i e})$.

$$\mathbf{F}^{\tau i} = \int_{\Omega} F_{\tau}^U N_i^U \mathbf{f} d\Omega \quad (8.30)$$

In Eq. (8.27), \mathbf{I} is the 3×3 identity matrix.

Similarly to CUF models for elasticity, the mathematical expressions of the nuclei are formally independent of the theory orders (N^U and N^P) and on the FEM shape functions (p^U and p^P). The fundamental nuclei above have to be expanded on the indexes τ , s , m , i , j , and t . This expansion leads to the construction of the elemental FE arrays associated to the Galerkin approximation of the Stokes problem. The expansion is carried out by following a scheme very similar to the one described in Section 4.2 and Fig. 4.1. Assembling all the finite elements, the final system of equations is formulated as

$$\begin{cases} \mathbf{A} \mathbf{q} + \mathbf{B}^T \mathbf{p} = \mathbf{F} \\ \mathbf{B} \mathbf{q} = \mathbf{0} \end{cases} \quad (8.31)$$

It is interesting to note the following relation between the nuclei of the matrices \mathbf{B}^T and \mathbf{B} :

$$\mathbf{B}^{m s t j T} = \mathbf{B}^{\tau m i t} \quad (8.32)$$

which is formally true aside from the use of different indices.

8.4 Boundary conditions

Equation (8.31) does not include boundary conditions prescribed on the boundaries. A typical problem considered in this thesis is shown in Fig. 8.2, where the boundary surface $\partial\Omega$ of a tube are divided into inlet, outlet and lateral surfaces, namely $\partial\Omega = \Gamma^{\text{in}} \cup \Gamma^{\text{out}} \cup \Gamma^{\text{l}}$. Subscripts in Fig. 8.2 indicate that either Dirichlet (D) or Neumann (N) boundary conditions are applied.

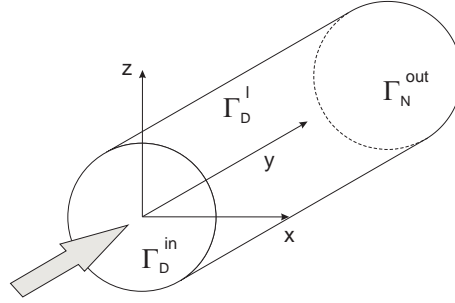


Figure 8.2: Pipe with circular cross-section

Regarding homogeneous Neumann boundary conditions², they are implicitly satisfied by the solution of the problem in Eq. (8.31). On the other hand, the imposition of Dirichlet boundary conditions requires the involvement of some mathematical passages. Briefly, let the generic Dirichlet boundary condition be defined as follows:

$$\mathbf{u}|_{\Gamma_D} = \mathbf{g}^D \quad (8.33)$$

where \mathbf{g}^D is an arbitrary known function and Γ_D is either a generic cross-section of the tube (e.g. Γ_D^{in}) or the lateral surface Γ_D^{l} . Equation (8.33) is imposed by formulating the correspondent Galerkin approximation; i.e.,

Find $\mathbf{u}_h \in V_h$ such that

$$\int_{\Gamma_D} \mathbf{u}_h \cdot \mathbf{v}_h \, d\Gamma = \int_{\Gamma_D} \mathbf{g}^D \cdot \mathbf{v}_h \, d\Gamma \quad \forall \mathbf{v}_h \in V_h \quad (8.34)$$

By substituting CUF and FEM approximation into Eq. (8.34), the imposition of the Dirichlet boundary condition is written in terms of fundamental nuclei as in the following linear system:

$$\mathbf{A}_{BC}^{\tau s i j} \mathbf{q}_{s j} = \mathbf{F}_{BC}^{\tau i} \quad (8.35)$$

In the case of boundary condition applied on a tube cross-section, the fundamental nuclei are

$$\mathbf{A}_{BC}^{\tau s i j} = \left[N_i^U(y_g) N_j^U(y_g) \int_{\Gamma_D} F_\tau^U F_s^U \, d\Gamma \right] \mathbf{I} \quad (8.36)$$

$$\mathbf{F}_{BC}^{\tau i} = N_i^U(y_g) \int_{\Gamma_D} F_\tau^U \mathbf{g}^D \, d\Gamma \quad (8.37)$$

²Nonhomogeneous Neumann boundary conditions are not considered in this thesis.

where y_g is the coordinate along y of the cross-section where the condition is imposed. In the case of boundary condition applied on Γ_D^1 , the fundamental nuclei are

$$\mathbf{A}_{BC}^{\tau s i j} = \left[\int_L N_i^U N_j^U dy \int_{\gamma_S} F_\tau^U F_s^U d\gamma \right] \mathbf{I} \quad (8.38)$$

$$\mathbf{F}_{BC}^{\tau i} = \int_{\Gamma_D} N_i^U F_\tau^U \mathbf{g}^D d\Gamma \quad (8.39)$$

where γ_S is the contour of the cross-section.

The nuclei of the Dirichlet boundary conditions have to be expanded according to the summation indexes, assembled, and then imposed to Eq. (8.31) by penalization method; i.e.,

$$\begin{cases} [\mathbf{A} + \alpha \mathbf{A}_{BC}] \mathbf{q} + \mathbf{B}^T \mathbf{p} = [\mathbf{F} + \alpha \mathbf{F}_{BC}] \\ \mathbf{B} \mathbf{q} = \mathbf{0} \end{cases} \quad (8.40)$$

where α is a high penalty value. Equation (8.40) represents the final algebraic system of equations to be solved. For further details about the CUF formulation of the Stokes problem, the reader is referred to [160].

Chapter 9

Numerical Results

Selected analyses and results are discussed in this chapter. In the first part, the proposed structural CUF models are assessed. Both strong and weak form solutions for free vibrations of beams are provided. Multi-line and component-wise analyses of simple and complex structures, including composite materials, are subsequently presented. In the second part, flutter instabilities and gust response of various aircraft structures are discussed. Finally, CUF models for fluid-dynamics are validated. The attention is focused on the capability of the proposed methodology to carry out enhanced analyses of complex problems with very low computational efforts.

9.1 Comparison of FEM, DSM and RBFs for free vibrations

The strong form solutions for free vibrations of classical and refined CUF 1D models as discussed in Chapter 3 are assessed in this section. Both solid and thin-walled metallic structures as well as a composite laminate are considered. Results by RBFs and DSM methods are compared to FEM approximations of CUF models and of those available in commercial codes and in the literature. Further results can be found in [119, 121, 120, 38, 122]. The attention is focused on the accuracy of the diverse numerical methods adopted and on the higher-order capabilities of the TE CUF models.

9.1.1 Rectangular cross-section beam

A beam with a solid rectangular cross-section such as the one shown in Fig. 9.1 is considered first. For illustrative purposes, it is assumed that the beam has a square cross-section ($a = b$), with $b = 0.2$ m and length L such that $L/b = 10$. The material data are: Young modulus, $E = 75$ GPa, Poisson ratio, $\nu = 0.33$, material density, $\rho = 2700$ kg/m³.

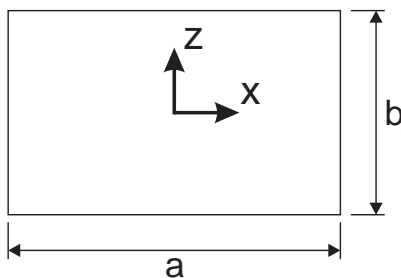


Figure 9.1: Solid rectangular cross-section

No. Elem.	p	EBBM	TBM	$N = 1$	$N = 2$	$N = 3$	$N = 4$
I Bending mode							
FEM							
10	1	2.873	2.842	2.842	2.847	2.843	2.843
20	1	2.846	2.816	2.816	2.818	2.813	2.813
40	1	2.840	2.809	2.809	2.810	2.806	2.806
10	2	2.838	2.807	2.807	2.808	2.803	2.803
20	2	2.838	2.807	2.807	2.808	2.803	2.803
DSM							
		2.838	2.807	2.807	2.808	2.803	2.803
II Bending mode							
FEM							
10	1	11.775	11.292	11.292	11.378	11.304	11.304
20	1	11.350	10.904	10.904	10.931	10.864	10.863
40	1	11.247	10.810	10.810	10.823	10.758	10.757
10	2	11.216	10.782	10.782	10.791	10.726	10.725
20	2	11.213	10.779	10.779	10.788	10.723	10.722
40	2	11.213	10.779	10.779	10.787	10.723	10.722
10	3	11.213	10.779	10.779	10.787	10.723	10.722
DSM							
		11.213	10.779	10.779	10.787	10.723	10.722
III Bending mode							
FEM							
10	1	27.587	25.209	25.209	25.611	25.266	25.260
20	1	25.409	23.409	23.409	23.526	23.245	23.241
40	1	24.905	22.988	22.988	23.042	22.775	22.771
10	2	24.777	22.881	22.881	22.916	22.653	22.649
20	2	24.743	22.852	22.852	22.886	22.623	22.619
40	2	24.740	22.850	22.850	22.884	22.621	22.617
10	3	24.740	22.850	22.850	22.884	22.621	22.617
20	3	24.740	22.849	22.849	22.884	22.621	22.617
40	3	24.740	22.849	22.849	22.884	22.621	22.617
DSM							
		24.742	22.849	22.849	22.884	22.621	22.617
IV Bending mode							
FEM							
10	1	51.823	44.543	44.543	45.676	44.680	44.647
20	1	44.865	39.400	39.400	39.707	38.995	38.975
40	1	43.339	38.236	38.237	38.371	37.713	37.697
10	2	43.038	38.006	38.005	38.097	37.448	37.432
20	2	42.860	37.868	37.868	37.950	37.309	37.292
40	2	42.848	37.859	37.859	37.940	37.300	37.283
10	3	42.849	37.860	37.860	37.941	37.301	37.284
DSM							
		42.853	37.858	37.858	37.939	37.298	37.282

Table 9.1: First to fourth non-dimensional bending frequencies $\omega^* = \frac{\omega L^2}{b} \sqrt{\frac{\rho}{E}}$ for the SS square beam; $L/b = 10$

Table 9.1 shows the first four bending natural frequencies in non-dimensional form ($\omega^* = \frac{\omega L^2}{b} \sqrt{\frac{\rho}{E}}$) for a simply-supported (SS) square beam using both DSM and FEM solutions based on TE models. Higher-order TE finite elements by Lagrange shape functions with 2, 3 and 4 nodes were used in the FEM solutions, or in other words, linear, quadratic

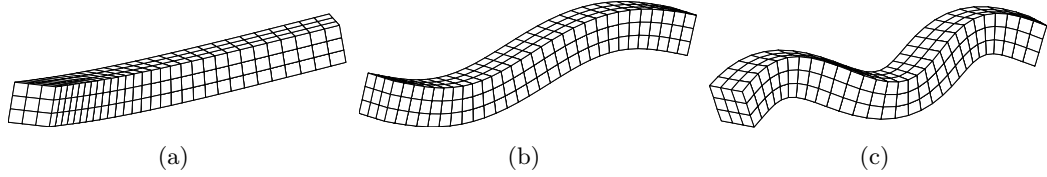


Figure 9.2: First (a), second (b) and third (c) bending modes for a SS square beam ($L/b = 10$); DSM $N = 4$ TE model

Model	I Bending	II Bending	I Torsional	II Torsional
MSC Nastran model				
Solid	1.016	6.088	8.852	26.516
Classical and refined TE, DSM solutions				
$N = 5$	1.013	6.069	8.868	26.603
$N = 4$	1.013	6.070	8.871	26.619
$N = 3$	1.014	6.075	9.631	28.893
$N = 2$	1.015	6.107	9.631	28.893
TBM	1.008	6.069	-*	-
Classical and refined TE, RBFs solutions				
$N = 5$	1.011	6.075	8.872	26.605
$N = 4$	1.012	6.078	8.875	26.623
$N = 3$	1.013	6.081	9.634	28.895
$N = 2$	1.014	6.115	9.634	28.895
TBM	1.007	6.076	-	-

*: not provided by the model

Table 9.2: Non-dimensional natural periods $\omega^* = \frac{\omega L^2}{b} \sqrt{\frac{\rho}{E}}$ for the CF square beam; $L/b = 10$

and cubic approximations along the y -axis were adopted. Classical beam theories (TBM), linear ($N = 1$), quadratic ($N = 2$), cubic ($N = 3$) and fourth-order ($N = 4$) TE models are considered. It is clearly shown that, as far as FEM solutions of CUF higher-order models are concerned, the number of beam elements that are necessary to obtain accurate results - provided by the DSM - increases as natural frequencies as well as beam theory order increase.

Figure 9.2 shows the first three bending modes of the beam with SS boundary conditions obtained from the DSM analysis when using a $N = 4$ TE model. It should be emphasized that DSM results are mesh independent and the mesh used in Fig. 9.2 is merely a plotting grid for convenience.

One of the most important features of the DSM is that it provides exact solutions for any kind of boundary conditions. Moreover, TE higher-order theories are able to take into account several non-classical effects such as warping, in-plane deformations, shear effects and bending-torsion couplings as demonstrated in [33]. In Table 9.2, the first two bending modes and the first two torsional modes for a clamped-free (CF) short ($L/b = 10$) square beam are shown. In this table, RBFs solutions of classical and higher-order TE models are compared to exact solutions by DSM. RBFs results are obtained by considering 37 collocation points and a shape parameter $c = \frac{2.4}{L}$. Results obtained by 3D FEM models using MSC Nastran [113] are also shown in Table 9.2. The generic three-dimensional

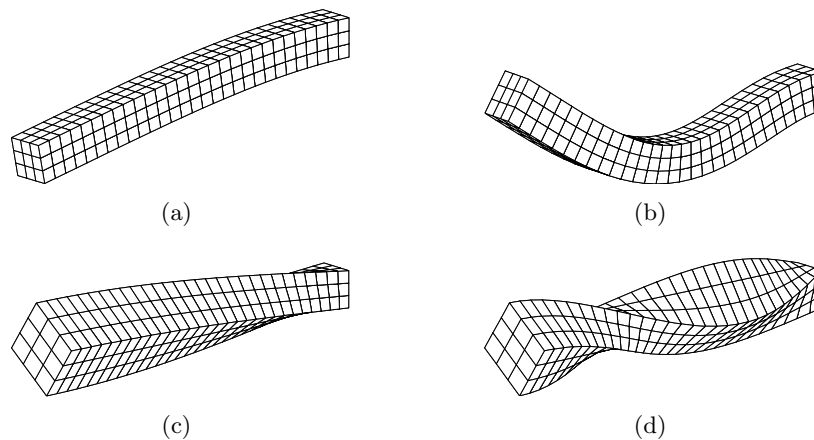


Figure 9.3: First bending (a), second bending (b), first torsional (c) and second torsional (d) modes for a CF square cross-section beam ($L/b = 10$); DSM $N = 5$ TE model

FEM solution is herein referred to as “Solid”. In the results shown in Table 9.2, Solid is built using 8-node CHEXA Nastran elements. Figure 9.3 shows some representative modal shapes by DSM for the fifth-order TE model of the CF beam. Some comments are relevant:

- According to 3D MSC Nastran solution, the present lower-order TE models are able to characterize the bending behaviour of solid cross-section beams.
- DSM provides exact solutions. Although, FEM and RBFs methods give reliable results when applied to CUF refined beam models of compact cross-section beams.
- A fourth-order ($N = 4$) TE model is necessary to correctly detect torsional frequencies.

9.1.2 Thin-walled cylinder

A thin-walled cylinder is considered to further highlight the higher-order capabilities of the present structural formulation. The cross-section geometry is shown in Fig. 9.4. The cylinder has the outer diameter d equal to 2 m, thickness $t = 0.02$ m, and length $L = 20$ m. The structure is made of the same metallic material as in the previous example.

Table 9.3 shows the natural frequencies of the thin-walled cylinder for different boundary conditions (BCs). In particular, free-free (FF), clamped-free (CF), clamped-clamped (CC), as well as simply-supported (SS) ends are considered. Both classical TBM and

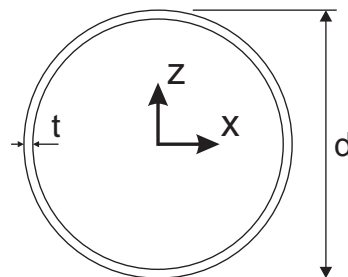


Figure 9.4: Cross-section of the thin-walled cylinder

9.1. Comparison of FEM, DSM and RBFs for free vibrations

BCs	Model	I Bending	II Bending	I Shell-like	II Shell-like	I Torsional	II Torsional
SS	Shell	13.978	51.366	14.913	22.917	80.415	160.810
	$N = 5$, DSM	14.022	51.503	18.405	25.460	80.786	161.573
	$N = 5$, RBFs	14.294	51.567	18.608	25.574	80.639	162.551
	$N = 3$, DSM	14.022	51.520	34.935	61.300	80.787	161.572
	$N = 3$, RBFs	14.295	51.583	35.049	61.353	80.847	161.712
	TBM, DSM	14.182	53.542	-*	-	-	-
	TBM, RBFs	14.459	53.604	-	-	-	-
CC	Shell	28.498	68.960	17.396	30.225	80.415	160.810
	$N = 5$, DSM	28.576	69.110	20.484	32.222	80.786	161.573
	$N = 5$, RBFs	28.354	69.096	20.463	31.974	80.838	161.596
	$N = 3$, DSM	28.605	69.199	38.690	70.333	80.787	161.572
	$N = 3$, RBFs	28.259	68.921	38.889	70.056	80.838	161.596
	TBM, DSM	30.302	76.443	-	-	-	-
	TBM, RBFs	30.435	76.489	-	-	-	-
CF	Shell	5.059	29.001	14.235	17.435	40.209	120.620
	$N = 5$, DSM	5.076	29.088	17.805	20.580	40.394	121.181
	$N = 4$, DSM	5.077	29.090	23.069	25.239	40.393	121.181
	$N = 4$, RBFs	5.047	29.002	23.003	24.979	40.431	121.203
	$N = 3$, DSM	5.079	29.104	26.882	49.252	40.393	121.181
	$N = 3$, RBFs	5.059	28.953	26.934	49.356	40.431	121.203
	TBM, DSM	5.108	30.237	-	-	-	-
	TBM, RBFs	5.060	30.312	-	-	-	-
FF	Shell	30.829	76.806	14.129	14.171	80.415	160.810
	$N = 5$, DSM	30.932	77.041	17.709	17.777	80.788	161.576
	$N = 4$, DSM	30.932	77.043	22.987	23.053	80.789	161.577
	$N = 4$, RBFs	30.945	77.052	22.864	23.048	80.787	161.592
	$N = 3$, DSM	30.935	77.090	22.987	34.700	80.789	161.576
	$N = 3$, RBFs	31.121	77.099	23.043	34.678	80.787	161.592
	TBM, DSM	31.338	80.275	-	-	-	-
	TBM, RBFs	31.341	80.286	-	-	-	-

*: not provided by the model

Table 9.3: Natural frequencies (Hz) of the thin-walled cylinder for different boundary conditions; Comparison of RBFs and DSM solutions

higher-order CUF beam models are shown in Table 9.3, where the results by the RBFs-based method are compared to exact DSM higher-order TE beam models and MSC Nas-tran 2D FE (Shell) solutions obtained by using CQUAD4 elements. In the case of RBFs, a number of centers equal to 31 and a shape parameter $c = \frac{2.4}{L}$ were used. It is shown that classical and lower-order beam models are able to capture bending and torsional modes, whereas 1D higher-order theories are mandatory in order to detect local shell-like modes in accordance with 2D solutions.

Figure 9.5 shows the percentage error between the present RBFs method and exact reference solution from DSM. In Fig. 9.5 the first bending, torsional, and shell-like modes for different expansion orders N and boundary conditions are considered. It is shown that, for fixed values of the parameters c and number of centers n , bending and torsional modes exhibit a good convergence for all the boundary conditions and theory order considered. On the other hand, shell-like modes become unstable if higher than fourth-order ($N = 4$) models and CF or FF boundary conditions are examined. This is the reason why in Table 9.3 only up to $N = 4$ models are considered for those boundary conditions in the

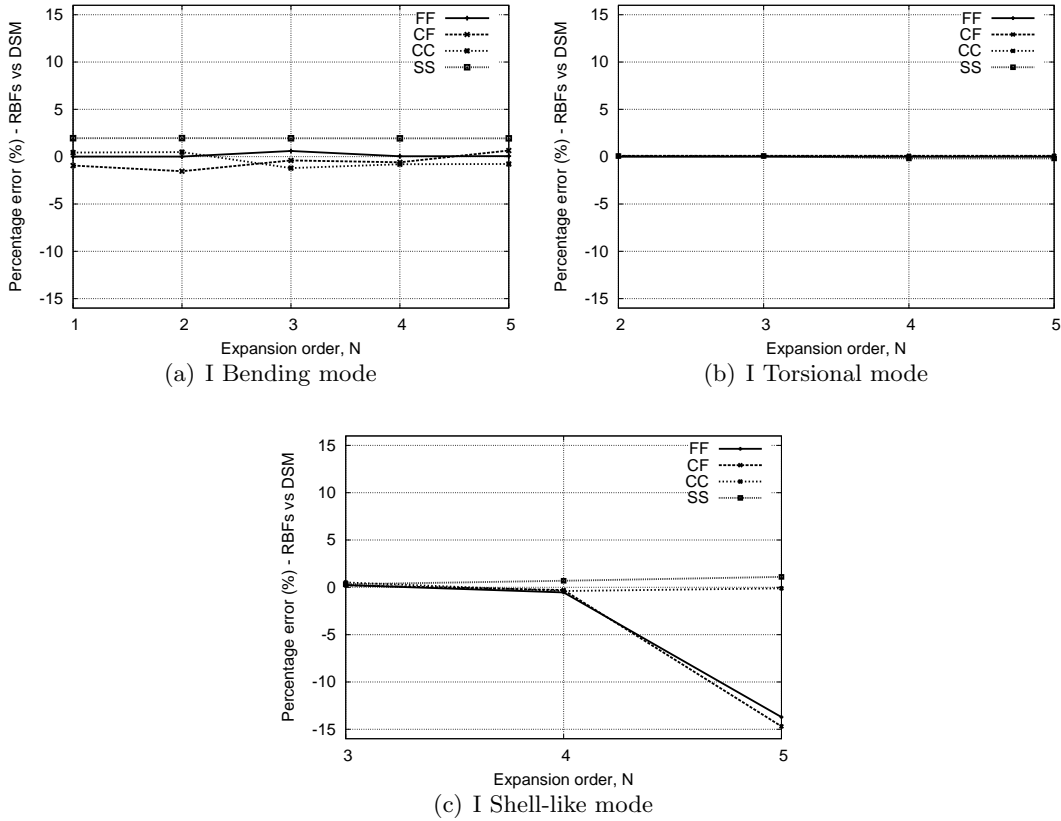


Figure 9.5: Percentage error between the RBFs and exact DSM solutions for various expansion orders and boundary conditions; Thin-walled cylinder

case of RBFs.

Figure 9.6 shows the important modes of the cylinder for CC boundary condition by the fifth-order ($N = 5$) TE DSM model. The following comments arise:

- Only the flexural modes are provided by the classical beam theories.
- Torsional modes are correctly detected by the linear TE ($N = 1$) model in the case of axisymmetric structures.
- 1D higher-order model are necessary to detect shell-like modes as evident from the 2D FEM solutions provided by MSC Nastran.
- Instabilities may occur in the case of RBFs when thin-walled structures are considered.

9.1.3 Four- and two-layer beams

The capabilities of the proposed methodology when applied to laminated composite structures is further verified. The beam has a square cross-section and a length-to-side ratio, L/h , equal to 15 with $h = 25.4$ mm. The material adopted is a AS4/3501-6 graphite/epoxy composite in accordance with [54].

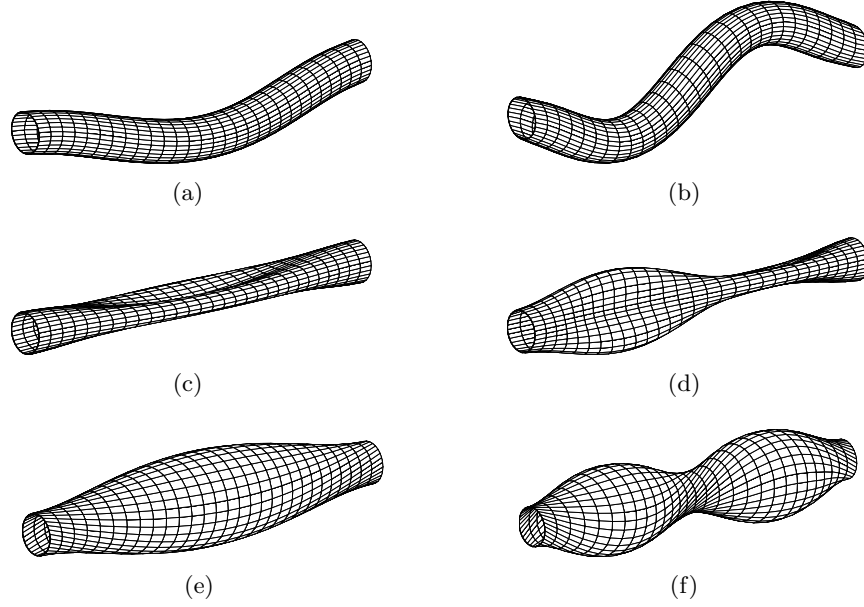


Figure 9.6: First flexural (a), second flexural (b), first shell-like (c), second shell-like (d), first torsional (e) and second torsional (f) modes for a CC thin-walled cylinder; DSM $N = 5$ TE model

	DSM				RBFs				References	
	TBM	$N = 2$	$N = 4$	$N = 6$	TBM	$N = 2$	$N = 4$	$N = 6$	Ref. [56]	Ref. [53]
Mode 1 ^a	1.993	2.112	1.987	1.962	1.993	2.123	1.995	1.976	1.845	1.981
Mode 2 ^b	2.067	2.144	2.084	2.045	2.067	2.153	2.103	2.071	-*	-
Mode 3 ^a	5.261	5.577	5.188	5.134	5.261	5.579	5.206	5.164	4.987	5.217
Mode 4 ^b	5.641	5.852	5.687	5.579	5.641	5.878	5.738	5.647	-	-
Mode 5 ^c	-*	10.627	9.241	9.131	-	10.633	9.265	9.169	-	-
Mode 6 ^a	9.793	10.342	9.553	9.474	9.793	10.344	9.579	9.516	9.539	9.691
Mode 7 ^b	10.898	11.319	10.990	10.782	10.898	11.369	11.089	10.920	-	-
Mode 8 ^a	15.278	16.088	14.756	14.663	15.278	16.088	14.785	14.719	13.474	10.535
Mode 9 ^d	15.174	15.472	15.307	15.092	15.174	15.496	15.370	15.177	15.292	15.098

^a: Flexural on plane yz ; ^b: Flexural on plane xy ; ^c: Torsional mode; ^d: Axial/shear (plane xz) mode

*: Mode not provided by the theory

Table 9.4: Non-dimensional natural frequencies, $\omega^* = \frac{\omega L^2}{b} \sqrt{\frac{\rho}{E_{11}}}$, of a CC [+45/ - 45/ + 45/ - 45] antisymmetric angle-ply beam

Table 9.4 shows the main non-dimensional natural periods ($\omega^* = \frac{\omega L^2}{b} \sqrt{\frac{\rho}{E_{11}}}$) for a [+45/ - 45/ + 45/ - 45] antisymmetric angle-ply lamination scheme in the case of clamped-clamped (CC) boundary conditions. The results by classical and refined beam theories from the present CUF method by both DSM and RBFs are compared to those from the literature. It is shown that higher-order effects can be detected if sufficiently enriched kinematics are considered. In the case of RBFs solutions, a uniform grid of 40 centers and a shape parameter $c = 4 \times 10^{-3}$ were used. It is clear that torsional and coupled axial/shear modes are foreseen by the presents models if a sufficiently higher-order kinematics is adopted.

To show the capability of the present models to deal with arbitrary laminations, Fig. 9.7 shows the effect of increasing the angle of orientation θ on the natural periods of two

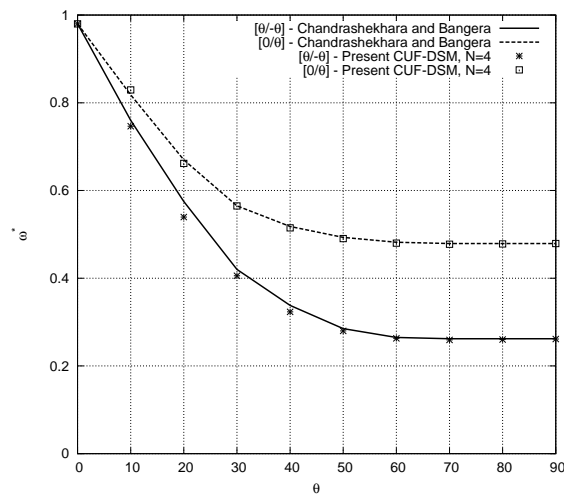


Figure 9.7: Effect of ply orientation angle on first flexural natural frequencies of two-layer CF beams; DSM $N = 4$ TE model versus [53]

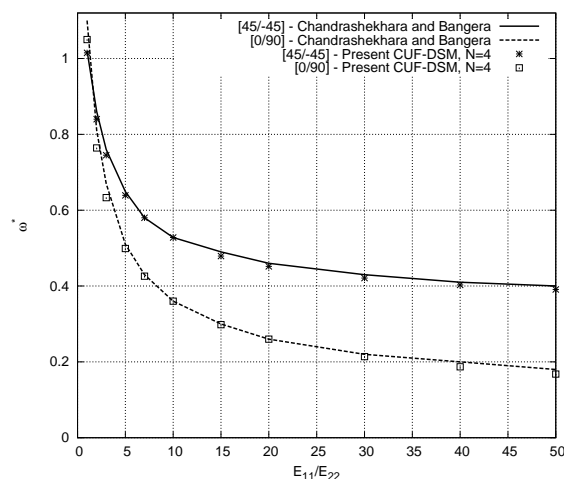


Figure 9.8: Effect of material anisotropy on first flexural natural frequencies of angle-ply and cross-ply CF beams; DSM $N = 4$ TE model versus [53]

lamination schemes $[\theta/ - \theta]$ and $[0/\theta]$. The present fourth-order ($N = 4$) CUF-DSM model is compared to the solution available from [53], where a 1D FE model based on a higher-order shear deformation theory was used.

Finally, Fig. 9.8 shows the effect of material anisotropy on fundamental frequencies. Also for this analysis case, the results by the present $N = 4$ TE-DSM model are validated with those from the literature. It is noted that in Fig. 9.8 the value of E_1 is varied, whereas the other elastic parameters are kept constant. It is clear that the angle-ply configuration tends to lower the frequencies more rapidly than the cross-ply beam.

9.2 Analysis of thin-walled and composite structures by ML

The accuracy and efficiency of Multi-Line (ML) models presented in Chapter 5 are discussed in this section. The results are retrieved from [36, 37], where static analyses of

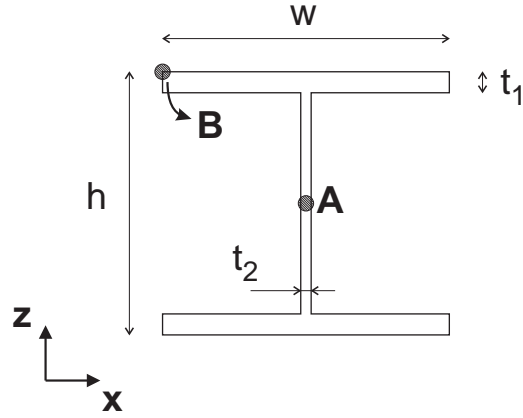


Figure 9.9: I-section beam geometry and verification points

thin-walled and composite laminated beams were discussed.

9.2.1 I-section beam

A cantilever beam with a I-shaped cross-section such as the one shown in Fig. 9.9 is considered. It is assumed that the beam has a height $h = 100$ mm and a width $w = 96$ mm. The length to height ratio, L/h , is 10. The thickness of the flanges is $t_1 = 8$ mm, whereas the thickness of the web is $t_2 = 5$ mm. The material data are: elastic modulus $E = 200$ GPa and Poisson ratio, ν , equal to 0.29. A vertical force $F_z = -2000$ N is applied at point B (see Fig. 9.9) at the free end of the beam.

Table 9.5 shows the vertical displacements, u_z , at the tip of the beam, at points A and B, which are shown in Fig. 9.9. The number of the degrees of freedom (DOFs) is also given for each model in Table 9.5. The results are compared with 3D (Solid) and 2D (Shell) FEM solutions obtained using the commercial code MSC Nastran. The Solid model was constructed by using 8-node CHEXA elements having approximately a unitary aspect ratio. On the other hand, the Shell model was obtained with 4-node CQUAD4 shell elements. The analytical result achieved through Euler-Bernoulli beam theory is also given for comparison purposes, $u_{z_b} = \frac{F_z L^3}{3EI}$, where I is the cross-section moment of inertia. The results by classical and refined CUF TE single-line models are shown in rows 6 to 15, where up to eight-order ($N = 8$) beam models are considered. The last rows of Table 9.5 give the results by the Multi-Line (ML) models of the I-section beam.

Figure 9.10 shows the difference between the single-line and the present ML models. In the single-line approach, 10 cubic Lagrange beam elements are placed on one beam axis. Conversely, in the ML models of the I-shaped cross-section structure, three beam axes are used. Specifically, one beam-line is placed on the web and one beam-line is placed on each flange. 10 cubic Lagrange beam elements are used for each beam-line. Compatibility of displacements is subsequently imposed at three points per beam node on the interfaces between flanges and web through Lagrange multipliers (see Chapter 5). Unlike the problems discussed in [42] where the number of connecting points was chosen on the basis of a convergence study, for the present ML models it was found that the convergence of the solution is guaranteed with a few connecting points. For this reason the attention is not focused on this problem in the present example. The ML models of the I-section beam are here referred to as ML_{N_f, N_w} , where N_f is the expansion order of the beam elements placed on beam-lines of the flanges and N_w is the expansion order of the beam elements

	$-u_{z_A}$ (mm)	$-u_{z_B}$ (mm)	DOFs	
$-u_{z_b} = \frac{F_z L^3}{3EI} = 0.951, \text{ mm}$				
MSC Nastran models				
Solid	0.956	2.316	355800	
Shell	1.006	(2.437)	61000	
Classical and refined single-line models				
EBBM	0.951	0.951	93	
TBM	0.964	0.964	155	
$N = 1$	0.964	0.978	279	
$N = 2$	0.956	0.978	558	
$N = 3$	0.989	1.018	930	
$N = 4$	0.989	1.287	1395	
$N = 5$	0.993	1.481	1953	
$N = 6$	0.992	1.462	2604	
$N = 7$	0.997	1.560	3348	
$N = 8$	0.997	1.851	4185	
Multi-line models, ML_{N_f, N_w}				
N_f	N_w			
1	1	1.016	1.016	837
2	1	0.990	1.028	1116
2	2	0.951	1.940	1674
3	1	0.994	1.104	1488
3	2	0.950	1.984	2046
3	3	0.952	2.186	2790
4	1	0.983	1.201	1953
4	2	0.951	2.008	2511
4	3	0.954	2.197	3255
4	4	0.952	2.230	4185

Table 9.5: Vertical displacement at points A and B on the free end of the cantilever I-section beam

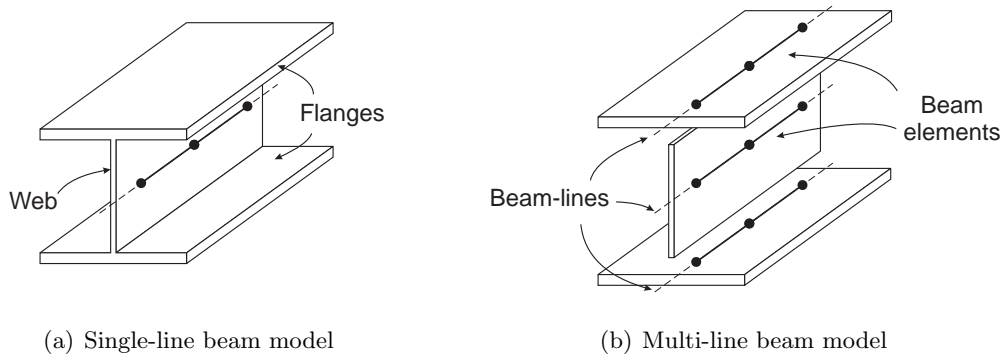


Figure 9.10: Single- and multi-line approaches to the analysis of the I-section beam

placed on the beam-line of the web.

Figure 9.11 shows the deformation of the free end of the beam. ML models are compared to the eight-order single-line ($N = 8$) TE model and to the Solid model. Finally,

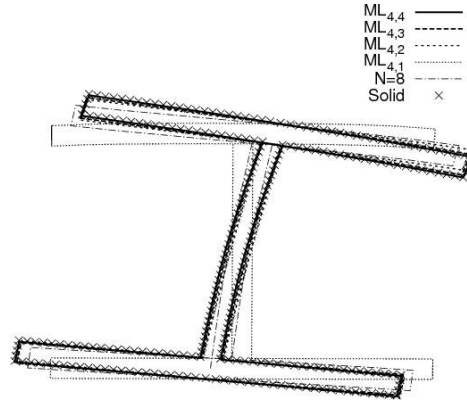


Figure 9.11: Tip cross-section deformation of the I-section beam

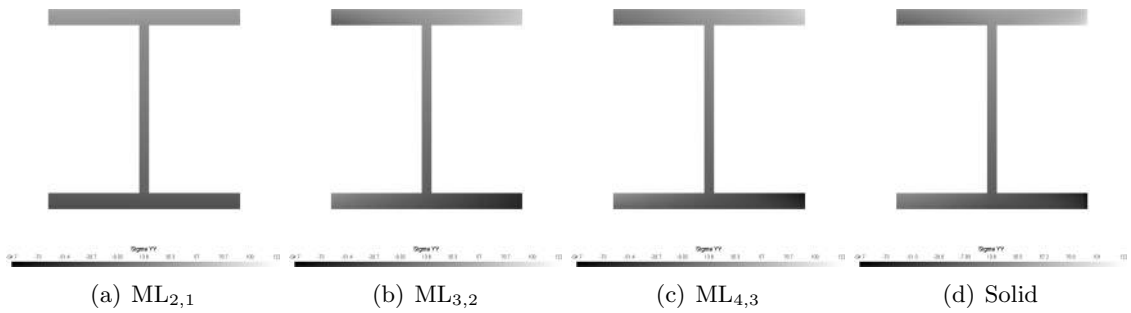


Figure 9.12: Normal stress distribution, σ_{yy} , at the clamped end of the I-section beam

Fig. 9.12 shows the distribution of axial stresses, σ_{yy} , at the clamped end for different structural models. Based on these results the following comments can be made:

- Classical and lower-order single-line models cannot detect the cross-sectional distortions due to the bending-torsional load according to MSC Nastran results.
- Lower-order elements can be effective when used in a ML approach. In fact, third-order (ML_{3,3}) and fourth-order (ML_{4,2}, ML_{4,3}, and ML_{4,4}) ML models match Shell and Solid solutions both in terms of displacement and stress fields.
- The number of the degrees of freedom of ML models is extremely reduced if compared to MSC Nastran and single-line refined models.

9.2.2 Symmetric laminated beam

The analysis of a symmetric cross-ply $[0^\circ/90^\circ/0^\circ]$ laminated cantilever beam is carried out next. The beam is considered to be rectangular with width b and height h . The length-to-height ratio is $L/h = 4$. The three layers have the same thickness. The non-dimensional properties of the adopted orthotropic material are

$$E_1/E_2 = 25 \quad G_{12}/G_{22} = 2.5 \quad \nu_{12} = \nu_{22} = 0.33$$

The ML scheme adopted is depicted in Fig. 9.13, together with the loading condition.

The ML models addressed make use of three beam-lines. Two ML configurations are considered: (1) in the first case a second-order ($N = 2$) expansion is used in the three layers; (2) in the second case a third-order ($N = 3$) expansion is used in the top/bottom

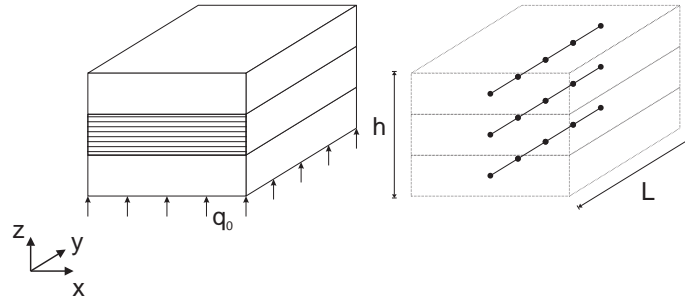


Figure 9.13: Symmetric laminated [0/90/0] beam and related ML model

Model	u_z^*	$-\sigma_{yy}^*$	$-\sigma_{zz}^*$	DOFs
Multi-line models, ML				
ML 2/2/2	17.69	32.72	1.01	1188
ML 3/2/3	17.83	25.69	1.03	1716
MSC Nastran model [29]				
Solid	17.98	30.58	1.03	103920
Classical and higher-order ESL models [29]				
$N = 6$ with ZZ	17.84	27.36	1.03	1914
$N = 6$	17.14	25.29	0.99	1848
$N = 3$ with ZZ	17.83	31.17	1.02	726
$N = 3$	16.76	28.38	1.04	660
TBM	14.02	36.52	0.00	110
EBBM	6.22	36.52	0.00	66

 Table 9.6: Non-dimensional displacement at the tip and stress components, symmetric cross-ply beam; σ_{yy}^* at $(b, 0, 0.867h)$ and σ_{zz}^* at $(b, L/2, 0)$

layers, whereas a parabolic distribution on the cross-section is assumed in the central layer. ML models of the symmetric laminated beam are referred to as ML $\alpha/\beta/\gamma$, where α is the expansion order of the beam discretizing the bottom layer, β is the expansion order of the central layer, and γ is the expansion order of the top layer.

The results are shown in Table 9.6, where the non-dimensional vertical displacement at the tip is given together with stress components. The results are non-dimensionalized as follows:

$$u_z^* = 100 \frac{bh^3 E_2}{q_0 L^4} u_z, \quad \sigma_{ij}^* = \frac{\sigma_{ij}}{q_0}, \quad \text{with } i, j = x, y, z \quad (9.1)$$

where L is the length of the beam, whereas b and h are the dimensions of the rectangular cross-section. q_0 is the intensity of the load uniformly distributed over the lower face of the beam. In Table 9.6 the values of σ_{yy}^* at $(b, 0, 0.867h)$ and σ_{zz}^* at $(b, L/2, 0)$ are shown (the verification points are measured from the bottom left corner). The last column of Table 9.6 gives the number of the DOFs for each model considered. The results by ML models are compared to classical and ESL (Equivalent Single Layer, i.e. single-line TE) theories from [29] and to a solid FE model by MSC Nastran. For both ML and ESL beam models, seven four-node Lagrange 1D elements were used along the beam axes.

ML analysis shows some convenience with respect to ESL, even though they are improved through Zig-Zag (ZZ) Murakami functions. The stress distributions shown in Fig. 9.14 confirm this conclusion, even if it is evident from the figure that ESL models

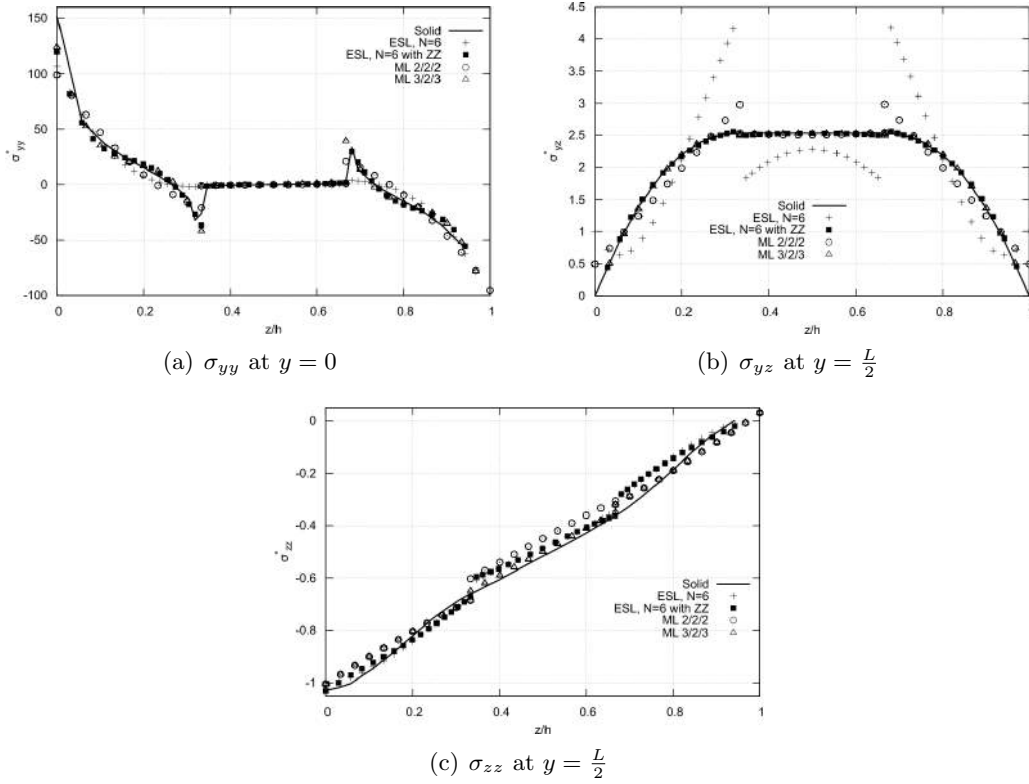


Figure 9.14: Distribution of axial, σ_{yy}^* , and transverse, σ_{yz}^* and σ_{zz}^* , stresses for the symmetric laminated beam

without through-the-thickness ZZ functions are not able to correctly detect transverse stress trends. On the other hand, both ESL with ZZ and ML models are able to deal with solid-like analysis with very low computational costs.

9.3 Analysis of aircraft structures by CW

The enhanced capabilities of CUF models when applied to aircraft structures are discussed in this section. The attention is mainly focused on the Component-Wise (CW) 1D models (see Chapter 5), which are able to reproduce 3D-like accuracy with very low computational costs. Both static and free vibration analyses are proposed, ranging from simple wing box to complex wing structures, including composites. Unless differently specified, all the CUF models have been discretized by means of FEM and by using 10 four-node (cubic) Lagrange 1D elements that provided convergence for most of the cases considered. For more results about aerospace structures by CW the reader is referred to [39, 40, 28, 46, 124, 45].

9.3.1 Static analysis of a trapezoidal wing box

The following analysis case is carried out on the three-bay wing box for which analytical solutions were given in Rivello's book [134]. The considered structure is shown in Fig. 9.15a, whereas Figs. 9.15b and c show its variations. These examples highlight the capability of the present advanced 1D models to accurately describe the effects due to ribs and open sections. The structures consist of three wing boxes each with a length, l , equal to 0.5 m. The cross-section is a trapezium with height $b = 1$ m. The two webs of the spars

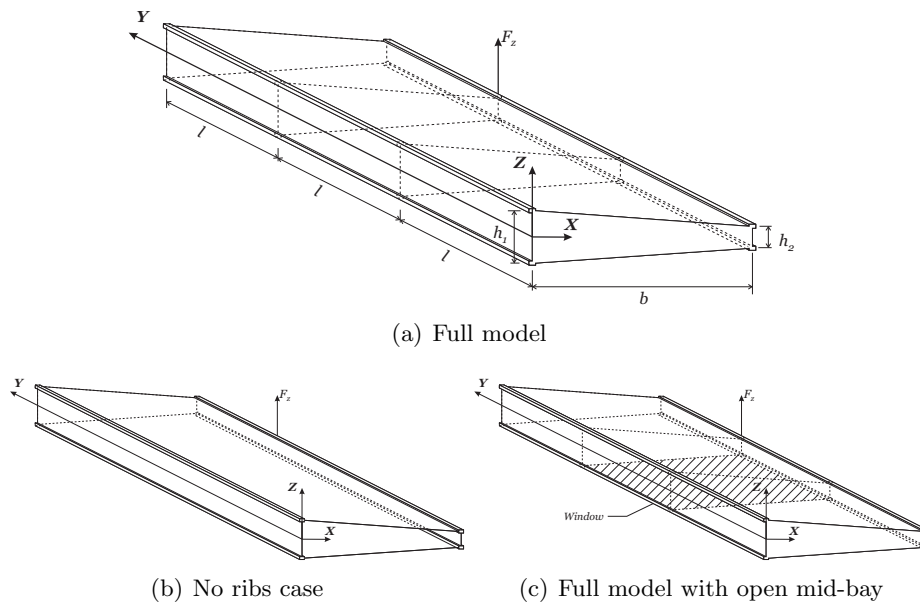


Figure 9.15: Different structural configurations of the three-bay wing box

	Full model		No ribs case		Open mid-bay case	
	$u_z \times 10^2$ (m)	DOFs	$u_z \times 10^2$ (m)	DOFs	$u_z \times 10^2$ (m)	DOFs
	MSC Nastran					
Solid/Shell	1.412	100026	3.051	89400	1.963	89621
	Classical beam theories					
EBBM	0.464	495	0.464	495	0.464	495
TBM	0.477	495	0.477	495	0.477	495
	TE-based refined models					
$N = 3$	0.793	1650	0.794	1650	0.873	1650
$N = 5$	1.108	3465	1.203	3465	1.500	3465
$N = 7$	1.251	5940	2.158	5940	1.745	5940
$N = 9$	1.325	9075	2.649	9075	1.836	9075
	LE-based refined models					
CW	1.397	10750	2.981	10560	1.919	10446

 Table 9.7: Displacement values, u_z , at the loaded point and number of DOFs for the considered structural configurations of the three-bay wing box

have a thickness of 1.6×10^{-3} m, whereas $h_1 = 0.16$ m and $h_2 = 0.08$ m. The top and the bottom panels have a thickness of 0.8×10^{-3} m, as well as the ribs. The area of each stringer is $A_s = 8 \times 10^{-4}$ m². The wing is completely made of an aluminium alloy 2024, having $G/E = 0.4$. The cross-section in $y = 0$ is clamped and a point load, $F_z = 20$ kN, is applied at $(b, 2 \times l, \frac{h_2}{2})$.

Table 9.7 shows the vertical displacement values u_z and the computational costs for each model. Results related to the CUF models are validated by an MSC Nastran model built both with solid (for stringers) and shell (for panels) FE elements and it is referred to as “Solid/Shell”. The CW models were obtained by using both L4 and L9 elements on the beam cross-section (see [39]).

Figures 9.16, 9.17 and 9.18 show the spanwise variation of the axial and the shear stress components for the three different configurations. Results by the present CUF models and

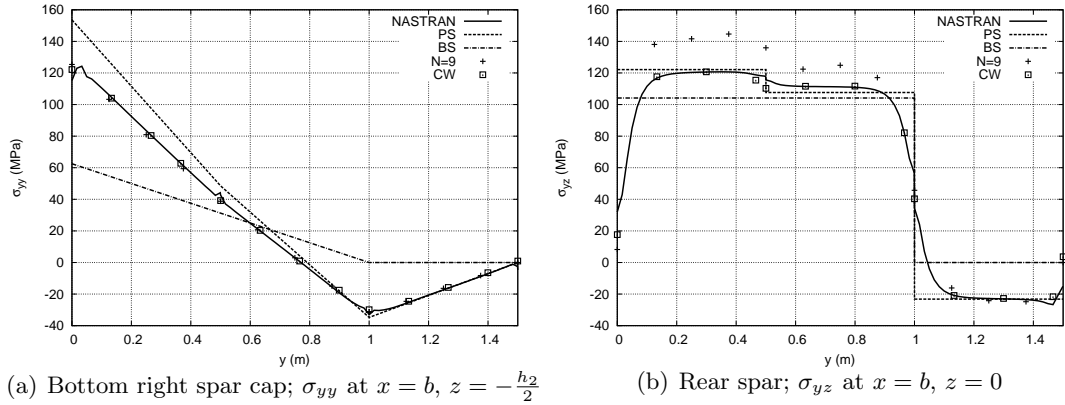


Figure 9.16: Stress components distribution along the wing span; Comparison of analytical, MSC Nastran and CUF models of the full model of the three-bay wing box

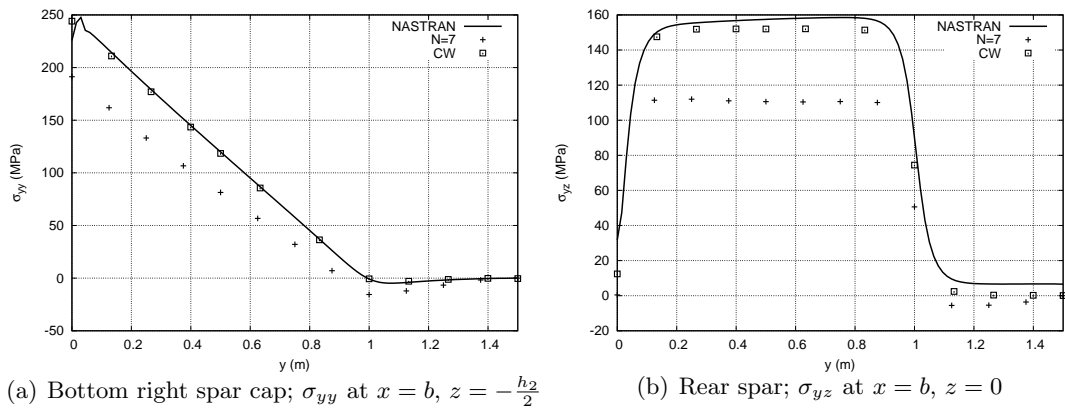


Figure 9.17: Stress components distribution along the wing span; Comparison of MSC Nastran and CUF models of the three-bay wing box with no ribs

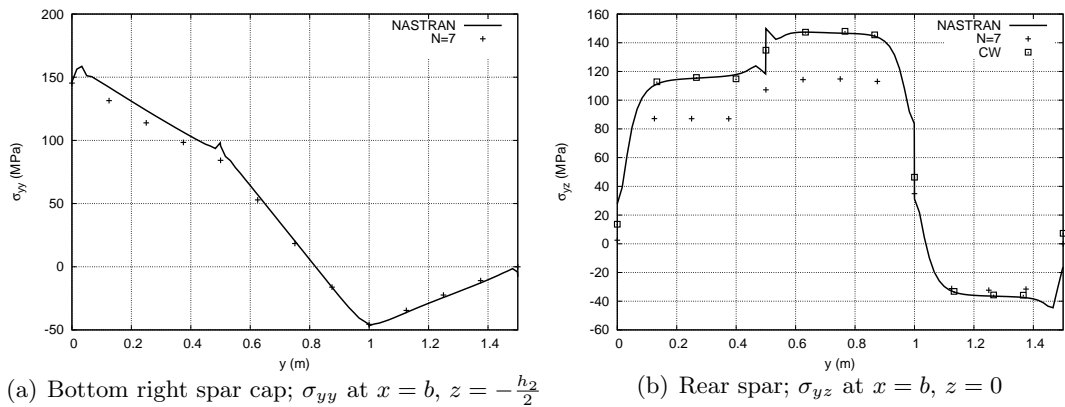


Figure 9.18: Stress components distribution along the wing span; Comparison of MSC Nastran and CUF models of the three-bay wing box with open mid-bay

Model	Full model		No ribs case		Open mid-bay case	
	σ_{yy} (MPa)	σ_{yz} (MPa)	σ_{yy} (MPa)	σ_{yz} (MPa)	σ_{yy} (MPa)	σ_{yz} (MPa)
Solid/Shell	80.598	120.730	178.147	155.368	123.841	115.351
CW LE	80.404	120.603	177.018	151.876	118.684	115.810

Table 9.8: Stress components, σ_{yy} at $(b, \frac{l}{2}, -\frac{h_2}{2})$ and σ_{yz} at $(b, \frac{l}{2}, 0)$, of the different structural configurations of the three-bay wing box

MSC Nastran are compared to analytical solutions, which are retrieved from [134]. Those analytical, classical solutions are referred to as BS (Beam Semimonocoque) and PS (Pure Semimonocoque). In PS, stringers are considered as concentrated areas carrying only axial stresses, while webs and panels carry only shearing stresses. In BS, beam theories are also applied to PS assumptions (see [24, 39]); hence, structural redundancies can be generally eliminated and the equilibrium can be determined by only using the equations of the statics. In fact, the structure considered has three redundancies and the equilibrium equations are not sufficient for PS. As in [24], the principle of virtual displacements is here used to “correct” the BS solution. For the complete resolution of the trapezoidal wing box the reader is referred to [134, Chap. 11 p. 301].

Table 9.8 finally reports the numerical values of the stress components of both CW and comparison models. The following remarks can be made:

- CW models correctly predict ribs and local effects, as they match the results obtained with solid/shell models.
- Higher than sixth-order TE models are required to correctly predict the cross-section deformability.
- The PS method is quite accurate in the description of the full configuration of the three-bay wing box. Conversely, the BS method is not suitable as the structure is statically indeterminate.

9.3.2 Free vibrations of a complete NACA wing

The free vibration analysis of a cantilever, complete aircraft wing is further discussed. The cross-section of the wing is shown in Fig. 9.19. The NACA 2415 airfoil was used and two spar webs and four spar caps were added. The airfoil has the chord, c , equal to 1 m. The length, L , along the span direction is equal to 6 m. The thickness of each panel is 3×10^{-3} m, whereas the thickness of the spar webs is 5×10^{-3} m. The dimensions of the flanges of the longerons can be found in [40]. The whole structure is made of an isotropic material. The material data are: the Young modulus, E , is equal to 75 GPa; the Poisson ratio, ν , is 0.33; the density is $\rho = 2700 \text{ kg/m}^3$. For the present wing structure, two different configurations have been considered. *Configuration A* has no transverse stiffening members. In *Configuration B* the wing is divided into three equal bays, each separated by a rib with a thickness of 6×10^{-3} m.

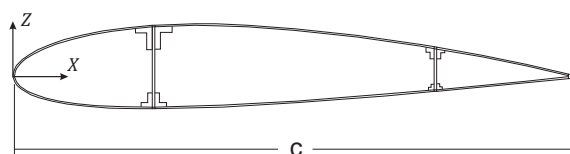


Figure 9.19: Cross-section of the wing

Table 9.9 shows the main modal frequencies of both structural configurations of the wing. In this table, the results obtained through the CUF models are compared to those from classical beam theories and to those from 3D MSC Nastran (Solid) models. In the last two rows of Table 9.9, the frequencies of the first two shell-like modes are quoted.

	EBBM	TBM	$N = 1$	$N = 2$	$N = 3$	CW	Solid
<i>Configuration A</i>							
DOFs	93	155	279	558	930	21312	186921
Global modes							
I Bending ^{x*}	4.22	4.22	4.22	4.29	4.26	4.23	4.21
I Bending ^z	22.10	21.82	21.82	21.95	21.87	21.76	21.69
II Bending ^x	26.44	26.36	26.36	26.66	26.25	25.15	24.78
I Torsional	-	-	132.93	50.27	48.46	31.14	29.18
III Bending ^x	73.91	73.35	73.35	73.99	71.64	59.26	56.12
II Bending ^z	134.66	124.68	124.68	124.99	122.77	118.39	118.00
Local modes							
I Shell-like	-	-	-	-	-	86.36	75.13
II Shell-like	-	-	-	-	-	88.94	73.85
<i>Configuration B</i>							
DOFs	84	140	252	504	840	23976	171321
Global modes							
I Bending ^{x*}	4.12	4.12	4.12	4.19	4.17	4.14	4.12
I Bending ^z	21.56	21.30	21.30	21.50	21.42	21.28	21.22
II Bending ^x	25.71	25.63	25.63	26.00	25.61	25.00	24.92
I Torsional	-	-	131.24	49.57	47.48	39.45	39.22
III Bending ^x	71.44	70.90	70.90	71.80	69.49	64.84	63.88
II Bending ^z	131.11	121.49	121.49	122.23	120.06	115.76	115.40
Local modes							
I Shell-like	-	-	-	-	-	85.61	75.01
II Shell-like	-	-	-	-	-	91.54	78.61

* Bending^ξ: bending mode about the ξ-axis

Table 9.9: Global and local modal frequencies (Hz) of the complete NACA aircraft wing

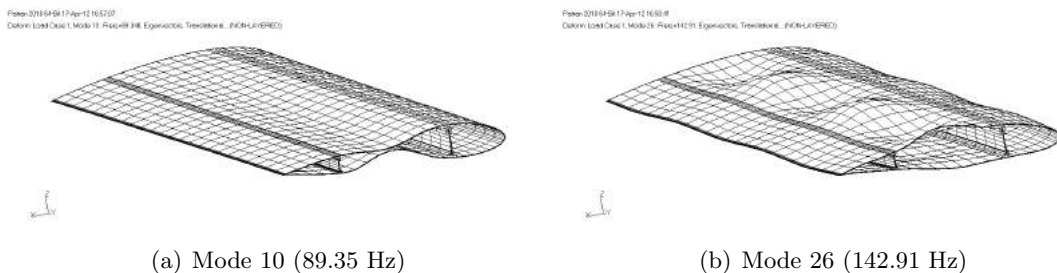


Figure 9.20: Shell-like modes of the wing (*Configuration A*) evaluated with the CW model

To deal with complex structures, such as the one considered in this section, the CW models were included into the commercial software MSC Nastran, which was used to solve

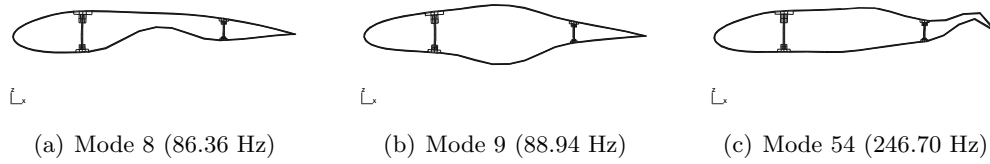


Figure 9.21: Shell-like modes of the wing (*Configuration A*) evaluated with the CW model; Mid-span cross-section

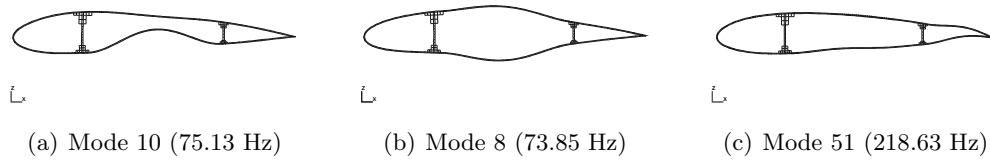


Figure 9.22: Shell-like modes of the wing (*Configuration A*) evaluated with the Solid model; Mid-span cross-section

the eigenvalue problem through DMAP alters, and MSC Patran was used for the post-processing of the CW model of the wing. Two shell-like modes evaluated by means of the CW model are shown in Fig. 9.20 for *Configuration A*.

To further underline the component-wise capability of the CW approach, in Figs. 9.21 and 9.22 the deformed mid-span cross-sections for different shell-like modes are plotted. Moreover, the enhanced capabilities of the present methodology is definitely assessed by the MAC matrix shown in Fig. 9.23, in which the CW eigenvectors are compared to those from the 3D model. The MAC is, in fact, defined as a scalar representing the degree of consistency (linearity) between one modal and another reference modal vector (see [3]) as follows:

$$MAC_{ij} = \frac{|\{\phi_{A_i}\}^T \{\phi_{B_j}\}|^2}{\{\phi_{A_i}\}^T \{\phi_{A_i}\} \{\phi_{B_j}\} \{\phi_{B_j}\}^T} \quad (9.2)$$

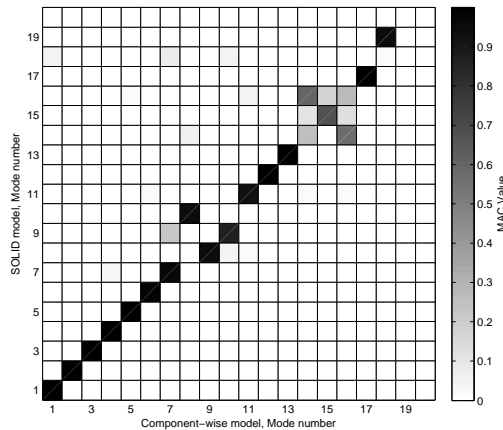


Figure 9.23: MAC values between the CW models and the Solid model; NACA aircraft wing (*Configuration A*)

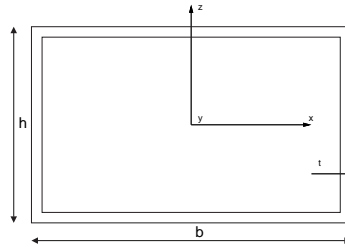


Figure 9.24: Cross-section of the laminated box beam

where $\{\phi_{A_i}\}$ is the i^{th} eigenvector of model A , while $\{\phi_{B_j}\}$ is the j^{th} eigenvector of model B . The modal assurance criterion takes on values from zero (representing no consistent correspondence), to one (representing a consistent correspondence). The following considerations hold:

- The bending modes of the wing are correctly detected by both the lower-order and higher-order TE models.
- At least a cubic expansion on the displacement field (TE, $N = 3$) is necessary to correctly detect the torsional modes.
- The CW models match the 3D solutions; in fact, shell-like modes can be obtained by means of CW beam elements.
- The computational effort of a higher-order beam model is significantly lower than the ones requested by solid models.

9.3.3 Free vibrations of composite wing boxes

In this section a hollow rectangular cross-section laminated box beam is considered for verification. Clamped-free boundary conditions are addressed. The same structure was used for experimental [52] and analytical [5] investigations in previous works. The cross-section geometry is shown in Fig. 9.24. The dimensions of the beam are as follows: length $L = 844.55$ mm, height $h = 13.6$ mm, width $b = 24.2$ mm, and thickness $t = 0.762$ mm. The box beam is made of six layers with the following orthotropic material properties: $E_1 = 141.96$ GPa, $E_2 = E_3 = 9.79$ GPa, $\nu_{12} = \nu_{13} = 0.42$, $\nu_{23} = 0.5$, $G_{12} = G_{13} = 6.0$ GPa, $G_{23} = 4.83$ GPa, and $\rho = 1445$ kg/m³. The six layers have the same thickness. Different lamination schemes are considered for the box beam under consideration. Both CAS (Circumferentially Asymmetric Stiffness) and CUS (Circumferentially Uniform Stiffness) stacking sequences are addressed and they are detailed in Table 9.10.

Lay-up	Flanges		Webs	
	Top	Bottom	Left	Right
CAS2	[30] ₆	[30] ₆	[30/ - 30] ₃	[30/ - 30] ₃
CAS3	[45] ₆	[45] ₆	[45/ - 45] ₃	[45/ - 45] ₃
CUS1	[15] ₆	[-15] ₆	[15] ₆	[-15] ₆
CUS2	[0/30] ₃	[0/ - 30] ₃	[0/30] ₃	[0/ - 30] ₃
CUS3	[0/45] ₃	[0/ - 45] ₃	[0/45] ₃	[0/ - 45] ₃

Table 9.10: Various stacking sequences of the box beam

Lay-up	Mode	TE				Exp. [52]	Analytical [5]	Shell [87]
		CW 24L9	TBM	N=3	N=7			
CAS2	1 ^a	20.06	20.96	21.39	20.60	20.96	19.92	19.73
	2 ^b	38.21	41.76	40.51	39.42	38.06	—*	37.53
	3 ^a	125.44	131.01	133.76	128.71	128.36	124.73	123.32
CAS3	1 ^a	14.75	15.00	15.24	14.69	16.67	14.69	14.58
	2 ^b	25.41	26.38	26.16	25.44	29.48	—	25.01
	3 ^a	92.35	93.88	95.44	94.83	96.15	92.02	91.23
CUS1	1 ^a	29.51	32.36	30.29	29.19	28.66	28.67	28.37
CUS2	1 ^a	34.69	35.09	34.91	34.61	30.66	34.23	34.29
CUS3	1 ^a	33.03	33.11	33.10	33.01	30.00	32.75	32.35

^a: Flexural on plane yz , ^b: Flexural on plane xy , *: Not provided

Table 9.11: Natural frequencies (Hz) for different stacking sequences of the laminated box beam.

The values of the natural frequencies obtained from these box beam configurations are listed in Table 9.11, where the results from the present LE/CW and TE models are compared to those from the literature. In particular, TBM, the third- and the seventh-order TE models as well as a LE model made with 24L9 elements are compared to experimental data [52], analytical solutions [5] and a 2D FE model (Shell) by ANSYS [87]. Regarding the 24L9 model, it was obtained by using one single L9 element per layer on each flange and web. Both TE and CW models were discretized with 7 cubic ($p = 3$) Lagrange 1D elements along the axis for this analysis case.

The following comments can be made:

- Classical TBM and lower-order TE models overestimate the natural frequencies of the proposed composite box beam.
- The present beam formulations can deal with both CAS and CUS lay-up box beam configurations. The results by the present CW and higher-order TE models are, in fact, in good agreement with those from analytical solutions and experimental data.
- Unlike the theory by Armanios and Badir [5], the present beam models can deal with bending modes in both yz - and xy -planes.
- Both CW and the seventh-order (N=7) TE models can detect the solution from a 2D shell FE model.

9.4 Application of CW models to civil engineering structures

During the research activities proposed in this thesis, the enhanced capabilities of the CW methodology has been widely tested over a large range of structures, including civil engineering structures. CW models for this kind of structures have been broadly discussed in [43, 41]. In this section, multi-floor buildings are discussed as an example.

A single-floor flat (*Configuration A*, Fig. 9.25a) is considered first. This structure is composed by one floor and four columns clamped to the ground. The main dimensions are given in Fig. 9.25a and Fig. 9.26, where the cross-section of the floor is shown. As it is clear from Fig. 9.26 the columns and the frames of the floor were made of *Material 1*, whose characteristics are $E = 210$ GPa, $\nu = 0.28$, $\rho = 7850$ kg/m³. The internal part

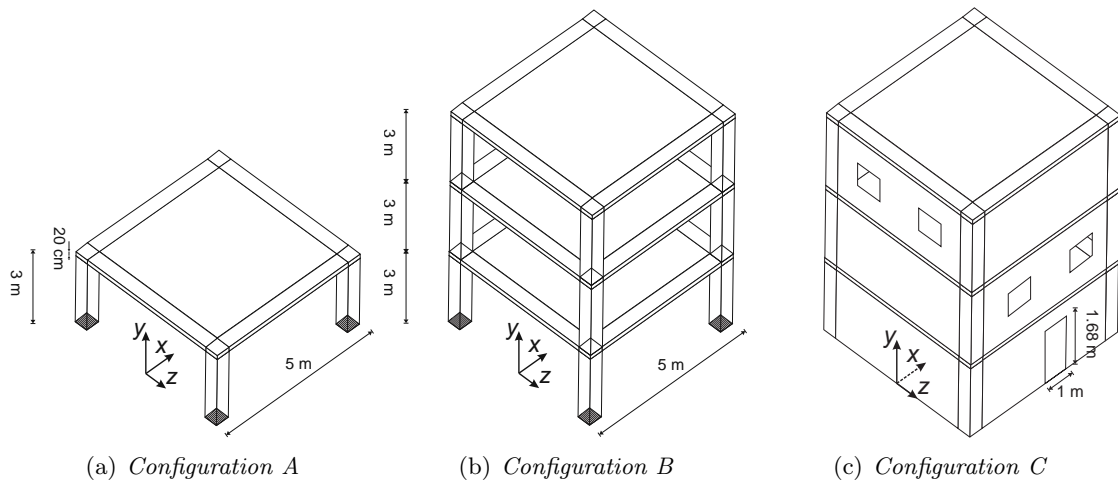


Figure 9.25: Multi-floor buildings

	Configuration A		Configuration B		Configuration C		
	CW	Solid	CW	Solid	CW - coarse	CW - finer	Solid
(DOFs)	(3396)	(181875)	(6300)	(78975)	(11592)	(19548)	(218286)
Mode 1	9.43 ^b	8.79 ^b	3.63 ^b	3.07 ^b	10.18 ^b	9.97 ^b	9.51 ^b
Mode 2	9.43 ^b	8.79 ^b	3.63 ^b	3.07 ^b	10.20 ^b	9.98 ^b	10.04 ^b
Mode 3	13.86 ^t	12.44 ^t	5.32 ^t	4.22 ^t	17.59 ^t	17.26 ^t	13.63 ^t
Mode 4	23.07 ^f	21.67 ^f	10.64 ^b	9.69 ^b	21.72 ^f	13.74 ^f	16.18 ^f
Mode 5	36.80 ^f	36.66 ^f	10.64 ^b	9.69 ^b	25.71 ^f	15.45 ^f	16.61 ^f
Mode 6	36.80 ^f	36.66 ^f	15.60 ^t	13.36 ^t	27.59 ^b	26.67 ^b	24.78 ^b
Mode 7	40.59 ^f	37.59 ^f	16.45 ^b	16.42 ^b	27.70 ^b	26.69 ^b	25.04 ^b
Mode 8	72.41 ^f	77.07 ^f	16.45 ^b	16.42 ^b	32.11 ^f	25.85 ^f	28.48 ^f
Mode 9	115.85 ^c	84.49 ^c	21.16 ^f	20.54 ^f	37.04 ^f	26.88 ^f	28.94 ^f

^b: bending mode; ^t: torsional mode; ^f: floor mode; ^c: column mode

Table 9.12: Natural frequencies (Hz) of multi-floor civil buildings

of the floor was made of *Material 2*, which is characterized by the following properties: $E = 48 \text{ GPa}$, $\nu = 0.28$, $\rho = 1570 \text{ kg/m}^3$. The natural frequencies of this structure are shown in columns 2 and 3 of Table 9.12. The results by the CW model are compared to those by a MSC Nastran solid model, which is referred to as Solid. As far as the CW model is concerned, the single-floor building was modeled as a beam whose axis lays along the coordinate y (see Fig. 9.25a). The cross-section of the floor, which is defined on the xz -plane, was discretized by means of 9 L9 elements (see [41]). One single L9 elements

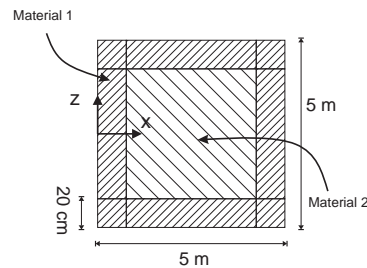


Figure 9.26: Cross-section of the floor

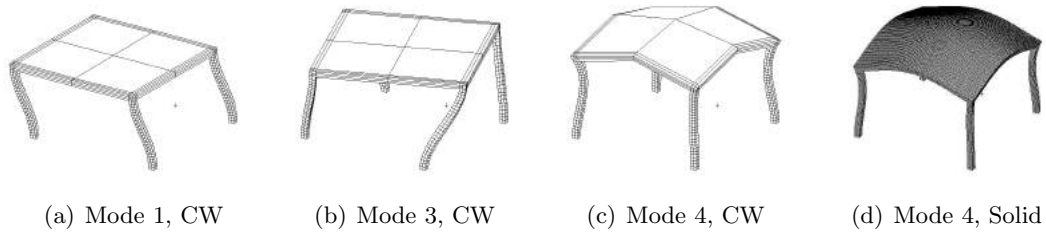


Figure 9.27: Modal shapes of multi-floor buildings; *Configuration A*

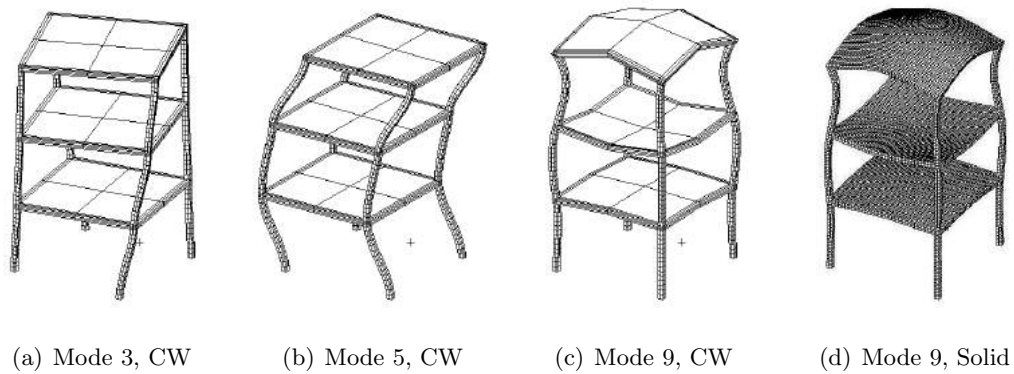


Figure 9.28: Modal shapes of multi-floor buildings; *Configuration B*

was used for each component (i.e. column, frame, etc.). Some representative modes by the CW model and the Solid model of the structure under consideration are shown in Fig. 9.27.

The natural frequencies of the three-floor building (*Configuration B*, Fig. 9.25b) are also given in Table 9.12. The dimensions of the structure are shown in Fig. 9.25b and in Fig. 9.26. The results in Table 9.12 suggest the high efficiency on the present CW models in dealing with both global and local modes. Bending, torsional as well as local modes involving the single components (e.g. floor and columns) are in fact detected in accordance with the solid reference solution by MSC Nastran. This conclusion is also confirmed by

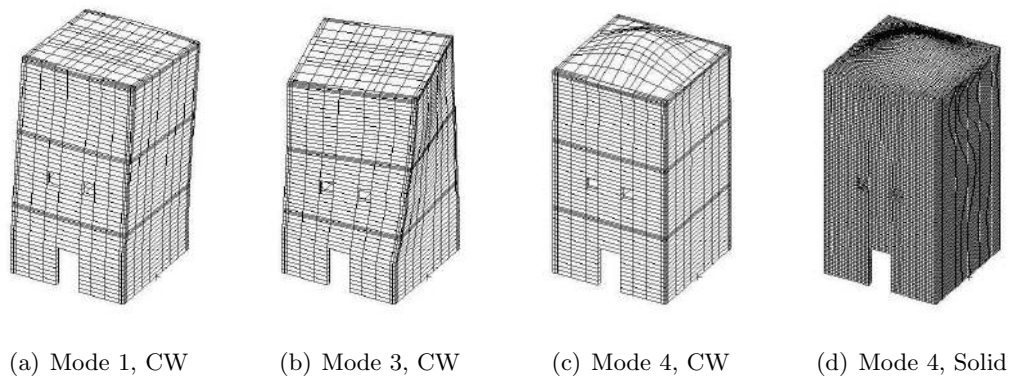


Figure 9.29: Modal shapes of multi-floor buildings; *Configuration C*

Fig. 9.28, where some mode shapes of the three-floor building are shown.

A complete building (*Configuration C*) is considered as the last example and it is shown in Fig. 9.25c. The supporting structure is the same as in the case of the three-floor building (*Configuration B*) considered above, with the difference that walls, windows and a door were added in *Configuration C*. Moreover, in this configuration case, the inner part of the floors (see Fig. 9.26) and walls were made of a material with the following characteristics: $E = 2.1$ GPa, $\nu = 0.28$, $\rho = 1570$ kg/m³. The first nine natural frequencies are given in columns 6, 7 and 8 of Table 9.12 and the results by two different CW models are compared to a solid MSC Nastran model. The two CW models differ in the cross-sectional distribution of the L-elements and more details can be found in [41]. The CW model with a coarse mesh on the cross-section was mainly built with L4 elements. On the contrary, the second CW model had a finer mesh and mainly L9 elements were used. The results in table and the comparison of the modes shown in Fig. 9.29 finally demonstrate the effectiveness of the proposed formulation even when applied to civil engineering structures.

9.5 Flutter analysis of flat-plate wings

Flutter analyses of isotropic and composite structures as discussed in [123] are proposed in this section. Fig. 9.30 shows the notation adopted and the positive directions of sweep and fiber orientation angles. An 8×30 aerodynamic mesh was exploited since this mesh offers good accuracy as shown by Petrolo [128, 127]. The first ten natural modes were used to build the generalized matrices according to Chapter 6.

9.5.1 Isotropic plate wing

An isotropic wing modeled as a flat plate is first considered. The investigated wing model has the following characteristics: $L = 305$ mm, $c = 76$ mm, and thickness $t = 1$ mm. The material is an aluminum alloy with elastic modulus $E = 73.8$ GPa, shear modulus $G = 27.6$ GPa and density $\rho = 2768$ kg/m³. This model was retrieved from [106].

Table 9.13 shows the first three natural frequencies for a swept back configuration ($\Lambda = 30^\circ$). Different beam models have been considered, classical (EBBM and TBM) and higher-order TE (from $N = 1$ to $N = 4$). The results were obtained through the CUF-DSM methodology (see Chapter 3) and they are compared with FEM results from [128]. Bending and torsional modes were detected.

Table 9.14 shows the flutter velocity of the forward swept configuration ($\Lambda = -30^\circ$). Again, the DSM are compared against FEM [128] and the influence of the beam model is evaluated. The results from the classical and the linear ($N = 1$) models are not reported

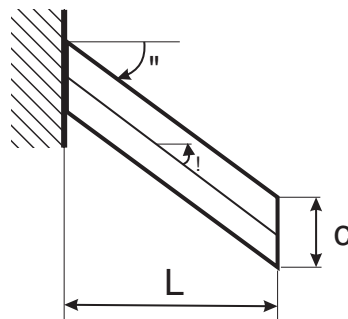


Figure 9.30: Sweep and fiber orientation angles

Model	Method	f_1	f_2	f_3
EBBM	FEM	8.967	56.192	157.335
	DSM	8.968	56.191	157.336
TBM	FEM	8.966	56.189	157.320
	DSM	8.967	56.190	157.320
$N = 1$	FEM	8.966	56.185	157.308
	DSM	8.965	56.186	157.308
$N = 2$	FEM	7.199	44.462	97.939*
	DSM	7.180	44.338	97.863*
$N = 3$	FEM	7.125	43.778	74.316*
	DSM	7.105	43.654	74.412*
$N = 4$	FEM	7.093	43.529	73.296*
	DSM	7.070	43.389	73.370*

*Torsional mode

Table 9.13: Effect of the TE expansion order (N) on the vibration frequencies (Hz) of the isotropic plate wing by means of DSM and FEM; $\Lambda = 30^\circ$

Model	Method	Velocity (m/s)
$N = 2$	FEM	84.206
	DSM	84.086
$N = 3$	FEM	59.202
	DSM	59.366
$N = 4$	FEM	58.050
	DSM	58.188

Table 9.14: Effect of the TE expansion order (N) on the flutter velocities of the isotropic plate wing by means of DSM and FEM; $\Lambda = -30^\circ$

since no flutter conditions were detected by those models. In fact, as it is clear from Table 9.13 and from previous analyses, the classical and the linear ($N = 1$) structural models are not able to foresee torsion and coupling phenomena, which are fundamental in flutter modelling.

The influence of the sweep angle on the flutter velocity is reported in Table 9.15. On the other hand, the influence of the beam models on the flutter condition is shown in Tables 9.16 and 9.17. Finally, Fig. 9.31 shows the damping and the frequency of the first three modes versus the free-stream velocity of the swept back wing. From Fig. 9.31, it is clear that flutter occurs as the damping crosses the zero-line and the first two modes coalesce. The following comments stem from the results that were obtained for the isotropic case:

- The 1D DSM results perfectly match the FEM solutions. Since in [128] the FEM solutions by means of CUF 1D models were successfully compared against those ones by 2D plate models [106], it can be stated that the present 1D DSM models can detect flutter conditions of wings with plate-like accuracy.
- At least a third-order beam model ($N = 3$) is needed to have reliable flutter analyses. This is due to the need of a proper description of torsion and of the bending-torsion coupling to detect flutter conditions.

Λ	Method	Velocity (m/s)
-30°	FEM	58.050
	DSM	58.186
-20°	FEM	51.109
	DSM	51.560
-10°	FEM	46.029
	DSM	46.371
0°	FEM	68.406
	DSM	68.523
10°	FEM	64.262
	DSM	64.506
20°	FEM	60.684
	DSM	59.130
30°	FEM	57.339
	DSM	57.216

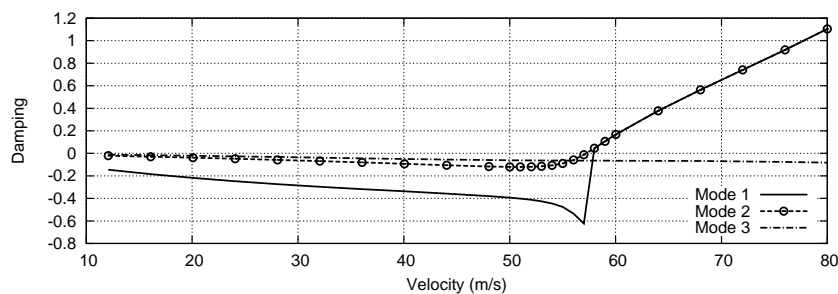
Table 9.15: Flutter velocities of the isotropic plate wing for different sweep angles by means of DSM and FEM; $N = 4$ TE model

Λ	$N = 2$	$N = 3$	$N = 4$
-30°	84.086	59.366	58.188
-20°	64.769	51.559	51.559
-10°	49.676	46.210	46.371
0°	69.388	68.503	68.523
10°	65.441	64.305	64.506
20°	66.408	61.046	59.130
30°	70.145	57.747	57.216

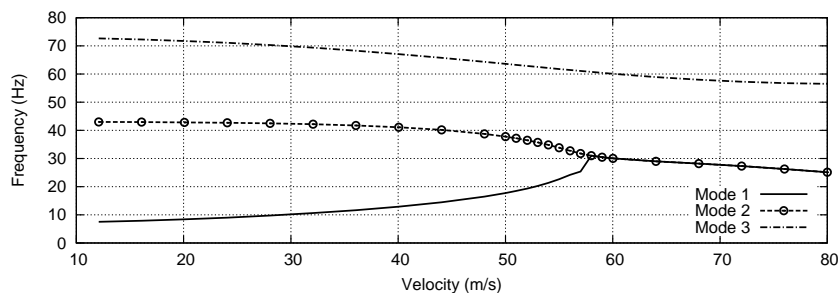
Table 9.16: Effect of the expansion order (N) on the flutter velocity (m/s) of the isotropic plate wing by means of DSM

Λ	$N = 2$	$N = 3$	$N = 4$
-30°	64.773	52.181	51.668
-20°	61.616	56.737	56.581
-10°	62.020	59.816	59.746
0°	40.002	39.029	38.995
10°	38.362	37.361	37.352
20°	36.736	35.095	34.793
30°	34.156	31.887	31.616

Table 9.17: Effect of the expansion order (N) on the flutter frequency (Hz) of the isotropic plate wing by means of DSM



(a) Damping vs velocity



(b) Frequency vs velocity

Figure 9.31: Frequency and damping vs free-stream velocity for the isotropic plate wing; $\Lambda = 30^\circ$, DSM $N = 4$ TE model

- The $N = 3$ and $N = 4$ models provide similar results. This means that the convergence to the exact solution with respect to the beam order is almost obtained.
- The $N = 2$ model provides reliable results for moderate or null sweep angles.

9.5.2 Composite plate wing

In the second analysis case, composite wing structures are considered. Composite plate wing models were retrieved from [96] and from [94]. A graphite/epoxy composite material with the following characteristics is used: $E_1 = 98.0$ GPa, $E_2 = 7.90$ GPa, $G_{12} = 5.60$ GPa, Poisson ratio $\nu = 0.28$ and $\rho = 1520$ kg/m³. The length of the wing (L) is equal to 305 mm and the chord (c) is equal to 76.2 mm. The total thickness of the laminate is 0.804 mm.

First, symmetric six-layer laminates with constant thickness layers are considered. The plate wing is straight ($\Lambda = 0^\circ$). Table 9.18 shows the flutter velocities for various stacking sequences and various beam models. The results from the present CUF DSM refined elements were compared with those from CLT (Classical Laminate Theory) plate models and with experimental results from the literature.

An eight-layer symmetric stacking sequence is then considered. The stacking sequence is $[-22.5/67.5/22.5/-67.5]_s$, whereas the thickness sequence is $[0.09/0.12/0.16/0.63]_s$, where each term indicates the thickness ratio of each ply with respect to the half of the thickness of the laminate. For instance, the thickness of the first layer is the 9% of the half thickness of the laminate. Two sweep angles are considered, $\Lambda = 0^\circ$ and $\Lambda = 30^\circ$. The natural frequencies and the flutter velocities are given in Tables 9.19 and 9.20, in which the results from the present variable order 1D DSM models are compared with those from plate models and from experiments. Finally, the nodal lines of the first sixth mode shapes

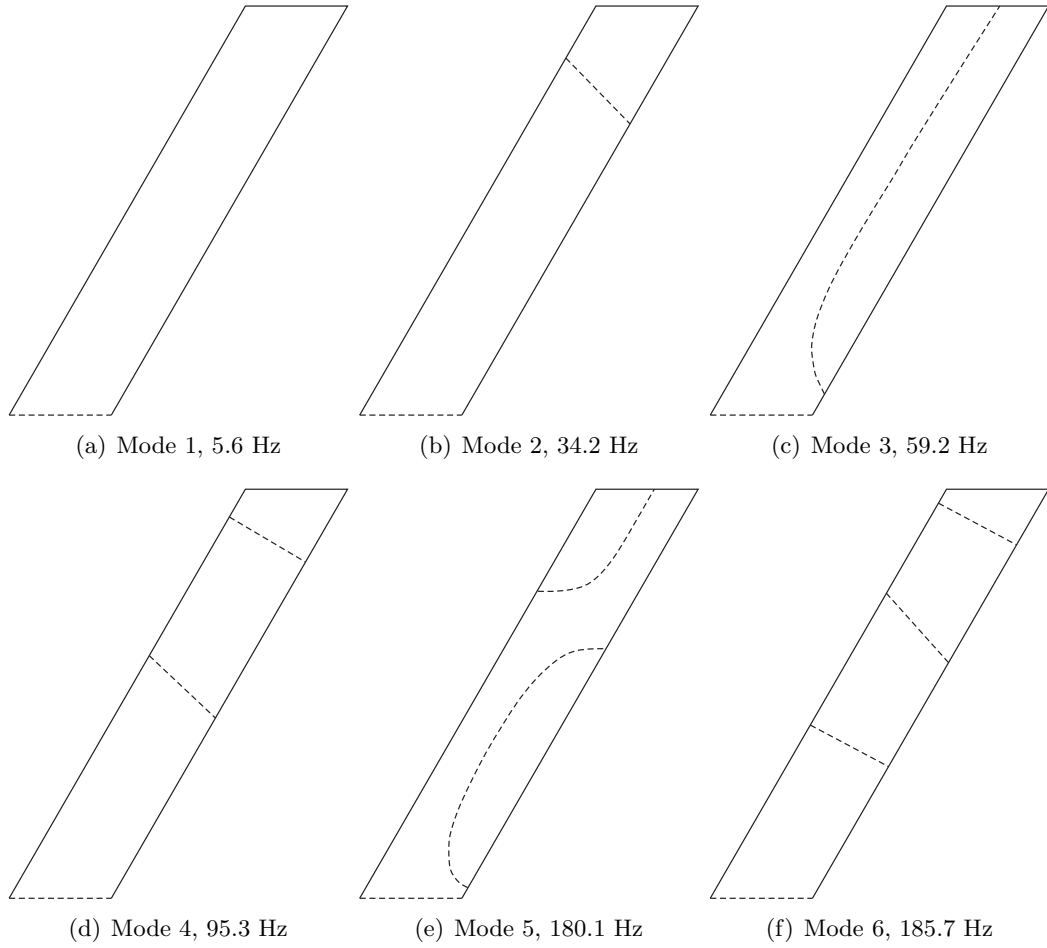


Figure 9.32: Mode shapes of the eight-layer swept ($\Lambda = 30^\circ$) plate wing; DSM $N = 4$ TE model

of the swept wing ($\Lambda = 30^\circ$) via the $N = 4$ DSM beam model are shown in Fig. 9.32. The flutter analyses of the composite wings confirm the previous conclusions and demonstrate that the proposed method allows for accurate and efficient flutter analysis of both isotropic and composite plate wings.

Stacking	$N = 2$	$N = 3$	$N = 4$
$[0_2/90]_s$			
CLT, 23.0 EXP, 25	23.3	23.3	23.2
$[45/-45/0]_s$			
CLT, 40.1 EXP, > 32	43.3	40.4	40.4
$[45_2/0]_s$			
CLT, 27.5 EXP, 28	32.5	26.9	26.7
$[30_2/0]_s$			
CLT, 27.1 EXP, 27	29.3	26.3	26.3

Table 9.18: Flutter velocities (m/s) for the six-layer straight plate wing; DSM CUF beams vs CLT [96] and experimental [94] results

Model	f_1	f_2	f_3	f_4	f_5	V_f
$N = 2$	7.4	46.1*	59.1	129.5*	182.7	38.2
$N = 3$	7.2	45.1*	59.1	126.5*	182.4	38.2
$N = 4$	7.2	45.0*	59.1	126.4*	182.3	38.1
CLT [96]	7.3	45.4*	59.1	127.7*	182.3	38.8

*Torsional mode

Table 9.19: Natural frequencies (Hz) and flutter velocities (m/s) of an eight-layer straight plate wing via different models

Model	f_1	f_2	f_3	f_4	f_5	V_f
$N = 2$	5.6	34.7	76.5*	97.5	193.3*	38.6
$N = 3$	5.6	34.4	60.1*	95.9	187.0*	31.5
$N = 4$	5.6	34.2	59.2*	95.3	180.1*	31.7
CLT [96]	5.6	34.4	60.0*	95.4	182.0*	32.4

*Torsional mode

Table 9.20: Natural frequencies (Hz) and flutter velocities (m/s) of an eight-layer swept ($\Lambda = 30^\circ$) plate wing via different models

9.6 Dynamic and gust response analyses

In this section, dynamic and gust response analyses of simple and complex structure are discussed. The analyses are carried out according to Chapter 7 by using both TE and CW CUF models. First a simple dynamic problem is considered to assess the mode superposition method as an effective means to conduct time-history analyses. Discrete gust responses of plate-like as well as complete wing structures are subsequently presented.

9.6.1 Square cross-section beam subjected to sinusoidal loading

A simply-supported square cross-section beam is considered in order to validate the mode superposition method, which has been described in Chapter 7 for the solution of time-domain dynamic problems.

Each side of the cross-section of the beam is equal to 0.1 m, whereas the span-to-height ratio L/h is equal to 100. The structure is considered to be made of an aluminium alloy with elastic modulus equal to $E = 69$ GPa, Poisson ratio $\nu = 0.33$, and density $\rho = 2700$ kg/m³. A single sinusoidal load, with amplitude $P_{z_0} = -1000$ N and angular frequency $\omega = 7$ rad/s, is applied at the mid-span section

$$P_z(t) = P_{z_0} \sin(\omega t) \quad (9.3)$$

CUF models are discretized by FEM and 10 cubic ($p = 3$) Lagrange 1D elements are used along the beam axis for the analysis under consideration.

The same problem was addressed by Carrera and Varello [50] by means of the Newmark direct integration scheme. Analytical solutions are also provided in the following as addressed in [165]. In order to be consistent with reference and analytical results, only EBBM models are discussed as TE models. However, also a 1 L9 LE model is addressed in order to demonstrate the versatility of the present mode superposition method.

Time-history of the transverse displacement u_z at the mid-span section is shown in Fig. 9.33. Only the first mode shape has been used for mode superposition and this ensure

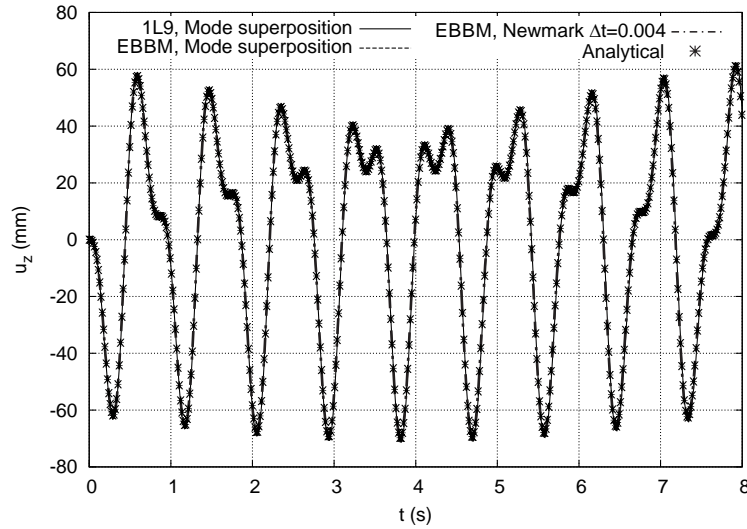


Figure 9.33: Vertical displacement at the mid-span cross section of the EBBM beam subjected to sinusoidal load

a perfect agreement with reference results. However, more than one single mode shape might be necessary for correct dynamic analyses in some cases, e.g. when (i) the loading frequency is comparable or higher than the first natural frequency of the structure; (ii) more than one mode participates to the dynamic response due to non-symmetrical loadings or structural/material couplings. For this reason, converge analyses versus the number of mode shapes to include into mode superposition analysis are necessary in most of the problems of practical interest, such as discrete gusts analyses discussed in the following sections.

9.6.2 Sweep angle effect on gust response of metallic plate wings

Discrete one-minus-cosine response of the same isotropic plate wing as considered in Section 9.5.1 and in Pagani et al. [123] is addressed hereinafter. The aircraft is supposed flying at altitude $h = 3097.82$ m (i.e., $\rho_\infty = 0.9$ kg/m³) with speed $V_\infty = 15$ m/s. The wing loading is $W/S = 40.77$ kg/m². At time $t = 0$, a vertical gust with amplitude $U_0 = 15$ m/s and duration $t_g = 0.4$ s is encountered. The wing is supposed to fly at null incidence with $C_{L_\alpha} = 2\pi$ rad⁻¹. The following results are given in terms of displacement variations with respect to equilibrium state. No structural damping is taken into consideration.

The $\Lambda = 30^\circ$ swept-back wing is considered first. DSM was used to calculate mode shapes and natural frequencies of the wing structures to be used in conjunction with mode superposition to conduct dynamic gust responses. From convergence analyses it was clear that at least the first two mode shapes are necessary for mode superposition. Free vibration results of the structure under consideration are given in Section 9.5.1. The necessity for the adoption of refined models is clear from Fig. 9.34, where the vertical displacement variation, Δu_z , of the trailing edge at the tip cross-section via various classical and higher-order TE models is shown. Gust pulse profile is also shown in Fig. 9.34. In addition, Fig. 9.35 further demonstrates the need for at least a fourth beam model ($N = 4$) for the gust response of the 30° swept-back wing. In fact, the figure shows the bending torsional coupling as the difference of the deflections of the leading and trailing edges.

The fourth order ($N = 4$) TE model is therefore used in the following analysis, which is summarized in Fig. 9.36 where the effect of the sweep angle Λ on the time history

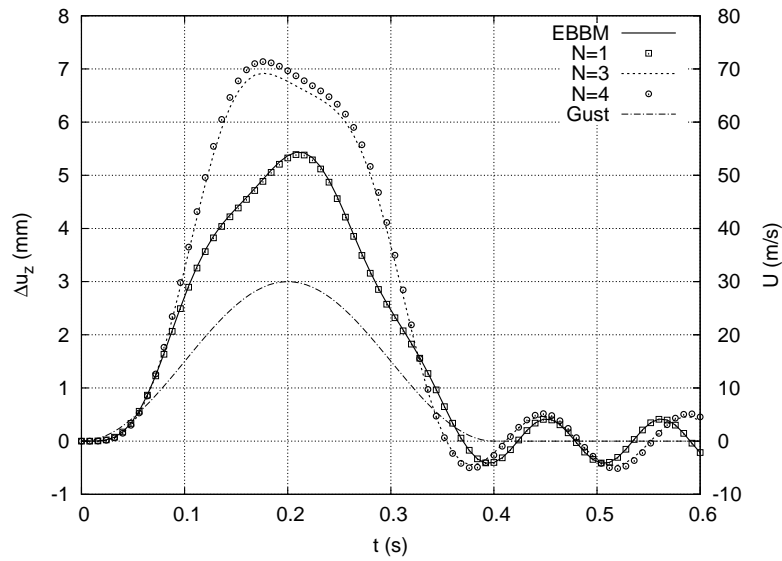


Figure 9.34: Vertical displacement variation at the tip trailing edge for the $\Lambda = 30^\circ$ swept-back wing undergoing a gust load

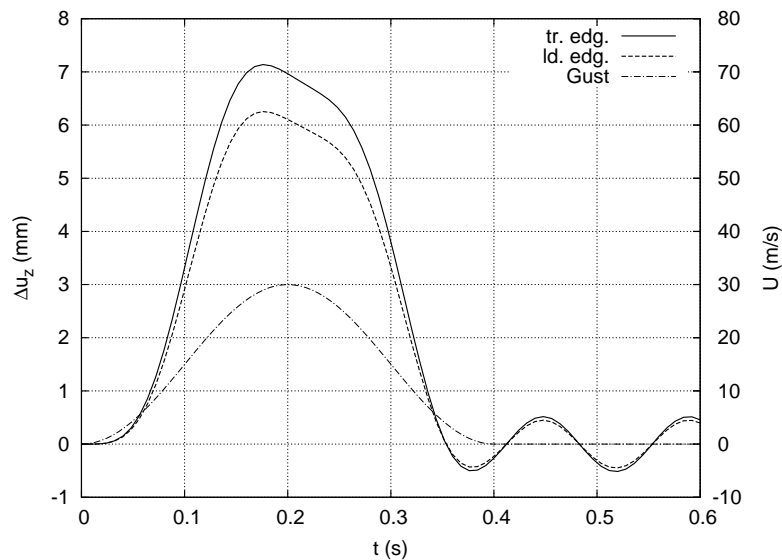


Figure 9.35: Vertical displacement variations of the leading and trailing edges at the tip for the $\Lambda = 30^\circ$ swept-back wing undergoing a gust load; Fourth-order ($N = 4$) model

of the vertical displacements is shown. As expected, swept wings are more sensitive to gust loadings than straight wings. Nevertheless, for the given gust, Table 9.21 shows that inertial effects are more important in straight wings than in swept wings for the case under consideration. In fact, Table 9.21 quotes the dynamic load factors (DLF) for each wing configuration, where DLF is the ratio between the dynamic pick response and the static response, evaluated by neglecting inertial terms in Eq. (7.8).

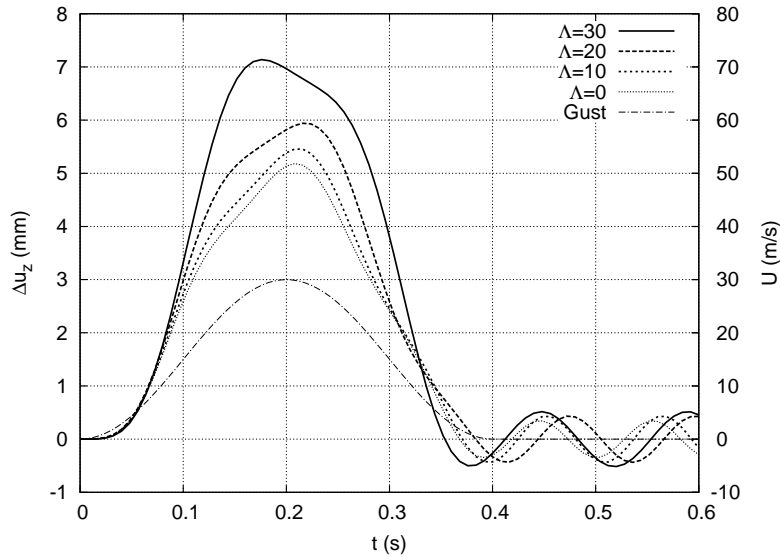


Figure 9.36: Effect of the sweep angle Λ on the maximum vertical displacement variations of the metallic plate wing undergoing a gust load; Fourth-order ($N = 4$) model

Λ	$\Delta u_{z_{\max}}$, dyn (mm)	$\Delta u_{z_{\max}}$, st (mm)	DLF
0	5.255	4.912	1.070
10	5.692	5.343	1.065
20	6.186	5.940	1.041
30	7.138	6.894	1.035

Table 9.21: Dynamic load factor for the metallic plate wing undergoing a gust load; Fourth-order ($N = 4$) model

9.6.3 Composite plate wing

Gust response analyses of the six-layer composite straight plate wings, whose free vibration and flutter characteristics have been investigated in Section 9.5.2 and in Pagani et al. [123], are addressed hereafter. The aircraft is supposed to fly at the same conditions as in the previous analysis case. The intensity and the duration of the discrete gust is the same as well.

Results by a fourth-order ($N = 4$) model are provided in the following and DSM was used to extract the first two mode shapes and related natural frequencies out of the structure. An higher-order TE model is exploited because of the ineffectiveness of the classical and lower-order models as demonstrated in the previous example and in Table 9.22, where the effects of the TE theory order on the maximum displacements at the leading and trailing edges of the $[45/45/0]_s$ plate wing are highlighted.

Figure 9.37 shows the time history of the maximum vertical displacement for the composite wings with various stacking sequences subjected to gust. The displacement values are given in terms of variations with respect to an equilibrium state.

The effect of the gust duration, t_g , on the maximum displacement variation for each plate wing lamination is shown in Fig. 9.38. As expected, the position of the maximum pick response is different for different stacking sequences: For a given lamination, the maximum dynamic load factor (hence, the most critical case characterized by the maximum displacement) fall into a region close to the value of t_g such that $2\pi/t_g = \omega_1$, where ω_1 is

Model	$\Delta u_{z_{\max}}$ (mm)	
	Ld. edg.	Tr. edg.
EBBM	18.36	18.36
$N = 1$	19.19	19.19
$N = 2$	25.02	21.74
$N = 3$	25.23	22.24
$N = 4$	25.33	22.28

Table 9.22: Effect of the theory order on the maximum vertical displacements for the composite plate wing undergoing a 0.4 s gust load; $[45/45/0]_s$ lamination

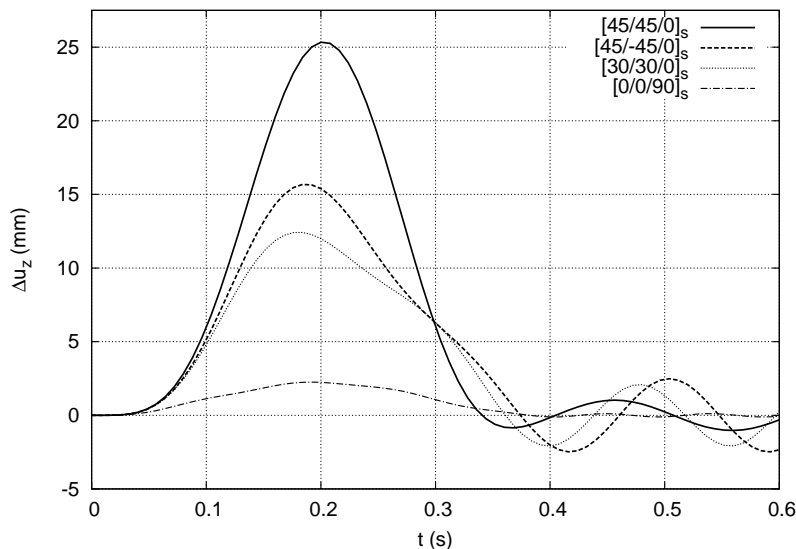


Figure 9.37: Maximum vertical displacement variations of various composite wings undergoing a 0.4 s gust load; Fourth-order ($N = 4$) model

the first natural frequency (in rad/s) of the structure. The reason is that the first natural mode shape dominates the gust response.

Conflicting conclusions can be extrapolated from the analysis described here and from the results provided in Section 9.5; it is therefore clear that dynamic gust response may play an important role for the final design of swept and composite wings.

9.6.4 Complete NACA aircraft wing

The complete wing with NACA 2415 airfoil section is considered as the last example about gust response. Geometrical and mechanical characteristics as well as free vibrations analysis of the wing can be found in Section 9.3.2 and in Carrera et al. [40]. The three-bay configuration is used for the following analysis. The airplane has a wing loading W/S equal to 378.6 kg/m^2 and it is supposed to fly at sea level ($\rho_\infty = 1.225 \text{ kg/m}^3$) with velocity $V_\infty = 80 \text{ m/s}$. At 1-g flight condition, a vertical gust with intensity $U_0 = 10 \text{ m/s}$ and duration $t_g = 0.4 \text{ s}$ is encountered. A $C_{L_\alpha} = 7.6 \text{ rad}^{-1}$ was estimated by means of XFRLR5 [61] and XFOIL [63] computer programs and by supposing inviscid flow.

No damping is assumed for the first analysis in Fig. 9.39, where the effect of the number of modes for mode superposition on the maximum displacements by CW model at leading

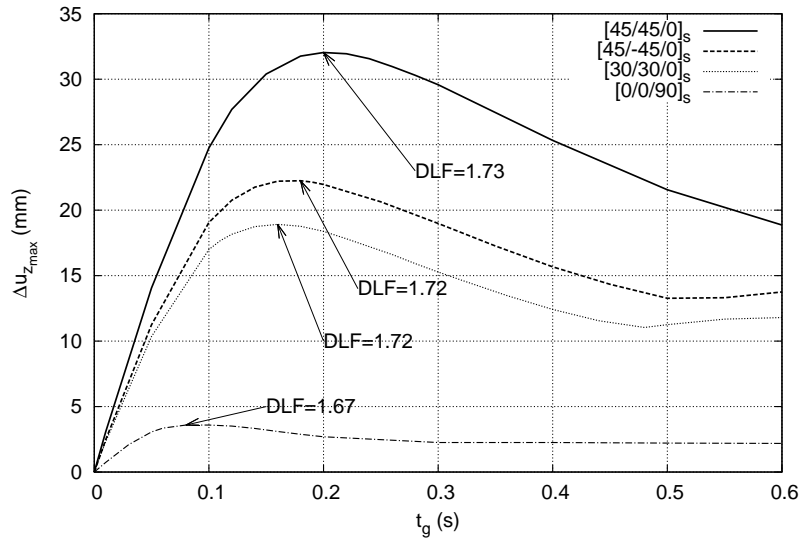


Figure 9.38: Effect of the gust duration, t_g , on the maximum pick displacement for various composite wings undergoing a gust load; Fourth-order ($N = 4$) model

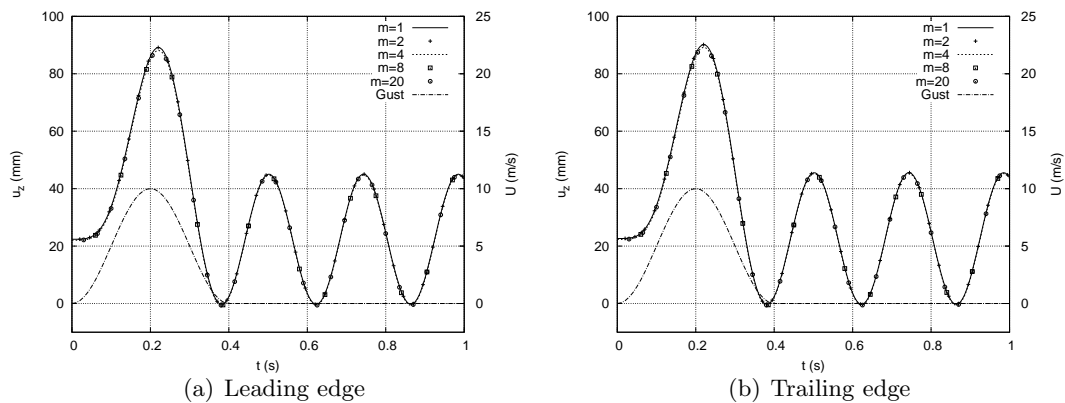


Figure 9.39: Effect of number of modes, m , in mode superposition solution for the gust response analysis of the complete NACA wing; CW model

and trailing edges is shown. The gust velocity profile is also depicted in Fig. 9.39. It should be noted that a few modes ($m = 4$) were necessary to ensure the convergence of the response; indeed, the mechanics of the structure is dominated by bending modes, which occupy the first positions in the eigenvector matrix Φ (see Eq. (7.10)). Figure 9.39 also demonstrates that a slight torsion is produced under discrete gust loading for the structure under consideration.

In the second analysis case of the NACA 2415 wing, the effects due to a concentrated non-structural mass (e.g. engine) are investigated. For this analysis, a β coefficient equal to 5×10^{-3} for Rayleigh damping (see Eq. (7.23)) is assumed. The gust and the other analysis data are the same as in the previous case. The mass (300 Kg) is placed at the wing underside in correspondence of the intersection between the first rib at $y = 2$ m and the front spar. Figure 9.40 shows the difference in maximum deflections between classical EBBM and CW model. Moreover, Table 9.23 quotes the maximum displacements for dynamic and related static analyses as well as maximum DLF's by various models. It

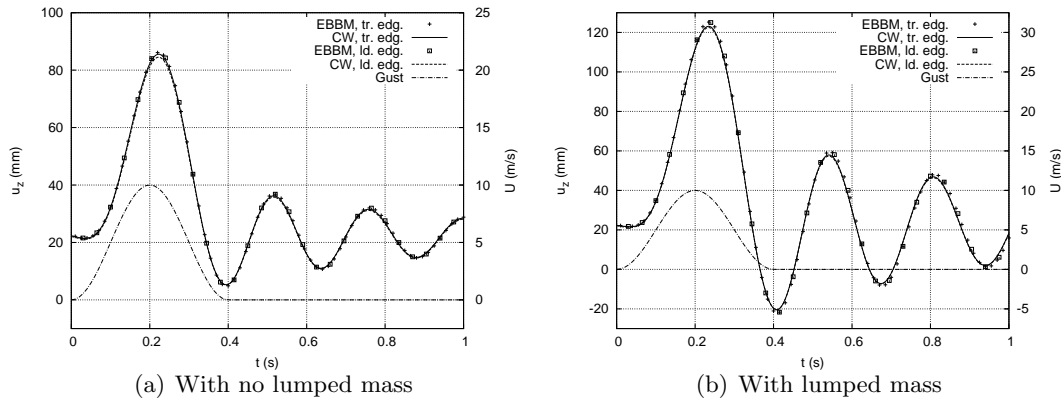


Figure 9.40: Comparison of maximum displacements at leading and trailing edges by EBBM and CW model; $\beta = 5 \times 10^{-3}$

Model	With no lumped mass			With lumped mass		
	$u_{z_{max}}$, dyn (mm)	$u_{z_{max}}$, st (mm)	DLF	$u_{z_{max}}$, dyn (mm)	$u_{z_{max}}$, st (mm)	DLF
EBBM	86.163	67.322	1.280	125.268	90.827	1.379
TBM	86.204	67.346	1.280	124.975	90.629	1.379
$N = 2$	82.840	65.169	1.271	119.040	87.173	1.366
CW	85.541	66.965	1.277	123.159	89.449	1.377

Table 9.23: Dynamic load factor for the complete NACA wing undergoing a gust load; $t_g = 0.4$ s and $\beta = 5 \times 10^{-3}$

is noticed that: (i) even classical beam models such as EBBM provide good results for the case under consideration, at least for the configuration with no lumped mass; (ii) the non-structural mass obviously deteriorates the dynamic response capabilities of the wing since inertial effects are more important. This latter conclusion is also supported by Fig. 9.41, which shows the effect of the discrete gust duration on the maximum static and dynamic vertical displacement by the CW model of the wing. Also, maximum DLF's are given in Fig. 9.41 for each case and both up- and down-gusts are considered. It might

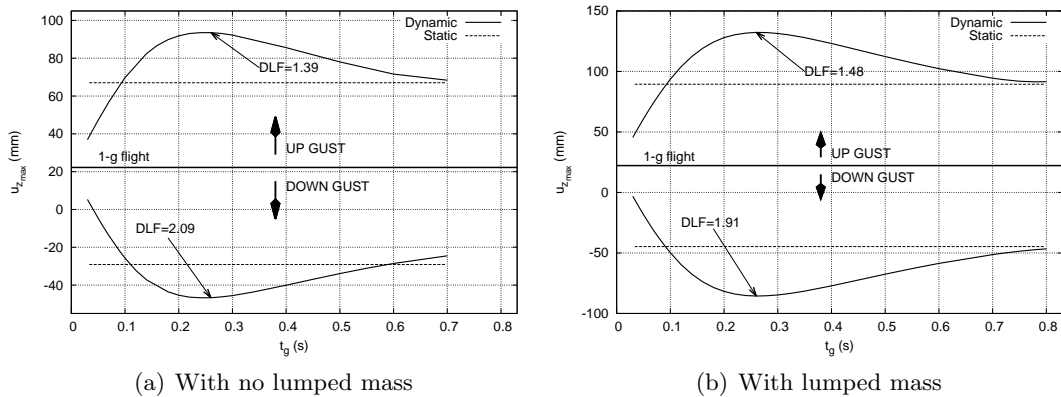


Figure 9.41: Effect of the gust duration on the maximum deflection of the complete NACA wing; CW model

be deduced by this last figure that static gust analyses (i.e. inertial terms are neglected) are conservative only in a narrow range of t_g and dynamic response should be considered otherwise.

9.7 Stokes flows

In this section, the results from the fluid-dynamics CUF formulation (see Chapter 8) is assessed and compared versus analytical solutions and OpenFOAM [82], an open source finite volume software. Velocity and pressure trends are investigated in a circular cross-section domain as shown in Fig. 8.2. The pipe has a length $L = 6$ m and radius $r = 1$ m. In all the following analyses, a homogeneous Dirichlet boundary condition is prescribed on the lateral surface Γ_D^l which means a no-slip condition at the pipe wall. A homogeneous Neumann boundary condition is instead prescribed on the outlet section Γ_N^{out} . On the contrary, a nonhomogeneous Dirichlet boundary condition (different for each case) is assigned to the inlet section Γ_D^{in} . No body forces are applied to the fluid, which means $\mathbf{f} = \mathbf{0}$ in Eq. (8.2). Finally, a kinematic viscosity ν equal to 10^{-2} m²/s is considered, which the reader can verify resulting in very low Reynolds numbers ($Re \ll 1$) for all the cases below. For all the discussed analyses, CUF models are discretized with 10 1D FEM elements, which ensured convergent results.

9.7.1 Poiseuille flow

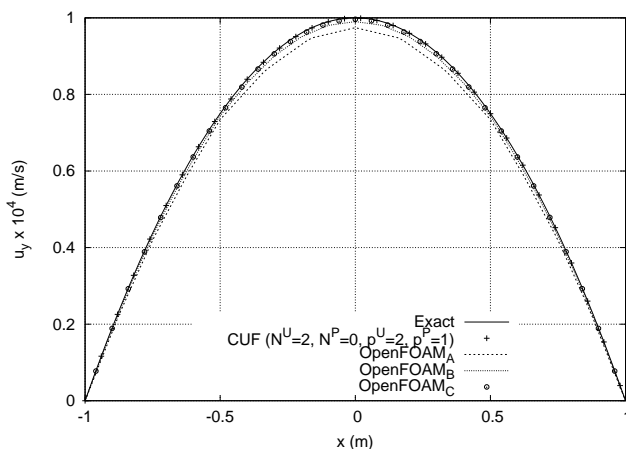
In the Poiseuille flow, the fluid flow is axisymmetric and the velocity \mathbf{u} does not depend on the position along the longitudinal axis y . In particular, the axial velocity u_y is paraboloidal on the two-dimensional cross-section, and the maximum axial velocity occurs at point $(x = 0, z = 0)$ of each section. In order to simulate this flow, the following Dirichlet boundary condition is applied on Γ_D^{in} :

$$\begin{cases} u_x = 0 \\ u_y = 10^{-4} (1 - x^2 - z^2) \\ u_z = 0 \end{cases} \quad \text{on } \Gamma_D^{\text{in}} \quad (9.4)$$

According to the Poiseuille flow, over the cross-section an accuracy of the second-order for the velocity and of the “zero-order” (constant trend) for pressure should be sufficient to detect the solution. In the framework of CUF, this means that a 1D model with $N^U = 2$ and $N^P = 0$ should be sufficient to detect the exact solution, which is demonstrated by Table 9.24. In this table, CUF and OpenFOAM results are compared with those from analytical solution [13, 151] and the number of degrees of freedom (DOFs) is also given for each model. Regarding OpenFOAM results, the *SimpleFoam* steady-state solver for

Model	e_p (%)	e_{u_y} (%)	DOFs
OpenFOAM _A	-0.72	-2.56	10560
OpenFOAM _B	-0.25	-0.97	54400
OpenFOAM _C	0.21	-0.39	435520
CUF	-0.05	-0.05	389

Table 9.24: Inlet pressure and maximum axial velocity in terms of percentage errors versus analytical solution for the Poiseuille flow; Comparison of CUF ($N^U = 2$, $N^P = 0$, $p^U = 2$, $p^P = 1$) and OpenFOAM results

Figure 9.42: Poiseuille flow velocity profile at $y = 3$ m

incompressible, laminar, Newtonian flows was used. In Table 9.24 the model OpenFOAM_A was constructed with 2640 finite volumes (132×20 mesh, where 132 stands for the number of volumes on the cross-section and 20 is the discretization along the y -axis), OpenFOAM_B has 13600 (340×40) finite volumes, and OpenFOAM_C has 108800 (1368×80) finite volumes. The efficiency of the present methodology for the problem discussed here is widely demonstrated and confirmed by Fig. 9.42, which shows the velocity profiles at the mid-span cross-section by different models.

Both in Table 9.24 and Fig. 9.42, quadratic Legendre shape functions (see Eq. (8.19)) were used for the velocity field ($p^U = 2$) and linear Legendre shape functions were used for the pressure field ($p^P = 1$) in the FEM approximation along the y -axis. However, particular attention should be focussed on the choice of these polynomial orders in the case of fluid-dynamics analyses. As detailed in [160], in fact, finite elements of the same polynomial degree for both velocity and pressures are in general unstable. This sentence is verified by Fig. 9.43, which shows the variation of the discrete pressure p along the beam axis for various choices of shape functions. It is noteworthy that spurious modes appear as $p^P = p^U$. Moreover, instabilities reduce as the polynomial degrees increase.

9.7.2 Fourth-order velocity profile

The results shown in the previous section may be easily reproduced by classical 1D models for Stokes flows. A more complex flow is therefore introduced hereinafter to show the 3D-like capabilities of CUF models. The following fourth-order velocity profile is enforced at the inlet cross-section:

$$\begin{cases} u_x = 0 \\ u_y = 10^{-4} (1 - x^2 - z^2)^2 \\ u_z = 0 \end{cases} \quad \text{on } \Gamma_D^{\text{in}} \quad (9.5)$$

Note that the flow is still axisymmetric.

According to the conclusions made previously about stable spaces and shape functions, the parameters p^U and p^P are respectively set equal to 4 and 3 and Legendre shape functions are used. Table 9.25 shows the effect of the theory expansion orders N^U and N^P on the maximum inlet pressure and axial velocity at the middle cross-section.

Table 9.25 demonstrates that the CUF model $N^U = 6$, $N^P = 4$ provides convergent results. This model is therefore used in Fig. 9.44, where pressure and axial velocity trends

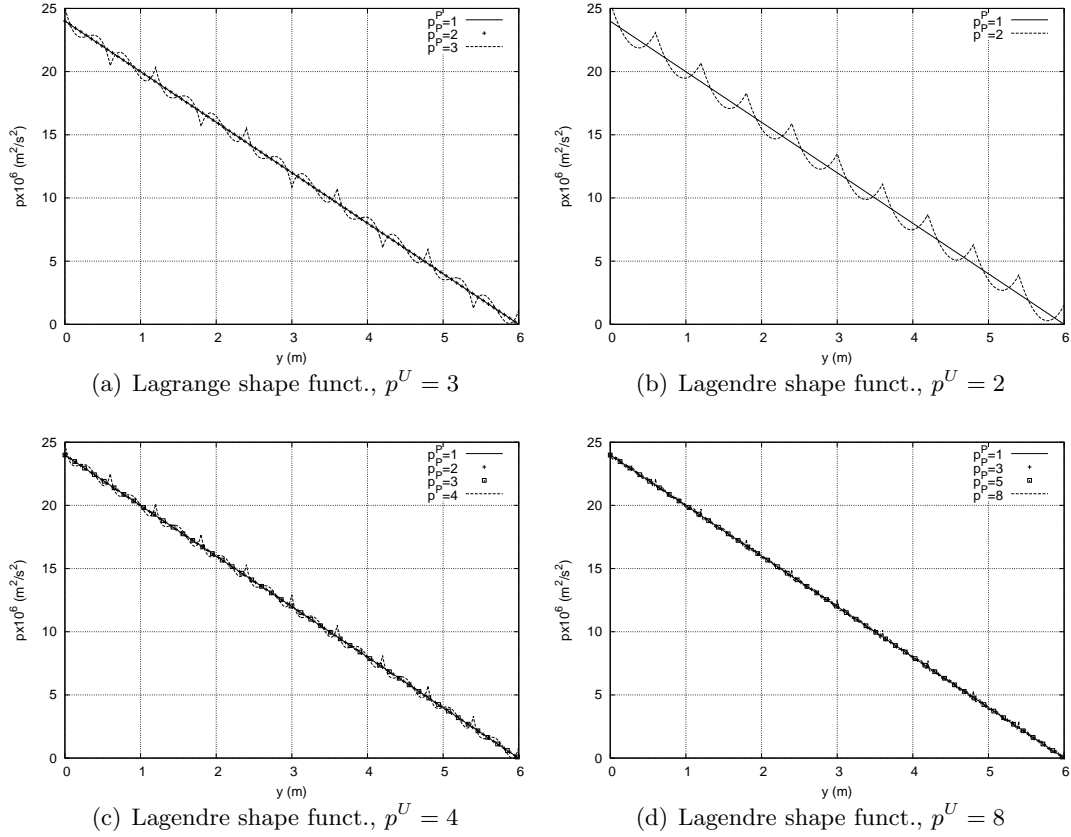


Figure 9.43: Pressure trends along y for the Poiseuille flow by CUF ($N^U = 2$, $N^P = 0$); Comparison of various combinations of Lagrange and Legendre shape functions

Model		$p \times 10^5$ (m ² /s ²)	$u_y \times 10^5$ (m/s)	DOFs
OpenFOAM				
OpenFOAM _A		1.70	6.50	10560
OpenFOAM _B		1.79	6.53	54400
OpenFOAM _C		1.87	6.36	435520
CUF				
N^U	N^P			
10	9	1.86	6.66	9823
8	7	1.86	6.66	6651
8	6	1.86	6.66	6403
6	5	1.86	6.66	4095
6	4	1.86	6.66	3909
6	3	1.78	6.66	3754
4	3	1.79	6.66	2155
4	2	1.79	6.66	2031
4	1	1.60	6.66	1938

Table 9.25: Maximum inlet pressure and maximum axial velocity at $y = 3$ by various models of the fourth-order inlet velocity flow; CUF models discretized by $p^U = 4$ and $p^P = 3$ Legendre FEM elements

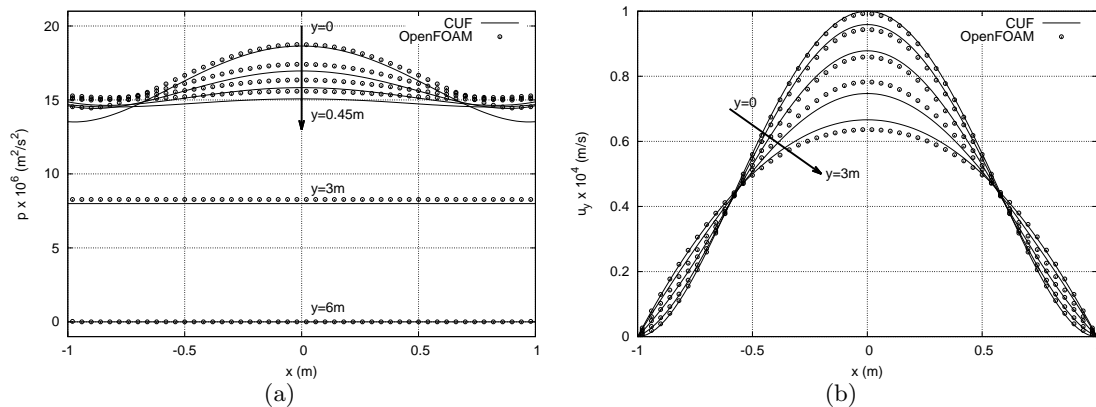


Figure 9.44: Pressure (a) and axial velocity (b) trends along x -axis at $z = 0$ and at $y = 0$, $y = 0.15$ m, $y = 0.3$ m, $y = 0.45$ m, $y = 3$ m, and $y = 6$ m for the fourth-order inlet velocity flow; Comparison of CUF ($N^U = 6$, $N^P = 4$, $p^U = 4$, $p^P = 3$) and OpenFOAM_C results

at various sections are shown and compared to the results by the model OpenFOAM_C. It is interesting to note that the velocity field is fully developed at $y = 3$ m and it approaches a paraboloidal Poiseuille profile as analyzed in the previous section; hence, velocity profile at $y = 6$ m is not provided in Fig. 9.44b. The transition from the inlet pressure profile to the constant pressure profile is also well depicted in Fig. 9.44a. The results show the great advanced capabilities of the proposed CUF models for complex Stokes flows. The slight differences between CUF models and the OpenFOAM ones may be due to the lack of the convective terms that are neglected in the proposed CUF approximation.

9.7.3 Fifth-order velocity profile

A non-axisymmetric flow is studied as the last example, where a fifth-order nonhomogeneous Dirichlet boundary condition is prescribed on the axial velocity u_y as follows:

$$\begin{cases} u_x = 0 \\ u_y = 10^{-4} (1 - x^2 - z^2)(1/4 + xz + x^3) \\ u_z = 0 \end{cases} \quad \text{on } \Gamma_D^{\text{in}} \quad (9.6)$$

The 1D mesh is not changed with respect to the previous case for CUF models, hence $p^U = 4$ and $p^P = 3$ in the following analyses. Table 9.26 shows the effect of the 1D CUF expansion orders N^U and N^P on the maximum inlet pressure and maximum axial velocity at $y = 3$. In this table, CUF results are compared with those from OpenFOAM and the number of DOFs is also given for each model implemented. Table 9.26 clearly shows that at least a $N^U = 6$ model is necessary to correctly detect the maximum value of the pressure field at the inlet. Furthermore, Fig. 9.45 shows the effects of the pressure theory order N^P on the pressure profile at the inlet. It is clear that at least $N^U = 6$, $N^P = 5$ expansions are needed for CUF approximation in order to detect the convergent solution. This model is therefore used in the remaining analyses.

The axial velocity profiles at various cross-section till $y = 3$ m (where the flow is fully developed) are shown in Fig. 9.46. It is clear that a flow transition occurs downline of the inlet section. Nonetheless, the profiles of velocity u_y gradually approach the more natural condition of axisymmetry, because of the outlet Neumann boundary condition and

Model	$p \times 10^6$ (m ² /s ²)	$u_y \times 10^5$ (m/s)	DOFs
OpenFOAM			
OpenFOAM _A	7.20	2.43	10560
OpenFOAM _B	8.17	2.44	54400
OpenFOAM _C	9.08	2.35	435520
CUF			
N^U	N^P		
10	9	9.52	2.50
8	7	9.48	2.50
8	6	9.57	2.50
6	5	9.23	2.50
6	4	10.72	2.50
6	3	10.72	2.50
5	4	10.80	2.50
5	3	10.80	2.50
5	2	8.03	2.50

Table 9.26: Maximum inlet pressure and maximum axial velocity at $y = 3$ by various models of the fifth-order inlet velocity flow; CUF models discretized by $p^U = 4$ and $p^P = 3$ Legendre FEM elements

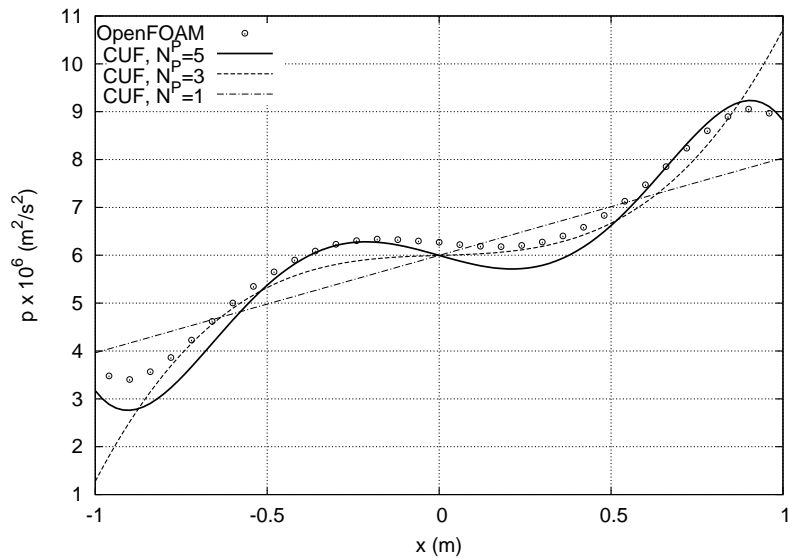


Figure 9.45: Effect of the parameter N^P on the pressure trends along x -axis at $(y = 0, z = 0)$ for the fifth-order inlet velocity flow; Comparison of CUF ($N^U = 6, p^U = 4, p^P = 3$) and OpenFOAM_C results

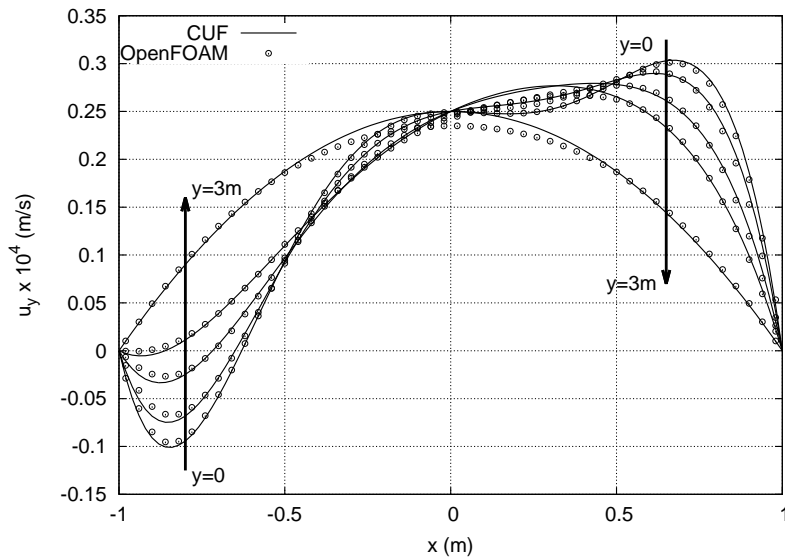


Figure 9.46: Axial velocity profile along x -axis at $z = 0$ and at $y = 0$, $y = 0.15$ m, $y = 0.3$ m, $y = 0.45$ m, and $y = 3$ m for the fifth-order inlet velocity flow; Comparison of CUF ($N^U = 6$, $N^P = 5$, $p^U = 4$, $p^P = 3$) and OpenFOAM_C results

the lateral homogeneous Dirichlet boundary condition, which is obviously axisymmetric. Similarly to what observed for the fourth-order inlet profiles, the velocity \mathbf{u} tends towards the paraboloidal behavior typical of the Poiseuille flow.

Map plots of the three components of the velocity field at $y = 0.3$ m are shown in Figs. 9.47 to 9.49. From these figures, one can easily note that the Dirichlet homogeneous boundary condition on the pipe wall is satisfied. Moreover, it is clear that in the transition zone the flow is completely non-axisymmetric.

The behaviour of the flow in the transition zone is further investigated by Figs. 9.50 and 9.51. The fifth-order velocity inlet profile case is an important assessment for the 1D CUF FE model for fluid-mechanics, because it demonstrates its capability to predict the evolution of complex flows (not violating the equations governing the fluid-dynamics) also in case of non-axisymmetric complex flows. The key point is that this feature is not typical

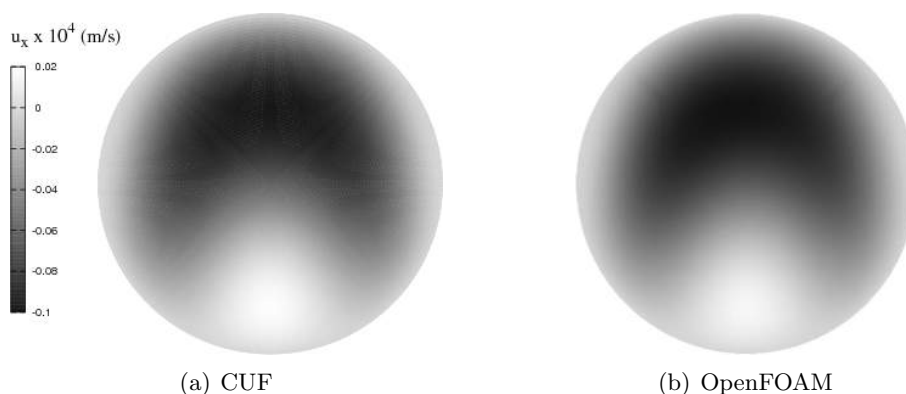


Figure 9.47: Velocity profiles u_x at $y = 0.3$ m for the fifth-order inlet velocity flow; Comparison of CUF ($N^U = 6$, $N^P = 5$, $p^U = 4$, $p^P = 3$) and OpenFOAM_C results

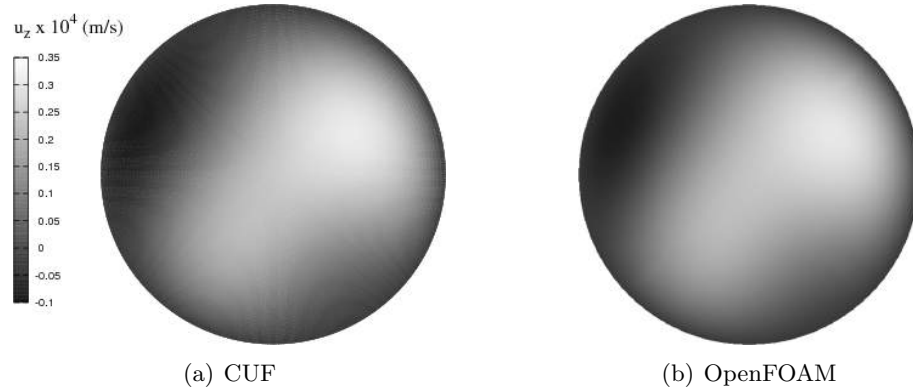


Figure 9.48: Velocity profiles u_y at $y = 0.3$ m for the fifth-order inlet velocity flow; Comparison of CUF ($N^U = 6$, $N^P = 5$, $p^U = 4$, $p^P = 3$) and OpenFOAM_C results

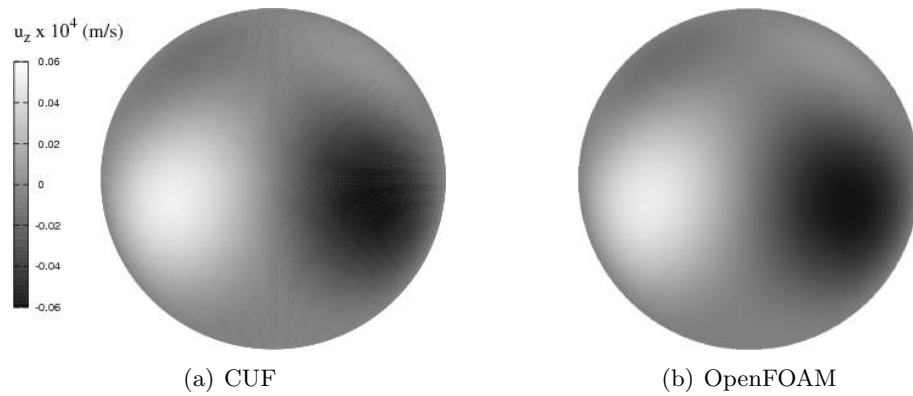


Figure 9.49: Velocity profiles u_z at $y = 0.3$ m for the fifth-order inlet velocity flow; Comparison of CUF ($N^U = 6$, $N^P = 5$, $p^U = 4$, $p^P = 3$) and OpenFOAM_C results

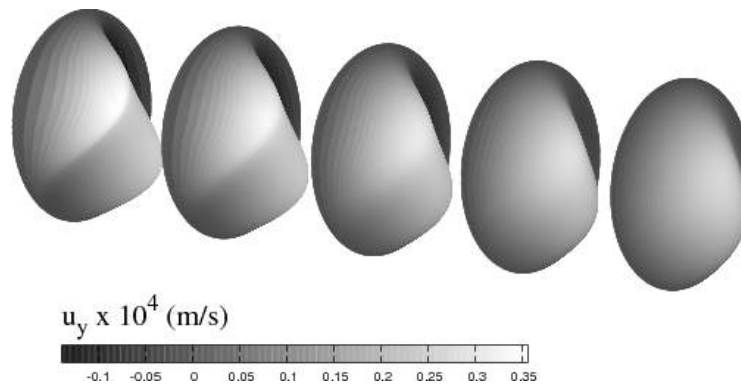


Figure 9.50: Axial velocity profiles along the transition zone at $y = 0$, $y = 0.15$ m, $y = 0.3$ m, $y = 0.45$ m, and $y = 0.6$ m for the fifth-order inlet velocity flow; CUF model ($N^U = 6$, $N^P = 5$, $p^U = 4$, $p^P = 3$)

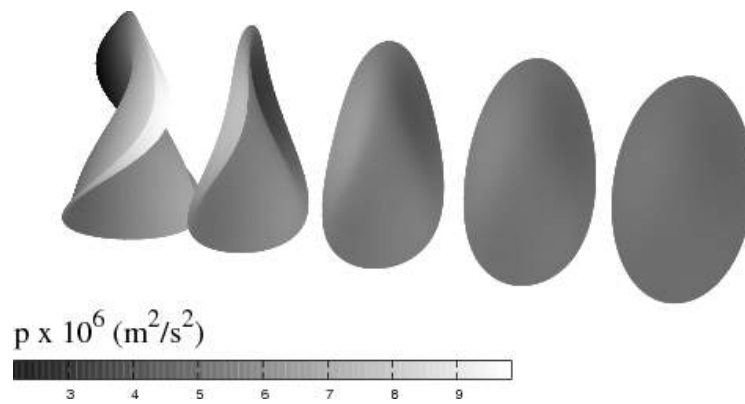


Figure 9.51: Pressure profiles along the transition zone at $y = 0$, $y = 0.15$ m, $y = 0.3$ m, $y = 0.45$ m, and $y = 0.6$ m for the fifth-order inlet velocity flow; CUF model ($N^U = 6$, $N^P = 5$, $p^U = 4$, $p^P = 3$)

for classical (i.e. standard) 1D reduced order models. Moreover, it should be remembered that the analysis accuracy is a free parameter of the CUF model, thus allowing for the automatic implementation of 1D refined models able to foresee complex phenomena with very low DOFs.

Chapter 10

Conclusions

10.1 Work outline

Advanced modelling techniques for structural, aeroelastic and fluid-dynamic analyses have been discussed in this thesis. The main novelty of the work lies in the use of refined, hierarchical, one-dimensional theories based on the Carrera Unified Formulation (CUF), which allows for the systematic approximations of 3D problems by arbitrary accuracy.

CUF has been widely presented in the framework of solid-mechanics: Starting from classical beam models, Chapter 2 has shown that higher-order phenomena (e.g. actual shear strain distribution, torsion, etc.) can be taken into account by opportunely enriching the displacement field. Variable kinematic beam models have been therefore developed with CUF by expressing the 3D displacement field as a N -order truncated expansion series of the generalized unknowns (i.e. displacements and displacement derivatives). The resulting beam models have been referred to as TE (Taylor Expansion) because Taylor-like polynomials are used. On the other hand, beam models with only pure displacement variables have been formulated in the same chapter and they have been referred to as LE (Lagrange Expansion). LE refined models are developed in the framework of CUF by interpolating the cross-sectional unknowns with linear, bi-linear, or quadratic Lagrange polynomials or a combination of them.

Particular attention has been focussed on free vibration analysis, which has played an important role in the whole research activities described in this thesis, including aeroelastic flutter instability analysis and dynamic gust response. Thus, strong form solutions for accurate modal analysis have been presented in Chapter 3. First, the equilibrium equations and the related natural boundary conditions of the generic N -order beam model have been derived; according to CUF, in fact, the governing equations do not depend on the problem characteristics and the theory order. Subsequently, both exact and approximate solutions have been devised. Exact solutions of any beam model with arbitrary boundary conditions have been found by formulating a frequency-dependant Dynamic Stiffness (DS) matrix and by using the Wittrick-Williams algorithm to carry out the resulting transcendental eigenvalue problem. Conversely, a linear eigenvalue problem has been derived by approximating the strong form governing equations by Radial Basis Functions (RBFs).

Chapter 4 has been dedicated to weak form solutions and the finite element approximation of the proposed CUF models. The Finite Element Method (FEM) still deserves important attentions due to its versatility and numerical efficiency. The various problems of the mechanics have been addressed, including static, free vibration and dynamic response problems. The strength of CUF is particularly clear when dealing with FEM because it allows one to express the elemental stiffness and mass matrices in terms of 3×3

fundamental nuclei, which are automatically expanded and assembled once the theory order and class are established.

Based on CUF, advanced methodologies for the analysis of aircraft structures have been reviewed in Chapter 5. In particular, multi-component structures have been introduced first. Next, the Component-Wise (CW) approach has been discussed. The CW method exploits the natural capability of the CUF beam models based on LE to be assembled at the cross-section level. This characteristic allows the analyst to use only CUF beam elements (i.e. the same stiffness matrix) to model each component of the structure; hence, purely physical surfaces are employed to construct the mathematical models. From the CAD/CAE scenario standpoint, this means that fictitious curves (e.g. stringers reference axes), surfaces (e.g. skins mid-planes) and links (e.g. multi-point constraints) are no more needed. Based on this idea, CW approach has also been extended to TE models and referred to as Multi-Line (ML). In the ML framework, each component of the structure is modelled via TE beam elements of arbitrary order. Compatibility of displacements between two or more components is then enforced through the Lagrange multipliers method.

The second part of this thesis deals with aeroelasticity. In particular, in Chapter 6, the Vortex (VLM) and the Doublet Lattice Methods (DLM) have been employed and extended to CUF models to develop aeroelastic models. According to the previous works, the infinite plate spline approach has been chosen for the mesh-to-mesh transformation in order to better exploit the shell-like capabilities of the structural models adopted. VLM has been used to model the steady contribution in the aerodynamic model, whereas DLM has provided the unsteady contribution in the frequency domain. Finally, the g-method has been described as an effective means for the formulation of the flutter stability problem. Particular attention is given to the extension of this methodology to exact DSM solutions of CUF beams.

Simplified, discrete, dynamic gust response analysis is discussed in Chapter 7. In this work, vertical gusts and one-minus-cosine idealization have been addressed. Accordingly, gust loads in terms of time-dependent load factors have been formulated. Subsequently, the mode superposition method has been briefly introduced in order to solve the linear dynamic response problem in the time domain by using both weak and strong form solutions of CUF models.

In the last part of the present work, minor extensions of 1D CUF models for fluid-dynamics problems have been carried out and they are discussed in Chapter 8. CUF approximation of Stokes flows was introduced in a recent thesis work and it has been here extended to the hierarchical p-version of FEM, which makes use of Legendre-like polynomials to interpolate the generalized unknowns along the 1D computational domain. For the sake of completeness, Stokes flows have been briefly discussed in Chapter 8 along with the correspondent Galerkin approximation. Then, the 3D velocity and scalar pressure fields have been approximated by arbitrary CUF expansions, which, similarly to the solid mechanics counterpart, allow the formulation of arbitrarily accurate 1D models of the Stokes equations.

Finally, some selected and noteworthy numerical results have been discussed in Chapter 9. In this chapter, the structural, aeroelastic and fluid-dynamics models have been validated. The results by the proposed CUF-based methodologies have been, in fact, widely compared to analytical solutions and to those from the literature and commercial codes, including finite element and finite volumes tools. Some conclusions and important remarks extrapolated from the numerical investigations are briefly summarized in the following section.

10.2 Concluding remarks

The results from the structural analyses have highlighted the following key-features of the 1D CUF approach:

- The adoption of refined 1D models allows for overcoming the well-known limitations of classical theories. Namely, torsion, coupling, and local effects, such as severe in-plane distortions, as well as shell-like modes can be accurately detected for a wide variety of configurations, including thin-walled cross-sections. Conversely, classical beam models can be effective in describing the bending behaviour of slender and moderately slender structures.
- CW and ML models have demonstrated their capabilities in dealing with multi-component and composite structures. In particular, the enhanced features of the CW approach to accurately deal with both static and dynamic analyses of aircraft structures have been highlighted.
- Highly accurate analyses are possible by CUF with very low computational efforts. Similar analyses are possible only by using shell/plate and solid models, which usually require a number of degrees of freedom that is some two order of magnitude higher.

Some interesting comments have also emerged from the comparison of FEM, DSM and RBFs methods when applied to free vibration analysis via CUF models:

- DSM is an elegant, effective method that allows for obtaining exact solutions for any-order beam model, independently from the problem characteristics and the boundary conditions. Thanks to DSM, one can in principle evaluate all the modal characteristics of a structure by utilizing one single element. However, DSM results in a non-linear eigenvalue problem and an iterative procedure is required.
- RBFs is a collocation method that allows the solution of the strong form equations in a very easy way. It results in a linear eigenvalue problem in the case of modal analyses. However, the solution may depend on the shape parameter used to formulating the RBFs and some numerical instabilities may appear if no optimization procedures are employed.
- Convergence analyses are needed in the case of FEM in order to obtain sufficiently accurate solutions. However, nowadays FEM is numerically stable and sufficiently mature to allow its usage in various fields of the mechanics, including those discussed in this thesis.

In the second part of Chapter 9, flutter analyses of various plate-like wings have been carried out by CUF and DLM. Moreover, the effects of lamination schemes and sweep angles have been investigated by using both FEM and DSM. The results have supported the following conclusions:

- Classical beam models are not adequate for flutter analysis. Refined 1D models are mandatory instead.
- At least a third-order ($N = 3$) beam model is needed to correctly predict the flutter. In fact, this phenomenon is usually accompanied by bending torsional couplings.
- Both FEM and DSM are effective for the flutter detection when applied to CUF models.

Before addressing gust responses, the mode superposition method has been validated in Section 9.6 versus a Newmark direct integration scheme and an analytical solution. Then, gust response by both TE and CW models of wing structures have highlighted the following remarks:

- Classical beam models can be quite accurate in dynamic gust response analysis if no coupling phenomena occur, i.e. when the response is dominated by only pure bending modes.
- In the case of composite wing structures, or in the presence of sweep angles, or when localized inertiae play a role in the torsion of the wing, refined models are mandatory.
- Static gust analyses (i.e. inertial terms are neglected) are conservative only if sufficiently short or sufficiently long gusts are encountered. Dynamic response should be considered otherwise.

The last part of the present thesis work has dealt with 1D CUF models of Stokes flows in rigid pipes. The results discussed in Chapter 9 have finally underlined the following comments:

- The proposed CUF models can reproduce the results by 3D finite volume codes with very low computational costs in the case of incompressible, viscous, laminar flows.
- Both simple Poiseuille and complex non-axisymmetric fluids can be successfully analyzed with the proposed methodology.
- Particular attention has to be focussed on the choice of the polynomial orders for the FE approximation in the case of Fluid-Dynamics analyses. Finite elements of the same polynomial degree for both velocity and pressures may be, in fact, unstable.

10.3 Future work

Many different perspective developments of the present formulation appear to be interesting. Regarding the structural formulation, the most promising developments deal with the extension to more complex composite aircraft structures; the extension to non-linear analysis, including both large strains and displacements; and buckling analysis. Nevertheless, the extension to fluid-dynamic problems of CUF models appear extremely interesting and challenging. Possible work in this direction might be conveyed to the extension to more complex fluids (e.g., by introducing convective and unsteady phenomena) and to fluid-structure interactions, including the analysis of compliant vessels.

Bibliography

- [1] M. Abdo, R. L'Heureux, F. Pepin, and F. Kafyeke. Equivalent finite element wing structural models used for aerodynamics-structures interaction. In *CASI 16th Aerospace Structures and Materials Symposium*, Montreal, Quebec, April 2003.
- [2] E. Albano and W. P. Rodden. A doublet-lattice method for calculating lift distributions on oscillating surfaces in subsonic flows. *AIAA Journal*, 7(2):279–285, 1969.
- [3] R. J. Allemang and D. L. Brown. A correlation coefficient for modal vector analysis. In *Proceedings of the International Modal Analysis Conference*, pages 110–116, 1982.
- [4] J. M. Argyris and S. Kelsey. *Energy theorems and structural analysis*. Butterworths, 1960.
- [5] E. A. Armanios and A. M. Badir. Free vibration analysis of anisotropic thin-wall close-section beams. *AIAA J*, 33(10):1905–10, 1995.
- [6] J. R. Banerjee. Coupled bending-torsional dynamic stiffness matrix for beam elements. *International Journal of Numerical Methods in Engineering*, 28:1283–1298, 1989.
- [7] J. R. Banerjee. Dynamic stiffness formulation for structural elements: a general approach. *Computers and Structures*, 63(1):101–103, 1997.
- [8] J. R. Banerjee. Free vibration analysis of a twisted beam using the dynamic stiffness method. *International Journal of Solids and Structures*, 38(38–39):6703–6722, 2001.
- [9] J. R. Banerjee. Free vibration of sandwich beams using the dynamic stiffness method. *Computers and Structures*, 81(18–19):1915–1922, 2003.
- [10] J. R. Banerjee. Development of an exact dynamic stiffness matrix for free vibration analysis of a twisted timoshenko beam. *Journal of Sound and Vibration*, 270(1–2):379–401, 2004.
- [11] J. R. Banerjee, C. W. Cheung, R. Morishima, M. Perera, and J. Njuguna. Free vibration of a three-layered sandwich beam using the dynamic stiffness method and experiment. *International Journal of Solids and Structures*, 44(22–23):7543–7563, 2007.
- [12] K. J. Bathe. *Finite element procedure*. Prentice hall, 1996.
- [13] C. O. Bennett and J. E. Myers. *Momentum, Heat, and Mass Transfer*. McGraw-Hill, 1962.

- [14] V. L. Berdichevsky, E. Armanios, and A. Badir. Theory of anisotropic thin-walled closed-cross-section beams. *Composites Engineering*, 2(5–7):411–432, 1992.
- [15] F. Biscani, G. Giunta, S. Belouettar, E. Carrera, and H. Hu. Variable kinematic beam elements coupled via Arlequin method. *Composite Structures*, 93:697–708, 2011.
- [16] M. Blair. A compilation of the mathematics leading to the doublet lattice method. TR 92–3028, Air Force Wright Laboratory, 1992.
- [17] M. Boscolo and J. R. Banerjee. Dynamic stiffness formulation for composite Mindlin plates for exact modal analysis of structures. part I: Theory. *Computers & Structures*, 96-97(0):61–73, 2012. DOI: 10.1016/j.compstruc.2012.01.002.
- [18] M. Boscolo and J. R. Banerjee. Dynamic stiffness formulation for composite Mindlin plates for exact modal analysis of structures. part II: Results and applications. *Computers & Structures*, 96-97(0):74–83, 2012. DOI: 10.1016/j.compstruc.2012.01.003.
- [19] F. Brezzi. On the existence, uniqueness and approximation of saddle-point problems arising from lagrange multipliers. *Revue Française d’Automatique, Informatique, Recherche Opérationnelle. Analyse Numérique*, 8(2):129–151, 1974.
- [20] L. Broglio. *Introduzione di un metodo generale per il calcolo delle strutture a guscio*. Ist. poligr. dello Stato, Roma, 1952. Monografie scientifiche di aeronautica n. 1.
- [21] E. F. Bruhn. *Analysis and Design of Flight Vehicle Structures*. Tri-State Offset Company, 1973.
- [22] E. Carrera. Theories and finite elements for multilayered, anisotropic, composite plates and shells. *Archives of Computational Methods in Engineering*, 9(2):87–140, 2002.
- [23] E. Carrera. Theories and finite elements for multilayered plates and shells: a unified compact formulation with numerical assessment and benchmarking. *Archives of Computational Methods in Engineering*, 10(3):216–296, 2003.
- [24] E. Carrera. *Fondamenti sul Calcolo di Strutture a Guscio Rinforzato per Veicoli Aerospaziali*. Levrotto & Bella, 2011.
- [25] E. Carrera, F Biscani, S. Belouettar, and G. Giunta. Analysis of thin-walled beams via a one-dimensional unified formulation through a Navier-type solution. *International Journal of Applied Mechanics*, 3(3):407–434, 2013.
- [26] E. Carrera and S. Brischetto. Analysis of thickness locking in classical, refined and mixed multilayered plate theories. *Composite Structures*, 82(4):549–562, 2008.
- [27] E. Carrera, M. Cinefra, and E. Petrolo, M. abd Zappino. *Finite Element Analysis of Structures through Unified Formulation*. John Wiley & Sons, 2014.
- [28] E. Carrera, M. Filippi, P. K. R. Mahato, and A. Pagani. Advanced models for free vibration analysis of laminated beams with compact and thin-walled open/closed sections. *Journal of Composite Materials*, 2014. In Press.

-
- [29] E. Carrera, M. Filippi, and E. Zappino. Laminated beam analysis by polynomial, trigonometric, exponential and zig-zag theories. *European Journal of Mechanics A/Solids*, 41:58–69, 2013.
- [30] E. Carrera, M. Filippi, and F. Zappino. Free vibration analysis of laminated beam by polynomial, trigonometric, exponential and zig-zag theories. *Journal of Composite Materials*, 2013.
- [31] E. Carrera and G. Giunta. Refined beam theories based on a unified formulation. *International Journal of Applied Mechanics*, 2(1):117–143, 2010.
- [32] E. Carrera, G. Giunta, P. Nali, and M. Petrolo. Refined beam elements with arbitrary cross-section geometries. *Computers and Structures*, 88(5–6):283–293, 2010.
- [33] E. Carrera, G. Giunta, and M. Petrolo. *Beam Structures: Classical and Advanced Theories*. John Wiley & Sons, 2011.
- [34] E. Carrera, M. Maiarú, and M. Petrolo. Component-wise analysis of laminated anisotropic composites. *International Journal of Solids and Structures*, 49:1839–1851, 2012.
- [35] E. Carrera, M. Maiarú, M. Petrolo, and G. Giunta. A refined 1D element for the structural analysis of single and multiple fiber/matrix cells. *Composite Structures*, 96:455–468, 2013.
- [36] E. Carrera and A. Pagani. Analysis of reinforced and thin-walled structures by multi-line refined 1D/beam models. *International Journal of Mechanical Sciences*, 75:278–287, 2013.
- [37] E. Carrera and A. Pagani. Multi-line enhanced beam model for the analysis of laminated composite structures. *Composites: Part B*, 57:112–119, 2014.
- [38] E. Carrera, A. Pagani, and J. R. Banerjee. Linearized buckling analysis of isotropic and composite beam-columns by carrera unified formulation and dynamic stiffness method. *Mechanics of Advanced Materials and Structures*, 2014. In Press.
- [39] E. Carrera, A. Pagani, and M. Petrolo. Classical, refined and component-wise theories for static analysis of reinforced-shell wing structures. *AIAA Journal*, 51(5):1255–1268, 2013.
- [40] E. Carrera, A. Pagani, and M. Petrolo. Component-wise method applied to vibration of wing structures. *Journal of Applied Mechanics*, 80(4):041012, 2013.
- [41] E. Carrera, A. Pagani, and M. Petrolo. Free vibration analysis of civil engineering structures by component-wise models. *AIAA Journal*, 333:4597–4620, 2013.
- [42] E. Carrera, A. Pagani, and M. Petrolo. Use of Lagrange multipliers to combine 1D variable kinematic finite elements. *Computers and Structures*, 129:194–206, 2013.
- [43] E. Carrera, A. Pagani, and M. Petrolo. Refined 1D finite elements for the analysis of secondary, primary, and complete civil engineering structures. *Journal of Structural Engineering*, page 04014123, 2014.

- [44] E. Carrera, A. Pagani, M. Petrolo, and E. Zappino. A component-wise approach in structural analysis. In B. H. V. Topping, editor, *Computational Methods for Engineering Science*, chapter 4, pages 75–115. Saxe-Coburg Publications, 2012.
- [45] E. Carrera, A. Pagani, and E. Zangallo. Thin-walled beams subjected to load factors and non-structural masses. *International Journal of Mechanical Sciences*, 81:109–119, 2014.
- [46] E. Carrera, A. Pagani, and F. Zangallo. Comparison of various 1D, 2D and 3D FE models for the analysis of thin-walled box with transverse ribs subjected to load factors. *Finite Elements in Analysis and Design*, 95:1–1, 2015.
- [47] E. Carrera and M. Petrolo. Refined beam elements with only displacement variables and plate/shell capabilities. *Meccanica*, 47(3):537–556, 2012.
- [48] E. Carrera and M. Petrolo. Refined one-dimensional formulations for laminated structure analysis. *AIAA Journal*, 50(1):176–189, 2012.
- [49] E. Carrera, M. Petrolo, and P. Nali. Unified formulation applied to free vibrations finite element analysis of beams with arbitrary section. *Shock and Vibrations*, 18(3):485–502, 2011.
- [50] E. Carrera and A. Varello. Dynamic response of thin-walled structures by variable kinematic one-dimensional models. *Journal of Sound and Vibration*, 331(24):5268–5282, 2012.
- [51] A. Catapano, G. Giunta, S. Belouettar, and E. Carrera. Static analysis of laminated beams via a unified formulation. *Composite Structures*, 94:75–83, 2011.
- [52] R. Chandra and I. Chopra. Experimental-theoretical investigation of the vibration characteristics of rotating composite box beam. *J. Aircrafts*, 29(4):657–64, 1992.
- [53] K. Chandrashekhara and K. M. Bangera. Free vibration of composite beams using a refined shear flexible beam element. *Computers and Structures*, 43(4):719–727, 1992.
- [54] K. Chandrashekhara, K. Krishnamurthy, and S. Roy. Free vibration of composite beams including rotary inertia and shear deformation. *Composite Structures*, 14:269–279, 1990.
- [55] P. C. Chen. Damping perturbation method for flutter solution: The g-method. *AIAA Journal*, 38(9):1519–1524, September 2000.
- [56] W. Q. Chen, C. F. Lv, and Z. G. Bian. Free vibration analysis of generally laminated beams via state-space-based differential quadrature. *Composite Structures*, 63:417–425, 2004.
- [57] P. Cicala. Sul calcolo delle strutture a guscio. *L’Aerotecnica*, XXVI(3):138–148, 1946. Part 1 of 4.
- [58] R. Courant. *Differential and Integral Calculus*. Interscience Publishers, 1937.
- [59] S. De Miranda, A. Gutierrez, and R. Miletta. Equilibrium-based reconstruction of three-dimensional stresses in gbt. *Thin-Walled Structures*, 74:146–154, 2014.

-
- [60] L. Demasi and E. Livne. Dynamic aeroelasticity of structurally nonlinear configurations using linear modally reduced aerodynamic generalized forces. *AIAA Journal*, 47(1), 2009.
- [61] A. Deperrois. XFLR5. <http://www.xflr5.com/xflr5.htm>, 2003–2014.
- [62] S. B. Dong, C. Alpdongan, and E. Taciroglu. Much ado about shear correction factors in Timoshenko beam theory. *International Journal of Solids and Structures*, 47:1651–1665, 2010.
- [63] M. Drela. XFOIL: An analysis and design system for low reynolds number airfoils. In *Conference on Low Reynolds Number Airfoil Aerodynamics*, University of Notre Dame, June 1989.
- [64] H. Ebner and H. Koller. Zur berechnung des kraftverlaufes in versteiften zylinder-shalen. *Luftf. Forsch.*, 1937.
- [65] H. Ebner and H. Koller. Ueber den kraftverlauf in längs und querversteiften scheiben. *Luftf. Forsch.*, 1938.
- [66] R. El Fatmi. On the structural behavior and the Saint Venant solution in the exact beam theory: application to laminated composite beams. *Computers and Structures*, 80(16–17):1441–1456, 2002.
- [67] R. El Fatmi. A non-uniform warping theory for beams. *Comptes Rendus - Mecanique*, 335:467–474, 2007.
- [68] M. S. A. Elsayed, R. Sedaghati, and M. Abdo. Accurate stick model development for static analysis of complex aircraft wing-box structures. *AIAA Journal*, 47(9):2063–2075, 2009.
- [69] L. Euler. *De curvis elasticis*. Lausanne and Geneva: Bousquet, 1744.
- [70] L. Euler. Principia pro motu sanguinis per arterias determinando. *Opera posthuma mathematica et physica anno 1844 detecta*, 2:814–823, 1775.
- [71] N. Fantuzzi, F. Tornabene, E. Viola, and A. J. M. Ferreira. A strong formulation finite element method (sfem) based on rbf and gdq techniques for the static and dynamic analyses of laminated plates of arbitrary shape. *Meccanica*, 49(10):2503–2542, 2014.
- [72] G. E. Fasshauer. Newton iteration with multiquadrics for the solution of nonlinear pdes. *Comput. Math. Applic.*, 43:423–438, 2002.
- [73] F. A. Fazzolari, J. R. Banerjee, and M. Boscolo. Buckling of composite plate assemblies using higher order shear deformation theory - an exact method of solution. *Thin-Walled Structures*, 71:18–34, 2013.
- [74] F. A. Fazzolari, M. Boscolo, and J. R. Banerjee. An exact dynamic stiffness element using a higher order shear deformation theory for free vibration analysis of composite plate assemblies. *Composite Structures*, 96:262–278, 2013.
- [75] A. J. M. Ferreira. A formulation of the multiquadric radial basis function method for the analysis of laminated composite plates. *Composite Structures*, 59(3):385–392, 2003.

- [76] A. J. M. Ferreira. Thick composite beam analysis using a global meshless approximation based on radial basis functions. *Mechanics of Advanced Materials and Structures*, 10:271–284, 2003.
- [77] A. J. M. Ferreira and G. E. Fasshauer. Computation of natural frequencies of shear deformable beams and plates by a rbf-pseudospectral method. *Computer Methods in Applied Mechanics and Engineering*, 196:134–146, 2006.
- [78] A. J. M. Ferreira, G. E. Fasshauer, R. C. Batra, and J. D. Rodrigues. Static deformations and vibration analysis of composite and sandwich plates using a layerwise theory and rbf-ps discretizations with optimal shape parameter. *Composite Structures*, 86(4):328–343, 2008.
- [79] A. J. M. Ferreira, C. M. C. Roque, and P. A. L. S. Martins. Analysis of composite plates using higher-order shear deformation theory and a finite point formulation based on the multiquadric radial basis function method. *Composites Part B: Engineering*, 34(7):627–636, 2003.
- [80] L. Formaggia, J. F. Gerbeau, F. Nobile, and A. Quarteroni. On the coupling of 3D and 1D Navier-Stokes equations for flow problems in compliant vessels. *Computational Methods in Applied Mechanics and Engineering*, 191:561–582, 2001.
- [81] L. Formaggia, D. Lamponi, and A. Quarteroni. One-dimensional models for blood flow in arteries. *Journal of Engineering Mathematics*, 47(3-4):251–279, 2003.
- [82] OpenFOAM Foundation. OpenFOAM. <http://www.openfoam.com/>, 2011–2014.
- [83] B. Gangadhara Prusty. Linear static analysis of hat stiffened laminated shells using finite elements. *Finite elements in analysis and design*, 39:1125–1138, 2003.
- [84] G. Giunta, F. Biscani, S. Belouettar, A. J. M. Ferreira, and E. Carrera. Free vibration analysis of composite beams via refined theories. *Composites: Part B*, 44:540–552, 2013.
- [85] G. Giunta, N. Metla, S. Belouettar, A. J. M. Ferreira, and E. Carrera. A thermo-mechanical analysis of isotropic and composite beams via collocation with radial basis functions. *Journal of Thermal Stress*, 36:1169–1199, 2013. doi: 10.1080/01495739.2013.819259.
- [86] W. J. Goodey. A stressed skin problem. *Aircr. Engin*, 1938.
- [87] M. G. Gunay and T. Timarci. Free vibration of composite box-beams by ANSYS. In *International Scientific Conference (UNITECH)*, Gabrovo, Bulgaria, 16-17 November 2012.
- [88] R. L. Harder and R. N. Desmarais. Interpolation using surface splines. *Journal of Aircraft*, 9(2):189–192, 1972.
- [89] R. L. Hardy. Multiquadric equations of topography and other irregular surfaces. *Geophysical Research*, 176:1905–1915, 1971.
- [90] R. L. Hardy. Theory and applications of the multiquadric-biharmonic method: 20 years of discovery. *Computers Math. Applic.*, 19(8/9):163–208, 1990.

-
- [91] P. R. Heyliger and Reddy J. N. A higher order beam finite element for bending and vibration problems. *Journal of Sound and Vibration*, 126(2):309–326, 1988.
- [92] H. Hoblit. *Gust Loads on Aircraft: Concepts and Applications*. Education Series. AIAA, Washington, USA, 1988.
- [93] D. H. Hodges and G. A. Pierce. *Introduction to Structural Dynamics and Aeroelasticity*. Cambridge University Press, Cambridge, UK, 2002.
- [94] S. J. Hollowell and J. Dugundji. Aeroelastic flutter and divergence of stiffness coupled, graphite/epoxy cantilevered plates. *Journal of Aircraft*, 21(1):69–76, 1984.
- [95] J. R. Hutchinson. Shear coefficients for Timoshenko beam theory. *Journal of Applied Mechanics*, 68:87–92, 2001.
- [96] M. Kameyama and H. Fukunaga. Optimum design of composite plate wings for aeroelastic characteristics using lamination parameters. *Composite Structures*, 85(3–4):213–224, 2007.
- [97] T. Kaneko. On Timoshenko’s correction for shear in vibrating beams. *Journal of Physics D: Applied Physics*, 8:1927–1936, 1975.
- [98] E. J. Kansa. Multiquadrics- a scattered data approximation scheme with applications to computational fluid dynamics. i: Surface approximations and partial derivative estimates. *Computers and Mathematics with Applications*, 19(8/9):127–145, 1990.
- [99] E. J. Kansa. Multiquadrics- a scattered data approximation scheme with applications to computational fluid dynamics. ii: Solutions to parabolic, hyperbolic and elliptic partial differential equations. *Computers and Mathematics with Applications*, 19(8/9):147–161, 1990.
- [100] E. J. Kansa and Y. C. Hon. Circumventing the ill-conditioning problem with multiquadric radial basis functions. *Computers and Mathematics with Applications*, 39(7–8):123–137, 2000.
- [101] K. Kapania and S. Raciti. Recent advances in analysis of laminated beams and plates, part I: Shear effects and buckling. *AIAA Journal*, 27(7):923–935, 1989.
- [102] K. Kapania and S. Raciti. Recent advances in analysis of laminated beams and plates, part II: Vibrations and wave propagation. *AIAA Journal*, 27(7):935–946, 1989.
- [103] J. Katz and A. Plotkin. *Low-Speed Aerodynamics: From Wing Theory to Panel Methods*. McGraw-Hill, Inc., New York, 1991.
- [104] J. S. Kim and K. W. Wang. Vibration analysis of composite beams with end effects via the formal asymptotic method. *Journal of Vibration and Acoustics*, 132(4):041003, 2010.
- [105] M. Kolli and K. Chandrashekhara. Finite element analysis of stiffened laminated plates under transverse loading. *Composite Science and Technology*, 56:1355–1361, 1996.
- [106] K. N. Koo. Aeroelastic characteristics of double-swept isotropic and composite wings. *Journal of Aircraft*, 38(2):343–348, 2001.

- [107] Y. Koutsawa, G. Giunta, and S. Belouettar. Hierarchical FEM modelling of piezo-electric beam structures. *Composite Structures*, 95:705–718, 2013.
- [108] P. Ladéveze, P. Sanchez, and J. G. Simmonds. Beamlike (Saint-Venant) solutions for fully anisotropic elastic tubes of arbitrary closed cross-section. *International Journal of Solids and Structures*, 41(7):1925–1944, 2004.
- [109] P. Ladéveze and J. G. Simmonds. The exact one-dimensional theory for end-loaded fully anisotropic beams of narrow rectangular cross section. *Journal of Applied Mechanics*, 68(6):865–868, 2001.
- [110] M. T. Landahl. Kernel function for nonplanar oscillating surfaces in a subsonic flow. *AIAA Journal*, 5(5):1045–1046, 1967.
- [111] L. Librescu and O. Song. On the static aeroelastic tailoring of composite aircraft swept wings modelled as thin-walled beam structures. *Composites Engineering*, 2:497–512, 1992.
- [112] F. Miglioretti, E. Carrera, and M. Petrolo. Variable kinematic beam elements for electro-mechanical analysis. *Smart Structures and Systems*, 13(4):517–546, 2014.
- [113] MSC.Software Corporation. *MD Nastran 2010 Quick Reference Guide*, 2010.
- [114] T. K. Nguyen, T. P. Vo, and H. T. Thai. Static and free vibration of axially loaded functionally graded beams based on the first-order shear deformation theory. *Composites Part B: Engineering*, 55:147–157, 2013.
- [115] V. V. Novozhilov. *Theory of elasticity*. Pergamon, Elmsford, 1961.
- [116] F. Nunes, M. Correia, J. R. Correia, N. Silvestre, and A. Moreira. Experimental and numerical study on the structural behavior of eccentrically loaded gfrp columns. *Thin-Walled Structures*, 72:175–187, 2013.
- [117] E. Oñate. *Structural Analysis with the Finite Element Method: Linear Statics, Volume 1*. Springer, 2009.
- [118] A. Pagani, M. Boscolo, J. R. Banerjee, and E. Carrera. Exact dynamic stiffness elements based on one-dimensional higher-order theories for free vibration analysis of solid and thin-walled structures. *Journal of Sound and Vibration*, 332(23):6104–6127, 2013.
- [119] A. Pagani, M. Boscolo, J. R. Banerjee, and E. Carrera. Exact dynamic stiffness elements based on one-dimensional higher-order theories for free vibration analysis of solid and thin-walled structures. *Journal of Sound and Vibration*, 332(23):6104–6127, 2013.
- [120] A. Pagani, E. Carrera, J. R. Banerjee, P. H. Cabral, G. Caprio, and A. Prado. Free vibration analysis of composite plates by higher-order 1D dynamic stiffness elements and experiments. *Composite Structures*, 118:654–663, 2014.
- [121] A. Pagani, E. Carrera, M. Boscolo, and J. R. Banerjee. Refined dynamic stiffness elements applied to free vibration analysis of generally laminated composite beams with arbitrary boundary conditions. *Composite Structures*, 110(23):305–316, 2014.

-
- [122] A. Pagani, E. Carrera, and A. J. M. Ferreira. Higher-order theories and radial basis functions applied to free vibration analysis of thin-walled beams. *Mechanics of Advanced Materials and Structures*, 2014. In Press.
- [123] A. Pagani, M. Petrolo, and E. Carrera. Flutter analysis by refined 1D dynamic stiffness elements and doublet lattice method. *Advances in Aircraft and Spacecraft Science*, 1(3):291–310, 2014.
- [124] A. Pagani, E. Zangallo, and E. Carrera. Influence of non-structural localized inertia on free vibration response of thin-walled structures by variable kinematic beam formulations. *Composite Structures*, 2014:141982, 2014.
- [125] S. N. Patel, P. K. Datta, and A. H. Seikh. Buckling and dynamic instability analysis of stiffened shell panels. *Thin-Walled Structures*, 44:321–333, 2006.
- [126] M. Petrolo. *Advanced aeroelastic models for the analysis of lifting surfaces made of composite materials*. PhD thesis, Politecnico di Torino, Turin, Italy, 2011.
- [127] M. Petrolo. Flutter analysis of composite lifting surfaces by the 1D Carrera Unified Formulation and doublet lattice method. *Composite Structures*, 95:539–546, 2013.
- [128] M. Petrolo. Advanced 1D structural models for flutter analysis of lifting surfaces. *International Journal of Aeronautical and Space Sciences*, 13(2):199–209, 2014.
- [129] P. Piperni, M. Abdo, and F. Kafyeke. The building blocks of multi-disciplinary wing design method. In *CASI 50th Annual General Meeting*, Montreal, Quebec, 2003.
- [130] W. H. Press, S. A. Teukolsky, W. T. Vetterling, and B. P. Flannery. *Numerical Recipes: The Art of Scientific Computing*. Cambridge University Press, New York, 3rd edition, 2007.
- [131] A. Quarteroni. *Numerical Models for Differential Problems*. Springer, Milano, 1th edition, 2009.
- [132] A. Rajagopal and D. H. Hodges. Asymptotic approach to oblique cross-sectional analysis of beams. *Journal of Applied Mechanics*, 81(3):031015, 2014.
- [133] J. N. Reddy. *Mechanics of laminated composite plates and shells. Theory and Analysis*. CRC Press, 2nd edition, 2004.
- [134] R. M. Rivello. *Theory and analysis of flight structures*. McGraw-Hill, 1969.
- [135] W. P. Rodden, J. P. Giesing, and T. P. Kálmán. Refinement of the nonplanar aspects of the subsonic doublet-lattice lifting surface method. *Journal of Aircraft*, 9(1):69–73, 1972.
- [136] W. P. Rodden, P. F. Taylor, and S. C. Jr McIntosh. Further refinement of the subsonic doublet-lattice method. *Journal of Aircraft*, 35(5):720–726, 1998.
- [137] C. M. C. Roque and A. J. M. Ferreira. Numerical experiments on optimal shape parameters for radial basis functions. *Numerical Methods for Partial Differential Equations*, 26(3):675–689, 2010.
- [138] S. K. Satsangi and M. Mukhopadhyay. Finite element state analysis of girder bridges having arbitrary platform. *Int. Ass. of Bridge Struct. Engng.*, 17:65–94, 1987.

- [139] R. Schaback. On the efficiency of interpolation by radial basis functions. In A. Le Méhauté, C. Rabut, and L. L. Schumaker, editors, *Proceedings of Surface fitting and multiresolution methods*, pages 309–318. Vanderbilt University Press, 1997.
- [140] R. Schardt. *Verallgemeinerte Technische Biegetheorie*. Springer, Berlin, 1989.
- [141] R. Schardt. Generalized beam theory - an adequate method for coupled stability problems. *Thin-Walled Structures*, 19:161–180, 1994.
- [142] D. M. Schuster, D. D. Liu, and L. J. Huttzell. Computational aeroelasticity: success, progress, challenge. *Journal of Aircraft*, 40(5):843–856, 2003.
- [143] S. J. Sherwin, V. Franke, and J. Peiro'. One-dimensional modelling of a vascular network in space-time variables. *Journal of Engineering Mathematics*, 47(3-4):217–250, 2003.
- [144] N. Silvestre. Generalised beam theory to analyse the buckling behaviour of circular cylindrical shells and tubes. *Thin-Walled Structures*, 45(2):185–198, 2007.
- [145] N. Silvestre and D. Camotim. Shear deformable generalized beam theory for the analysis of thin-walled composite members. *Journal of Engineering Mechanics*, 139(8):1010–1024, 2013.
- [146] N. P. Smith, A. J. Pullan, and P. J. Hunter. An anatomically based model of transient coronary blood flow in the heart. *SIAM Journal of Applied Mathematics*, 62(3):990–1018, 2002.
- [147] I. S. Sokolnikoff. *Mathematical theory of elasticity*. McGraw-Hill, 1956.
- [148] N. G. Stephen. Timoshenko's shear coefficient from a beam subjected to gravity loading. *Journal of Applied Mechanics*, 47:121–127, 1980.
- [149] G. Strang. *Calculus*. Welles-Cambridge Press, 1991.
- [150] W. Su and C. E. S Cesnik. Dynamic response of highly flexible flying wings. *AIAA Journal*, 49(2):324–339, 2011.
- [151] S. P. Sutera and R. Skalak. The history of poiseuille's law. *Annual Review of Fluid Mechanics*, 25:1–19, 1993.
- [152] B. Szabó and I. Babůska. *Finite Element Analysis*. Wiley Interscience, 1991.
- [153] T. Theodorsen. General theory of aerodynamic instability and the mechanism of flutter. Technical Report 496, NACA, 1934.
- [154] T. I. Thinh and N. N. Khoa. Free vibration analysis of stiffened laminated plates using a new stiffened element. *Technische Mechanik*, 28(3–4):227–236, 2008.
- [155] S. P. Timoshenko. On the corrections for shear of the differential equation for transverse vibrations of prismatic bars. *Philosophical Magazine*, 41:744–746, 1922.
- [156] S. P. Timoshenko. On the transverse vibrations of bars of uniform cross section. *Philosophical Magazine*, 43:125–131, 1922.
- [157] S. P. Timoshenko and J. N. Goodier. *Theory of elasticity*. McGraw-Hill, 1970.

-
- [158] F. Tornabene, N. Fantuzzi, E. Viola, and A. J. M. Ferreira. Radial basis function method applied to doubly-curved laminated composite shells and panels with a general higher-order equivalent single layer formulation. *Composites Part B: Engineering*, 55(0):642–659, 2013.
- [159] S. W. Tsai. *Composites Design*. Dayton, Think Composites, 4th edition, 1988.
- [160] A. Varello. *Advanced higher-order one-dimensional models for fluid-structure interaction analysis*. PhD thesis, Politecnico di Torino, Turin, Italy, 2013.
- [161] A. Varello and E. Carrera. Nonhomogeneous atherosclerotic plaque analysis via enhanced 1D structural models. *Smart Structures and Systems*, 13(4):659–683, 2014.
- [162] A. Varello, E. Carrera, and L. Demasi. Vortex lattice method coupled with advanced one-dimensional structural models. *Journal of Aeroelasticity and Structural Dynamics*, 2(2):53–78, 2011.
- [163] A. Varello, E. Carrera, and L. Demasi. Vortex lattice method coupled with advanced one-dimensional structural models. *Journal of Aeroelasticity and Structural Dynamics*, 2(2):53–78, 2011.
- [164] V. Z. Vlasov. *Thin-walled elastic beams*. National Science Foundation, Washington, 1961.
- [165] E. Volterra and E. C. Zachmanoglou. *Dynamics of Vibrations*. Charles E. Merrill Books Inc., Ohio, USA, 1965.
- [166] G. M. Vörös. A special purpose element for shell-beam systems. *Computers and Structures*, 29(2):301–308, 1988.
- [167] G. M. Vörös. Finite element analysis of stiffened plates. *Periodica Polytechnica*, 51(2):105–112, 2007.
- [168] Q. Wang and W. Yu. A variational asymptotic approach for thermoelastic analysis of composite beams. *Advances in Aircraft and Spacecraft Science*, 1(1):93–123, 2014.
- [169] K. Washizu. *Variational Methods in Elasticity and Plasticity*. Pergamon, Oxford, 1968.
- [170] H. Wendland. Error estimates for interpolation by compactly supported radial basis functions of minimal degree. *Journal of Approximation Theory*, 93:258–296, 1998.
- [171] F. W. Williams and W. H. Wittrick. An automatic computational procedure for calculating natural frequencies of skeletal structures. *International Journal of Mechanical Sciences*, 12(9):781–791, 1970.
- [172] W. H. Wittrick. A unified approach to initial buckling of stiffened panels in compression. *International Journal of Numerical Methods in Engineering*, 11:1067–1081, 1968.
- [173] W. H. Wittrick and F. W. Williams. A general algorithm for computing natural frequencies of elastic structures. *Quarterly Journal of mechanics and applied sciences*, 24(3):263–284, 1970.

- [174] W. H. Wittrick and F. W. Williams. Buckling and vibration of anisotropic or isotropic plate assemblies under combined loadings. *International Journal of Mechanical Sciences*, 16(4):209–239, 1974.
- [175] S. Xiang, Z.-Y Bi, S.-X. Jiang, Y.-X. Jin, and M.-S. Yang. Thin plate spline radial basis function for the free vibration analysis of laminated composite shells. *Composite Structures*, 93(2):611–615, 2011.
- [176] W. Yu and D. H. Hodges. Elasticity solutions versus asymptotic sectional analysis of homogeneous, isotropic, prismatic beams. *Journal of Applied Mechanics*, 71:15–23, 2004.
- [177] W. Yu and D. H. Hodges. Generalized Timoshenko theory of the variational asymptotic beam sectional analysis. *Journal of the American Helicopter Society*, 50(1):46–55, 2005.
- [178] R. Yurkovich. Status of unsteady aerodynamic prediction for flutter of high-performance aircraft. *Journal of Aircraft*, 40(5):832–842, 2003.
- [179] O. C. Zienkiewicz and R. L. Taylor. *The Finite Element Method for Solid and Structural Mechanics*. Butterworth-Heinemann, Washington, 6th edition, 2005.

COMMISSIONE GIUDICATRICE
"FLUIDODINAMICA"

Il dott. Alfonso PAGANI ha discusso in data 9 marzo 2015 presso il Dipartimento di Ingegneria Meccanica e Aerospaziale (DIMEAS) del Politecnico di Torino la tesi di Dottorato avente il seguente titolo:

"Component-wise Models for Static, Dynamic and Aeroelastic Analysis of Metallic and Composite Aerospace Structures"

Le ricerche oggetto della tesi sono rilevanti e attuali.

Le metodologie appaiono originali ed efficaci.

I risultati sono interessanti ed analizzati con ottimo senso critico.

Nel colloquio il candidato dimostra ottima conoscenza delle problematiche trattate.

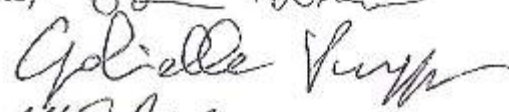
La Commissione unanime giudica ottimo il lavoro svolto e propone che al dott. Alfonso PAGANI venga conferito il titolo di **Dottore di Ricerca**.

Data, 9 marzo 2015

Prof. Domenic D'AMBROSIO (Presidente)



Prof. Gabriella PUPPO (Componente)



Prof. Alberto MILAZZO (Segretario)

